

Universidade de São Paulo  
Instituto de Física

# Modelamento do campo magnético de descargas não-axissimétricas em tokamaks

David Ciro Taborda

Orientador: Prof. Dr. Iberê Luiz Caldas

Tese de doutorado apresentada ao Instituto de  
Física para a obtenção do título de Doutor em  
Ciências.

Banca Examinadora:

Prof. Dr. Iberê Luiz Caldas (Universidade de São Paulo)

Prof. Dr. Artour Elfimov (Universidade de São Paulo)

Prof<sup>a</sup>. Dr<sup>a</sup>. Maria Célia Ramos de Andrade (Instituto Nacional de Pesquisas Espaciais)

Prof<sup>a</sup>. Dr<sup>a</sup>. Marisa Roberto (Instituto Tecnológico de Aeronáutica)

Prof. Dr. Ricardo Luiz Viana (Universidade Federal do Paraná)

São Paulo

2016

**FICHA CATALOGRÁFICA**  
**Preparada pelo Serviço de Biblioteca e Informação**  
**do Instituto de Física da Universidade de São Paulo**

Taborda, David Ciro

Modelamento do campo magnético de descargas não-axissimétricas em tokamaks. São Paulo, 2016.

Tese (Doutorado) – Universidade de São Paulo. Instituto de Física. Depto. de Física Aplicada.

Orientador: Prof. Dr. Iberê Luiz Caldas

Área de Concentração: Quebra da Simetria Axial em Tokamaks.

Unitermos: 1. Magnetohidrodinâmica; 2. Teoria não linear; 3. Física computacional; 4. Tokamaks.

USP/IF/SBI-103/2016

University of São Paulo  
Institute of Physics

# Magnetic field modeling for non-axisymmetric tokamak discharges

David Ciro Tabora

Advisor: Prof. Dr. Iberê Luiz Caldas

Submitted to the Institute of Physics in partial  
fulfillment of the requirements for the degree of  
Doctor in Sciences.

Examination Board:

Prof. Dr. Iberê Luiz Caldas (Universidade de São Paulo)

Prof. Dr. Artour Elfimov (Universidade de São Paulo)

Prof<sup>a</sup>. Dr<sup>a</sup>. Maria Célia Ramos de Andrade (Instituto Nacional de Pesquisas Espaciais)

Prof<sup>a</sup>. Dr<sup>a</sup>. Marisa Roberto (Instituto Tecnológico de Aeronáutica)

Prof. Dr. Ricardo Luiz Viana (Universidade Federal do Paraná)

São Paulo

2016



# Acknowledgments

This research has been possible due to the opportune interaction with great colleagues, friends and professors. Thanks to Prof. Iberê Luiz Caldas for his advice, guidance and support, to Dr. Todd Edwin Evans for his advice during the internship and his stimulating discussions along the development of this research and to the General Atomics staff for the welcome during that period. I am also grateful to Dr. Gustavo Canal for all the instructive discussions on plasma physics during the internship, to Dr. Vinicius Duarte for presenting me the concept of magnetic helicity and to Dr. Zwinglio Guimarães Filho for his advice on numerical optimization methods. Special thanks to the colleagues in our research group: Dennis Toufen, Julio da Fonseca, Alberto Marcus, Meirielen Caetano de Sousa, Everton Medeiros, Rafael de Oliveira, Celso Vieira Abud and Paula Allegro Pestana.

This work was developed in the Physics Institute of the São Paulo University, with auspice from the São Paulo Research Foundation (FAPESP) under grants 2012/18073-1 and 2014/03899-7. I am also indebted with the Brazilian people for the warm reception during all my post-graduation years.



# Resumo

Neste trabalho estuda-se a modelagem do campo magnético em configurações realistas de plasmas em equilíbrio não-axissimétrico e o fluxo de calor nos componentes em contato com o plasma em descargas de tokamaks com desviadores poloidais. Começa-se estabelecendo a relação entre configurações magnéticas arbitrárias e sistemas dinâmicos Hamiltonianos. Então aplicamos o conceito de helicidade magnética, que é usado para estabelecer limitações topológicas sobre as linhas de campo magnético em plasmas ideais, assim como para compreender a auto-consistência das superfícies magnéticas reconectadas em configurações não-axissimétricas. Após esta discussão teórica, apresentam-se alguns resultados sobre o equilíbrio magnetohidrodinâmico e o uso de soluções analíticas à equação de Grad-Shafranov para descrever descargas reais em tokamaks, com base em diagnósticos experimentais e condições de contorno realistas. Também realiza-se uma comparação entre a reconstrução do equilíbrio de uma descarga do DIII-D, obtida mediante uma rotina numérica desenvolvida para esta pesquisa, com a obtida mediante o código EFIT, usado amplamente em diversos tokamaks. Após isso, apresenta-se uma descrição simplificada do campo magnético não-axissimétrico, criado por fontes determinadas, e a sua implementação para descrever o campo magnético devido às correntes externas em tokamaks. Então, usam-se estas rotinas para desenvolver um procedimento numérico que ajusta um conjunto adequado de parâmetros não-lineares de correntes filamentosas internas, com as quais pretende-se modelar a resposta do plasma com base nas medidas de campo magnético fora do plasma. Finalmente, estes métodos são utilizados para modelar o campo magnético criado por uma instabilidade com rotação lenta numa descarga do DIII-D. Com base nas medidas das sondas magnéticas é possível modelar os campos criados em regiões arbitrárias próximas da borda do plasma. Usando esta informação é possível determinar a borda não-axissimétrica do plasma mediante as invariantes magnéticas calculadas com a utilização de uma rotina desenvolvida durante este trabalho. A intersecção da superfície invariante com a câmara do tokamak coincide satisfatoriamente com as medidas de fluxo de calor nas placas do divertor para a mesma descarga, indicando o desenvolvimento de uma variedade giratória criada pelas correntes de plasma não-axissimétricas, e sustentando quantitativamente a nossa descrição simpli-

ficada do campo magnético, assim como a definição da borda do plasma mediante as invariantes magnéticas.

**Palavras-chave:** Tokamaks, equilíbrio MHD, plasmas não-axissimétricos, resposta do plasma, interação plasma-parede, modos rasgantes, ilhas magnéticas, dinâmica Hamiltoniana.

# Abstract

In this work we study the magnetic field modeling of realistic non-axisymmetric plasma equilibrium configurations and the heat flux patterns on the plasma facing components of tokamak divertor discharges. We start by establishing the relation between generic magnetic configurations and Hamiltonian dynamical systems. We apply the concept of magnetic helicity, used to establish topological bounds for the magnetic field lines in ideal plasmas, and to understand the self-consistency of reconnected magnetic surfaces in non-axisymmetric configurations. After this theoretical discussion, we present some results on magnetohydrodynamic equilibrium and the use of analytical solutions to the Grad-Shafranov equation for describing real tokamak discharges based on the experimental diagnostics and realistic boundary conditions. We also compare the equilibrium reconstruction of a DIII-D discharge obtained with a numerical reconstruction routine, developed as part of this research, and the EFIT code used by several tokamak laboratories around the world. The magnetic topology and plasma profiles obtained with our method are in considerable agreement with the numerical reconstruction performed with the other code. Then, we introduce a simplified description of the generic non-axisymmetric magnetic field created by known sources and implement it numerically for describing the magnetic field due to external coils in tokamak devices. After that, we use this routines to develop a numerical procedure to adjust a suitable set of non-linear parameters of internal filamentary currents, which are intended to model the plasma response based on the magnetic field measurements outside the plasma. Finally, these methods are used to model the magnetic field created by a slowly rotating plasma instability in a real DIII-D discharge. The plasma response modeling is based on the magnetic probe measurements and allow us to calculate the magnetic field in arbitrary locations near the plasma edge. Using this information we determine the non-axisymmetric plasma edge through the magnetic invariant manifolds routine developed during this research. The intersection of the calculated invariant manifold with the tokamak chamber agrees considerably well with the heat flux measurements for the same discharge at the divertor plates, indicating the development of a rotating manifold due to the internal asymmetric plasma currents, giving quantitative support to our simplified description of the magnetic

field and the plasma edge definition through the invariant manifolds.

**Keywords:** Tokamaks, MHD equilibrium, non-axisymmetric plasmas, plasma response, plasma-wall interaction, tearing modes, magnetic islands, Hamiltonian dynamics.

# Contents

<b>1</b>	<b>Introduction</b>	<b>11</b>
<b>2</b>	<b>Magnetic fields and Hamiltonian Systems</b>	<b>15</b>
2.1	The Hamilton equations . . . . .	15
2.2	Magnetic field lines from a variational principle . . . . .	16
2.3	Magnetic field lines as a Hamiltonian system . . . . .	17
2.4	The tokamak magnetic field . . . . .	19
2.4.1	Resonances and magnetic islands . . . . .	22
2.5	Plasma response . . . . .	25
2.5.1	Magnetic helicity and topology . . . . .	25
2.5.2	Evolution of the magnetic helicity . . . . .	28
2.5.3	Magnetic islands in plasmas . . . . .	29
<b>3</b>	<b>Axisymmetric MHD equilibrium</b>	<b>33</b>
3.1	Boundary conditions . . . . .	36
3.2	General numerical solution . . . . .	38
3.3	Analytical equilibrium solutions . . . . .	40
3.3.1	Arbitrary functions . . . . .	41
3.3.2	Geometrical parameters of the equilibrium . . . . .	45
3.3.3	Control functions . . . . .	46
3.4	Semi-analytical solution . . . . .	47
3.4.1	Numerical implementation . . . . .	48
3.4.2	Safety factor profile . . . . .	50
3.5	Comparison with EFIT . . . . .	51
3.6	Chapter conclusions . . . . .	56
<b>4</b>	<b>Non-axisymmetric discharges</b>	<b>57</b>
4.1	Magnetic field from known sources . . . . .	58
4.2	Modeling the plasma response . . . . .	59
4.3	Magnetic invariant manifolds . . . . .	65

4.4	Chapter conclusions . . . . .	70
<b>5</b>	<b>Modeling time-dependent heat patterns in DIII-D tokamak</b>	<b>73</b>
5.1	Experimental observations . . . . .	73
5.2	Magnetic perturbation modeling . . . . .	75
5.2.1	Magnetic separatrix and footprints . . . . .	81
5.3	Chapter conclusions . . . . .	85
<b>6</b>	<b>Conclusions and perspectives</b>	<b>87</b>
	<b>Appendices</b>	<b>89</b>
<b>A</b>	<b>Useful derivations</b>	<b>91</b>
A.1	The Euler-Lagrange Equations . . . . .	91
A.2	Evolution of a surface function . . . . .	92
A.3	Evolution of the magnetic helicity . . . . .	93
A.4	Magnetic field frozen into the plasma . . . . .	95
A.5	Magnetic field from a finite segment . . . . .	96
<b>B</b>	<b>Numerical methods</b>	<b>99</b>
B.1	Levenberg-Marquardt optimization . . . . .	99
B.2	Numerical integration routine . . . . .	100
B.3	Invariant manifolds calculation . . . . .	102

# Chapter 1

## Introduction

Thermonuclear fusion is today one of the main research subjects in the *clean* generation of electricity. It is based upon the *deuterium - tritium* (D-T) reaction producing a 3.5 MeV  $^4\text{He}$  nucleus and a 14.1 MeV neutron, or the less energetic *deuterium-deuterium* (D-D) reaction resulting on a 0.8 MeV  $^3\text{He}$  nucleus and a 2.45 MeV neutron. Thermonuclear fusion stands out among other concepts due to the large energy/volume ratio of its fuels and to the natural abundance of the deuterium isotope (D or  $^2\text{H}$ ), which can be found naturally on sea-water and corresponds to *one* on every 6700 atoms of Hydrogen [Freidberg (2007)]. On the other hand, tritium (T or  $^3\text{H}$ ), is quite scarce in nature, but the neutron released by the D-T reaction can be used to produce more tritium, *in situ*, by means of its reaction with lithium (Li), also abundant in nature [Freidberg (2007); Mazayuki (2012)].

One of the main difficulties of thermonuclear fusion is that it involves temperatures of order  $10^8$  K in a laboratory setup, which requires the fuels to be completely ionized, i.e. in a *plasma* state, in which charged particles interact with each other through long-range electromagnetic fields. The inherent complexity of Plasma Physics has been a determinant factor in the apparent delay for reaching commercial viability of fusion reactors, which started their history in the 1950's with the tokamak concept [Wesson (2004)].

Magnetohydrodynamics (MHD), manages to capture the collective aspects of the plasma dynamics by centering in the description of a set of fields that condense the most relevant information of the system without caring for the individual behavior of the charged particles. This description offers a systematic treatment of the particles-fields dynamics with fewer parameters to be determined experimentally [Bittencourt (2004)], and has been successful in describing plasma oscillations, MHD equilibrium and stability, magnetic reconnection and other non-linear phenomena [Biskamp (1993)]. However, the treatment of MHD equations in realistic configurations requires developing specialized numerical tools and considerable computational power, and the development of simplified models that intend to capture the self-consistent plasma dynamics becomes desirable and

interesting.

The magnetic field plays a dominant role in the confinement of the charged particles in a tokamak device. Consequently, the magnetic field lines provide relevant information on the first order particle dynamics and the locations in the plasma where instabilities develop. Also, the intersection of these lines with the tokamak chamber gives us information about the preferred locations for heat deposition by parallel transport. In axisymmetric situations the structure of the plasma magnetic field is quite simple and can be described after determining one single scalar field and one flux function. This, however, changes dramatically when the problem becomes non-axisymmetric. In this situation the problem can not be posed in a unique form and must be studied perturbatively, but self consistency issues pose additional difficulties.

In the perturbative case, simplified descriptions of the plasma equilibrium can be obtained for certain geometrical conditions, and used to derive Poincaré maps of the magnetic field lines inside the plasma. These maps are available for circular section large aspect-ratio tokamaks [Caldas et al. (1996); Balescu et al. (1998)], and include realistic effects like the Shafranov shift [da Silva et al. (2006)] due to toroidicity. With these maps we can study general features of the magnetic bifurcations creating the magnetic islands and chaotic bands which have been related to experimental observations in diverted plasmas [de Vries et al. (1997)], and are also usable for the innermost magnetic topology of shaped plasmas, where the geometrical approximations hold.

In larger devices with small aspect-ratio and large elongation the plasma is no longer circular and frequently presents a magnetic separatrix at the plasma edge. This causes some magnetic field lines to be open and intersect the tokamak chamber [Stangeby (2000)]. Symplectic maps for the separatrix region have been also developed for these situations [Kroetz et al. (2010); Abdullaev (2014)] and can be used to study the separatrix splitting and magnetic footprints along the tokamak chamber when a non-axisymmetric magnetic perturbation disturbs the field lines. Also, they provide insight about the relevant parameters governing the footprint structure respect to externally produced magnetic perturbations.

For more general situations, with small aspect-ratio and plasma shaping, it is difficult to develop a sufficiently flexible symplectic map, and we are forced to take a step further in complexity if we want to consider the plasma response to the applied or inherent magnetic asymmetries. In the perturbative limit this requires solving the axisymmetric equilibrium problem and subsequently applying the non-axisymmetric perturbations. This approach has been used to model the effects of resonant magnetic perturbation (RPM) coils in realistic divertor geometries [Kroetz et al. (2008)] and real tokamaks discharges [Evans et al. (2002)]. Also, the plasma response to these fields has been modeled based in ideal

MHD requirements, using the magnetic topology created by the asymmetric vacuum field when combined with the axisymmetric field [Buttery et al. (1996); Cahyna et al. (2011)].

One of the main interests in modeling the magnetic footprint structure realistically is understanding the interaction of the internal non-axisymmetric currents with the magnetic separatrix in single-null discharges. This is fundamental to understand the influence of the plasma instabilities on the heat deposition in the divertor tiles. For a tokamak like ITER, the development of a rotating non-axisymmetric heat flux can cause periodic variation in the thermal loading of the target plates and cooling lines, resulting in thermal and mechanical fatigue of these components leading to premature failures. This type of slowly rotating non-axisymmetric internal mode must be controlled to prevent damage to the divertor, and the periodic variations of the thermal loads may be modified to reduce damage.

Experiments using in-chamber 3D coils, such as those being installed in ITER, have been carried out in DIII-D to entrain these modes and prevent them from resulting in disruptions [Volpe et al. (2009)], but additional research is needed to better understand how to mitigate the thermal cycling of the divertors and this requires modeling the time-dependent evolution of the heat patterns caused by the plasma instabilities.

In this work we are interested in understanding the effects of the non-axisymmetric plasma response over the magnetic topology of the plasma edge in a realistic situation. From an MHD perspective this requires describing the ideal plasma response in the non-reconnecting magnetic surfaces and the magnetic reconnection process leading to the magnetic islands [Biskamp (1993)], which is complex and involves several characteristic times. As we are interested in simple models which encompasses relevant dynamics we will take a semi-analytical approach. For the axisymmetric part of the magnetic field we will develop a numerical routine based on analytical solutions of the Grad-Shafranov equation [McCarthy (1999); Ciro and Caldas (2014)]. This allows us to approximate efficiently a realistic MHD equilibrium configuration. For the non-axisymmetric part, we introduce a generic description of the external asymmetric fields and the plasma response based on filamentary currents outside and inside the plasma volume, and adjust the model parameters using real measurements in tokamak discharges. This procedure allows us to model the magnetic field from the plasma response with filamentary currents, regardless of any explicit knowledge of the process taking place inside the plasma, while at the same time we approximate the time-dependent measurements at the magnetic probes.

Using the complete magnetic field we can determine the non-axisymmetric separatrix of a single null tokamak discharge, which corresponds to the invariant surfaces of the magnetic flow converging to the non-axisymmetric magnetic saddle of the discharge. An efficient numerical method [Ciro et al. (2016a)] is used to build such surfaces and

calculate their intersection with the plasma facing components. In [Ciro et al. (2016b)] this approach for modeling the magnetic field was used to estimate the heat deposition region based on the non-axisymmetric magnetic separatrix, obtaining a reasonable time-dependent match with the infrared diagnostics of DIII-D.

In the following chapters we present a systematic method to calculate the complete magnetic field of a tokamak discharge. First we present a semi-analytical approach to model the axisymmetric equilibrium field, then, a simple method to calculate the magnetic field due to non-axisymmetric external currents, and finally, a numerical method to adjust the parameters of the internal filamentary currents based in experimental diagnostics. Also, we present the tools developed during this doctoral research to achieve that goal and to calculate the magnetic invariant manifolds that determine the plasma edge. We start in Chapter 2 with a discussion about the symplectic nature of the magnetic field lines and its consequences in magnetic confinement devices, then we mention the self-consistency problem in a non-axisymmetric situation and attempt to reconcile the seemingly diverging views from MHD and the Kolmogorov-Arnold-Moser (KAM) theory about the resilience of rational magnetic surfaces under magnetic perturbations. In chapter 3 we present a more technical treatment of the MHD equilibrium problem in an axisymmetric situation. We give special emphasis on the semi-analytical approach to the equilibrium based on specified arbitrary functions, also we present comparisons between our approach and the equilibrium reconstruction by the EFIT code. In Chapter 4 we present a generic description of the magnetic field based on Biot-Savart integrals and its numerical implementation. Then we introduce a method for adjusting non-linear parameters of a system of filamentary currents that describe the magnetic field from the plasma response and a numerical routine developed for calculating high-resolution invariant manifolds of the magnetic field. In Chapter 5 we utilize the developed methods to predict the heat pattern of a real tokamak discharge based on the magnetic probes measurements, and finally compare it with the experimental profiles of heat flux to the divertor plates, with a reasonable agreement. In Chapter 6 we present our conclusions and perspectives.

# Chapter 2

## Magnetic fields and Hamiltonian Systems

Perhaps the most important concept of this work is the Hamiltonian nature of the magnetic field lines. This gives us a framework to interpret the magnetic topology in terms of invariant surfaces and also allows us to understand better the complex geometries that emerge when the continuous symmetry of the time-like spatial variable is broken. Such information allows us to make geometrical predictions over the magnetic field invariants that define the plasma edge and the resonant structures inside the plasma. Consequently we start this work by demonstrating the Hamiltonian nature of the magnetic field lines for periodic confinement devices like tokamaks and stellarators.

### 2.1 The Hamilton equations

The equations of Hamiltonian Dynamics can be obtained from the variational principle [Goldstein et al. (2000); Arnold (1973)], when the action

$$J = \int_a^b dt \left[ \vec{p} \cdot \dot{\vec{q}} - \mathcal{H}(\vec{q}, \vec{p}, t) \right], \quad (2.1)$$

becomes stationary, i.e.  $\delta J = 0$ . In general, the solution to this problem gives us the Euler-Lagrange equations for each variable of the problem (see Appendix A.1). The integrand of the functional corresponds to the Lagrangian of the mechanical system

$$\mathcal{L}(\vec{q}, \dot{\vec{q}}, t) = \vec{p} \cdot \dot{\vec{q}} - \mathcal{H}(\vec{q}, \vec{p}, t), \quad (2.2)$$

where  $\vec{q} = \{q_i\}$  are the coordinates,  $\dot{\vec{q}} = \{\dot{q}_i\}$  the velocities and  $\vec{p} = \{p_i\}$  the momenta, defined from the Lagrangian as  $p_i = \partial \mathcal{L} / \partial \dot{q}_i$ . The index  $i = 1, \dots, N$  correspond to each

degree of freedom of the mechanical system [Goldstein et al. (2000)]. In general, the Euler-Lagrange equations take the form

$$\frac{\partial f}{\partial y_j} - \frac{d}{dt} \frac{\partial f}{\partial \dot{y}_j} = 0. \quad (2.3)$$

Upon identifying  $f(\vec{y}, \dot{\vec{y}})$  with  $\mathcal{L}(\vec{q}, \dot{\vec{q}})$  in (2.2), and the variables as  $(y_i, y_{N+i}) = (q_i, p_i)$  for  $i = 1, 2, \dots, N$ , we obtain the Hamilton equations

$$\frac{dq_i}{dt} = \frac{\partial \mathcal{H}}{\partial p_i}, \quad \frac{dp_i}{dt} = -\frac{\partial \mathcal{H}}{\partial q_i}, \quad (2.4)$$

The structure of these equations confers to the system some remarkable properties as the conservation of the phase-space volume  $d^N q d^N p$  that forbids the existence of attracting sets or transient behaviors that are characteristic of dissipative systems.

## 2.2 Magnetic field lines from a variational principle

From the divergence free nature of the magnetic field, there is a vector potential  $\vec{A}(\vec{r}, t)$  such that the magnetic field  $\vec{B}(\vec{r}, t)$  can be obtained as

$$\vec{B} = \nabla \times \vec{A}. \quad (2.5)$$

Now, consider the path  $\vec{r}(s)$  connecting the points  $a$  and  $b$  in  $\mathbb{R}^3$ , where  $s$  is an arbitrary parameter running from  $s_0$  to  $s_f$  that determines the position along the path (Fig. 2.1).

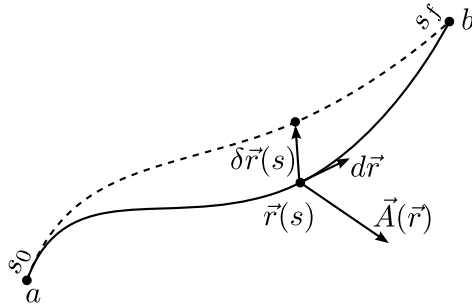


Figure 2.1: An arbitrary path  $\vec{r}(s)$  between  $a = \vec{r}(s_0)$  and  $b = \vec{r}(s_f)$ , and the varied path  $\vec{r}(s) + \delta\vec{r}(s)$  joining the same points.

Then we define the following functional of the path [Cary and Littlejohn (1983)]

$$\mathcal{J}[\vec{r}(s)] = \int_a^b \vec{A}(\vec{r}) \cdot d\vec{r} = \int_a^b (A_i \dot{x}_i) ds, \quad (2.6)$$

where  $\dot{x}_i = dx_i/ds$ , and the Einstein convention is being used. Now, let us investigate the

path that extremizes the action, i.e. such that the variation becomes stationary  $\delta\mathcal{J} = 0$ . For this, let us introduce the varied path  $\vec{r}(s) + \delta\vec{r}(s)$ , such that  $\delta\vec{r}(s)$  is small, and the variation of the action takes the form

$$\delta\mathcal{J} = \int_a^b A_i(\vec{r} + \delta\vec{r})(\dot{x}_i + \delta\dot{x}_i)ds - \int_a^b A_i(\vec{r})\dot{x}_i ds. \quad (2.7)$$

Notice that the integration limits were not altered because we want to know the path connecting these points and extremizing the action, and this implies that  $\delta x_i(s_a) = \delta x_i(s_b) = 0$ . Removing second order terms in  $\delta\vec{r}(s)$ , and requiring  $\delta\mathcal{J} = 0$  we obtain

$$\int_a^b \left[ \delta x_j \frac{\partial A_i}{\partial x_j} \dot{x}_i + A_i \delta \dot{x}_i \right] ds = 0. \quad (2.8)$$

Using  $\delta \dot{x}_i = \frac{d}{ds} \delta x_i$  and integrating by parts we have

$$\int_a^b \left[ \dot{x}_i \left( \frac{\partial A_i}{\partial x_j} - \frac{\partial A_j}{\partial x_i} \right) \right] \delta x_j ds - [A_i \delta x_i]_a^b = 0. \quad (2.9)$$

Recalling that the variation vanishes at the integration limits and using vector notation the integral takes the form

$$\int_a^b \left[ \frac{d\vec{r}}{ds} \times (\nabla \times \vec{A}) \right] \cdot \delta\vec{r} ds = 0. \quad (2.10)$$

Since the variation  $\delta\vec{r}(s)$  is arbitrary the integral can only vanish if the integrand vanishes everywhere along the path. Replacing  $\vec{B} = \nabla \times \vec{A}$  in the vanishing integrand we obtain the equation that describes the path that extremizes the action

$$\frac{d\vec{r}}{ds} \times \vec{B} = 0. \quad (2.11)$$

This indicates that the path elements must be parallel to the magnetic field, or in other words, the path is a magnetic field line. This implies that the integrand in the functional presented in (2.6) condenses naturally the magnetic field lines information, just like the Lagrangian of a mechanical system, and it can be used to study the symmetries associated to the field lines.

## 2.3 Magnetic field lines as a Hamiltonian system

The derivation just presented may look like a mathematical artifact unnecessary to describe the magnetic topology, however it provides a variational picture of the field lines

that leads naturally to their Hamiltonian structure. Before presenting the numerical methods to trace the magnetic field lines it is important to understand how the divergence free nature of the magnetic field leads to the Hamilton equations, so that we can use a well known framework from dynamical systems theory for interpreting the geometry of the magnetic field lines. Provided this, we can study the magnetic field lines as a one and a half degrees of freedom system, even when the magnetic field evolves in time.

To start, consider the functional in (2.6) for some arbitrary curve  $\Gamma$  in  $\mathbb{R}^3$ . Without loss of generality, we will use cylindrical coordinates  $(R, \phi, z)$  to illustrate this demonstration. In this system  $d\vec{r} = dR\hat{R} + dz\hat{z} + Rd\phi\hat{\phi}$  and the functional takes the form

$$\mathcal{J}[\Gamma] = \int_a^b \left( A_R \frac{dR}{ds} + A_z \frac{dz}{ds} + RA_\phi \frac{d\phi}{ds} \right) ds. \quad (2.12)$$

Intuitively speaking, if a field line curls around the  $z$  axis in some arbitrary fashion, but without reversing, it can be described by two differential equations with  $\phi$  being the independent variable. For periodic fusion devices like tokamaks and stellarators this is the case, since the confining magnetic field lines never reverse inside the plasma volume, i.e. the quantity  $\vec{B} \cdot \hat{\phi} = B_\phi$  does not change sign inside the plasma. Instead of using an arbitrary scalar  $s$  to parametrize the field lines we can use the toroidal angle, from which the functional becomes

$$\mathcal{J}[\Gamma] = \int_a^b \left( A_R \frac{dR}{d\phi} + A_z \frac{dz}{d\phi} + RA_\phi \right) d\phi. \quad (2.13)$$

As we know, the magnetic field  $\vec{B} = \nabla \times \vec{A}$  is invariant under gauge transformations of the form  $\vec{A} \rightarrow \vec{A} + \nabla\chi$ , and this only adds a constant factor to the functional that cancels out when extremizing. We use this to simplify the functional by choosing  $\chi(\vec{r})$  satisfying  $\partial\chi/\partial R = -A_R$  and the previous equation becomes

$$\mathcal{J}[\Gamma] = \int_a^b \left[ \left( A_z + \frac{\partial\chi}{\partial z} \right) \frac{dz}{d\phi} + R \left( A_\phi + \frac{1}{R} \frac{\partial\chi}{\partial\phi} \right) \right] d\phi, \quad (2.14)$$

In this form, the functional only involves two terms and contains the same information. Now, let us perform the following identification

$$p = A_z + \frac{\partial\chi}{\partial z}, \quad (2.15)$$

$$q = z, \quad (2.16)$$

$$t = \phi, \quad (2.17)$$

which are three independent quantities, provided that they define uniquely the position

vector  $\vec{r}$  in a given domain  $\Omega \in \mathbb{R}^3$ . Then, if we define  $\mathcal{H}(p, q, t) = RA_\phi + \partial_\phi \chi$  as a function of these three numbers, we obtain the expected representation for the functional

$$\mathcal{J}[\Gamma] = \int_a^b [p\dot{q} - \mathcal{H}(p, q, t)] dt, \quad (2.18)$$

in complete analogy with (2.24), where  $RA_\phi + \partial_\phi \chi$  plays the role of the Hamiltonian function and  $(q, p)$  are the canonical coordinate and momentum which define the spatial location of the field line in  $\mathbb{R}^3$ .

Although we have formally obtained the Hamiltonian function that governs the geometry of the field lines the identification of the gauge function  $\chi(\vec{r})$  was not made explicit. This deficiency however does not precludes us from calculating the field lines numerically, since the equation (2.11) gives a simple non-canonical representation of the field lines that is much easier to code for numerical calculations.

## 2.4 The tokamak magnetic field

In this section we will introduce the main properties of the magnetic field used to confine the hot plasma in a tokamak device, and the discussion about MHD equilibrium will be left for the next chapter. The magnetic field in a tokamak device results from the combination of the fields produced by a set of external currents and the field due to the plasma current itself. In a first approximation, the charged particles are confined by a combination of a strong toroidal magnetic and a poloidal field that restrict their motion to helical paths curled around the magnetic field lines [Chen (1984)]. The ionized plasma inside a tokamak chamber plays the role of the secondary coil in a transformer. The electromotive force created by a varying current in the primary coil (Fig. 2.2) leads to ohmic heating of the plasma while inducing the toroidal plasma current that creates part of the poloidal magnetic field. In addition to this field the set of poloidal field coils is used to shape the plasma and create the vertical magnetic field that balances the hoop force that tends to expand the plasma outwards [Freidberg (2004)].

The toroidal magnetic field is modeled to be axisymmetric but it presents small ripples near its sources due to their discrete nature. Also, a small reduction from the expected vacuum field intensity is due to the plasma diamagnetism resulting from the combined gyro-motion of the charged particles around the field lines.

In cylindrical coordinates, any axisymmetric magnetic field can be written in terms of the vector potential as

$$\vec{B} = -\hat{R} \frac{\partial A_\phi}{\partial z} + \hat{\phi} \left( \frac{\partial A_R}{\partial z} - \frac{\partial A_z}{\partial R} \right) + \frac{\hat{z}}{R} \frac{\partial (RA_\phi)}{\partial R}, \quad (2.19)$$

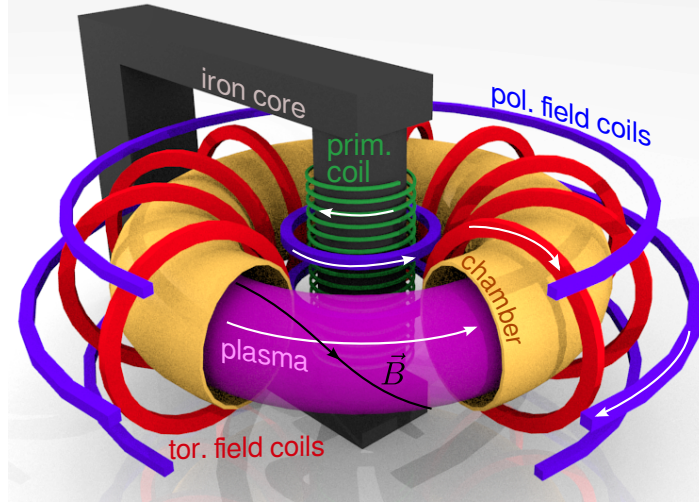


Figure 2.2: Representation the main magnetic field sources in a tokamak configuration. The arrow in the primary coil (green) indicates the direction of variation of the primary current. The magnetic flux change in the iron core (black) creates a positive toroidal electric field in the plasma volume that leads to the ohmic portion of the plasma current. The arrows in the poloidal field coils (blue) indicate the direction of the currents that create the vertical field that cancels the hoop force. The toroidal field coils around the chamber (red) create most of the magnetic field required to confine the charged particles and the conducting chamber provides an additional stabilizing effect by restricting the diffusion of magnetic field lines towards the chamber. The combined toroidal and poloidal magnetic fields results in helical field lines (black line) spanning nested toroidal surfaces inside the plasma.

where the axisymmetry is imposed by requiring  $\partial_\phi = 0$ . The toroidal component of the magnetic field is  $B_\phi = (\partial_z A_R - \partial_R A_z)$ . Then, we define the functions  $\psi(R, z) = RA_\phi(R, z)$  and  $F(R, z) = RB_\phi$ , so that the magnetic field takes the form

$$\vec{B}(R, z) = \nabla\psi \times \nabla\phi + F\nabla\phi. \quad (2.20)$$

Notice that  $\vec{B} \cdot \nabla\psi = 0$ , then, the value of  $\psi$  does not change along the magnetic field lines and can be used to label the magnetic surfaces, i.e. the magnetic field lines extend along the level surfaces  $\psi(R, z) = \text{const}$ . In a similar fashion, we can use the differential Ampere's law  $\nabla \times \vec{B} = \mu_0 \vec{j}$ , to write the current density inside the plasma as

$$\vec{j}(R, z) = \mu_0^{-1} \nabla F \times \nabla\phi + j_\phi \hat{\phi}. \quad (2.21)$$

In analogy with the magnetic field, the current density lines extend along  $F(R, z) = \text{const}$ . surfaces. In the next chapter it will be shown that for the simplest case in which the kinetic pressure is a scalar and there is no significant plasma flow, the surfaces  $F = \text{const}$ . coincide with the magnetic surfaces, but for now we use this without proof.

For tokamak discharges, the magnetic surfaces constitute a continuous family of nested toroidal surfaces. The magnetic field on each surface can be characterized with the rotational transform  $\iota(\psi)$ , or the safety factor  $q(\psi)$  defined as

$$q(\psi) = \frac{d\phi}{d\vartheta} = \frac{1}{\iota(\psi)}, \quad (2.22)$$

where  $\vartheta$  is a non-uniform poloidal angle defined so that the field lines become straight lines in the plane  $\vartheta - \phi$  (Fig. 2.3) [Kadomtsev (1992)]. The safety factor measures the ratio between toroidal and poloidal displacements for any field line in a given magnetic surface. It can take any real value inside the plasma, usually  $1 \lesssim q \lesssim 6$  for limiter discharges, but  $q$  can be very large in small regions of diverted discharges.

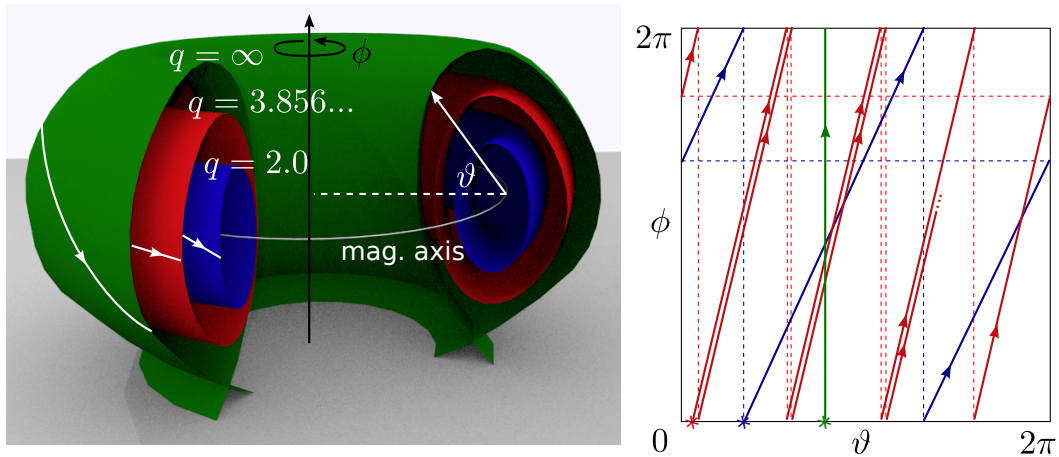


Figure 2.3: Three instances of magnetic surfaces in the real space (left) and the  $\vartheta - \phi$  space. Colors in the right correspond to the surfaces in the left and the asterisk indicate the starting point of the field lines. The blue surface is the rational  $q = 2$ , then, its field lines complete two toroidal turns in one poloidal turn and close exactly. Therefore we need infinite field lines to fill the blue surface in the left. The red surface is the irrational surface  $q = 3.856\dots$ , its field lines complete almost four toroidal cycles per poloidal cycle but they never close, in consequence, a single field line fills densely the red surface. The green surface is a separatrix surface and its field lines never close because the poloidal field  $\nabla\psi \times \nabla\phi$  vanishes at a single point (the X-point) in the toroidal section. As for rational surfaces, an infinite number of field lines are required to fill the surface.

For most magnetic surfaces  $q$  takes irrational values, implying that a single field line fills densely its corresponding magnetic surface without closing. However, there is an infinite countable (in a mathematical sense) set of rational surfaces where  $q = m/n$ , then the field lines close after  $m$  toroidal turns or  $n$  poloidal turns. In this case the magnetic surfaces are not spanned by a single field line, but require infinite lines to fill-up densely. In Fig. 2.3 we depict three kinds of magnetic surfaces of regular tokamak discharges, rational, irrational and separatrix, and their representation in the space  $\vartheta - \phi$ . The poloidal angle

is measured from the magnetic axis (the innermost magnetic field line) and does not correspond to the geometrical poloidal angle. Like rational surfaces, separatrix surfaces are spanned by infinite field lines, but these can not complete a single poloidal cycle. It is worth noticing that a diverging safety factor (or a vanishing rotational transform) does not imply absence of poloidal motion (as appears in the  $\vartheta - \phi$  plane) but indicates that a poloidal cycle is never completed, so, in some way  $\vartheta$  is ill defined for this kind of surface.

### 2.4.1 Resonances and magnetic islands

In the following we show a simple consequence of the Hamiltonian nature of the magnetic field when we are in an almost symmetric configuration. The following formal statements are not required for the magnetic field calculations, but provide valuable insight on the nature of the so called magnetic islands and homoclinic lobes that play a central role in this work. Since  $\phi$  corresponds to the time in (2.17), the rotational transform  $\iota(\psi) = d\vartheta/d\phi$  of the magnetic surface corresponds to the frequency of the Hamiltonian system with  $\mathcal{H}(q, p) = RA_\phi + \partial\chi/\partial\phi$ . Invoking the axisymmetry of the magnetic configuration the Hamiltonian becomes

$$\mathcal{H}(q, p) = RA_\phi = \psi(R, z), \quad (2.23)$$

where  $(q, p) = (z, A_z + \partial\chi/\partial z)$ , and the gauge function  $\chi$  satisfies  $\partial\chi/\partial R = -A_R$ . In addition, we can write the Hamilton equations in terms of action-angle variables with  $\vartheta$  the angle and  $\mathcal{I}(\psi)$  the action of the corresponding magnetic surface. Such action corresponds to the phase-space area enclosed by the magnetic surface

$$\mathcal{I}(\psi) = \oint pdq = \oint \left( A_z + \frac{\partial\chi}{\partial z} \right) dz, \quad (2.24)$$

where the integral is calculated at an arbitrary toroidal angle  $\phi = \text{const.}$  along the section of the magnetic surface. In general, the relation  $\mathcal{I}(\psi)$  can be inverted to obtain the magnetic flux  $\psi$  in terms of  $\mathcal{I}$ . This allows us to write the the Hamiltonian function in terms of the action  $\mathcal{H}(\mathcal{I}) = \psi(\mathcal{I})$ , and to calculate the rotational transform  $\iota(\psi)$  using the Hamilton equations for  $(\vartheta, \mathcal{I})$

$$\frac{d\vartheta}{d\phi} = \frac{\partial\mathcal{H}}{\partial\mathcal{I}} = \frac{d\psi}{d\mathcal{I}} \quad (2.25)$$

$$\frac{d\mathcal{I}}{d\phi} = -\frac{\partial\mathcal{H}}{\partial\vartheta} = 0. \quad (2.26)$$

With this we have  $q(\psi) = d\mathcal{I}/d\psi$ , and the second Hamilton equation results from  $\vartheta$  being a cyclic coordinate in action-angle variables. It simply states the fact that, by definition  $\mathcal{I}$  does not change along the field line, which in turn indicates that it is a function of

the magnetic flux  $\psi$  alone. We can view any axisymmetric discharge in the phase space  $\vartheta - \mathcal{I}$  as a collection of nested invariant tori with different frequencies [Lichtenberg and Lieberman (1983)]. In Fig. 2.4-left, we show the invariant surfaces or invariant tori in the  $\vartheta - \mathcal{I}$  space for an hypothetical discharge where  $q = 1$  occurs near the magnetic axis. Three main rational surfaces are highlighted as they play an important role in the development of new magnetic topologies.

Now, consider a *small* departure from axisymmetry condensed in an additive magnetic field  $\vec{B}_1(R, z, \phi)$  that may be composed by the oscillating part of the toroidal field (due to discreteness of the coils), the field created by resonant magnetic perturbation (RMP) coils, that will be discussed later, and the field created by non-axisymmetric currents developing inside the plasma through MHD mechanisms. Regardless of the sources of such field, there are unavoidable topological features coming from the Hamiltonian nature of the field lines and these can be understood in terms of Secular Perturbation Theory [Lichtenberg and Lieberman (1983)].

To put things in proper context consider the vector potential  $\vec{A}_1(R, z, \phi)$ , such that  $\vec{B}_1 = \nabla \times \vec{A}_1$ , then we define the perturbation Hamiltonian

$$\mathcal{H}_1 = RA_{1,\phi} + \frac{\partial \chi_1}{\partial \phi}, \quad (2.27)$$

where  $\partial_R \chi_1 = -A_{1,R}$ . Formally, this Hamiltonian can be written in terms of the action-angle variables of the axisymmetric one  $\mathcal{H}_0(\mathcal{I})$ , to obtain the full Hamiltonian determining the geometry of the field lines in the non-axisymmetric situation

$$\mathcal{H}(\mathcal{I}, \vartheta, \phi) = \mathcal{H}_0(\mathcal{I}) + \varepsilon \mathcal{H}_1(\mathcal{I}, \vartheta, \phi). \quad (2.28)$$

By construction,  $\mathcal{H}_1(\mathcal{I}, \vartheta, \phi)$  is a periodic function of  $\vartheta$  and  $\phi$  and admits a Fourier decomposition of the form

$$\mathcal{H}_1(\mathcal{I}, \vartheta, \phi) = \sum_{m,n} H_{m,n}(\mathcal{I}) \cos(m\vartheta - n\phi + \varphi_{m,n}). \quad (2.29)$$

Near the rational surface with  $q = m/n$  the component  $H_{m,n}$  of the asymmetric field becomes stationary respect to the unperturbed field lines. This resonance between the unperturbed field and the Fourier components of  $\mathcal{H}_1$  breaks the rational invariant tori and replace them with chains of magnetic islands of varying width. A detailed description of the mathematical aspects required to describe this phenomena is provided in [Lichtenberg and Lieberman (1983)]. After the symmetry break, only the field lines passing through the centers (elliptic points) and saddles (hyperbolic points) of the magnetic islands maintain the original property of the field lines in the unperturbed tori, i.e. closing after a

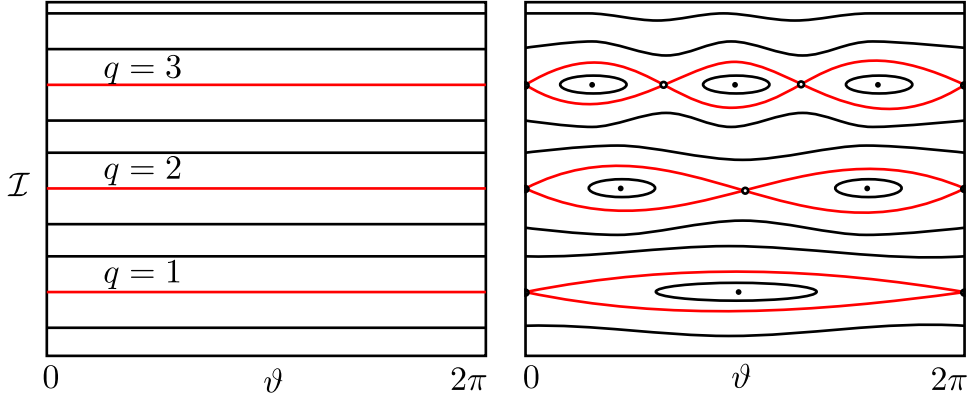


Figure 2.4: Poincaré section of the invariant tori in the  $\vartheta - \mathcal{I}$  space (left) and the resultant primary magnetic islands in the same space after breaking the axial symmetry. The separatrix chaos around the magnetic islands is not shown in this figure.

determined number of toroidal and poloidal cycles, however, the new field lines inside the islands may be irrational respect to their helical center and span new tori enclosing the center of the resonance. This can be understood as being a degeneracy remotion due to the symmetry break.

To illustrate this section, let us discuss the magnetic topology created by the combination of a vertical current  $I_1$  and a circular current  $I_2$  (Fig. 2.5). The vertical current acts as the source for the azimuthal (or toroidal) magnetic field, while the circular one leads to a poloidal field. The resulting magnetic field lines follow helical paths that encircle the circular and vertical currents simultaneously, spanning a toroidal magnetic surface when the safety factor is irrational.

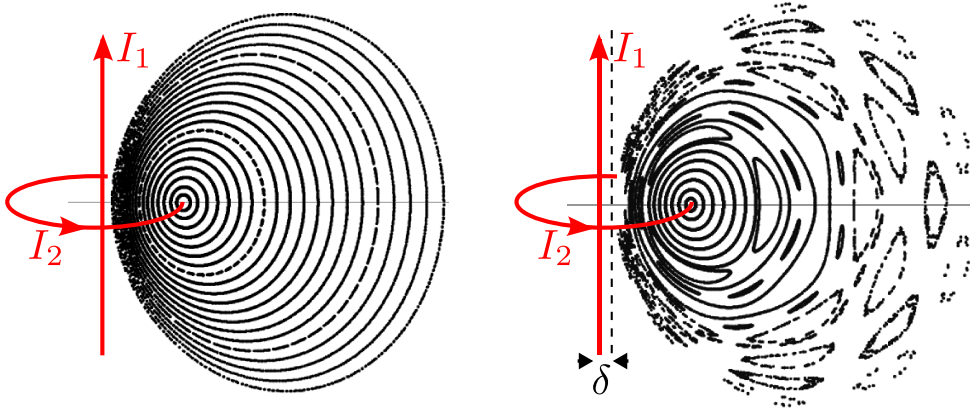


Figure 2.5: Vacuum magnetic field islands created by breaking weakly the axial symmetry of the source currents. The poloidal magnetic field is created by a circular current in the plane  $z = 0$  and the azimuthal field is due to an infinite vertical current passing through the center of the circle in the axisymmetric case and near the center in the non-axisymmetric one.

In Fig. 2.5 we show the Poincaré section of several magnetic field lines in the ax-

isymmetric and non-axisymmetric situations. The emergence KAM islands in the non-axisymmetric situation comes from the destruction of the rational surfaces in the axisymmetric situation due to the symmetry break. The emergence of these structures follows as a direct consequence of the divergence-free nature of the magnetic field and they are expected in situations where the source currents are distributed in space, like the plasma currents inside a tokamak or stellarator.

## 2.5 Plasma response

Until now, we have introduced the magnetic islands as a resonance phenomenon between an axisymmetric field and a periodic perturbation, independently of MHD considerations. In this sense, the formation of resonant islands does not require particularly strong asymmetries, and this seems to guarantee that arbitrarily small magnetic perturbations will lead to the formation of magnetic islands. However, additional restrictions over the physical system, like high conductivity, may impose strong restrictions over the island formation, that requires a finite resistivity for developing in the MHD framework [Goedbloed et al. (2010)].

It is, however, important to point out that the divergence-free nature of the magnetic field and its Hamiltonian structure are exact statements of fundamental nature, while the high conductivity and the fluid-like description are approximations that take place when moving from the statistical description of the many body system to the MHD description of the plasma [Bittencourt (2004)].

### 2.5.1 Magnetic helicity and topology

A fundamental idea that is ubiquitous in plasma physics textbooks, is that, in the ideal limit, the magnetic topology can not be modified by the plasma dynamics. However, it is rather difficult to find a clear demonstration of this important statement and we can not refer the reader to a standard textbook. To establish a clear connection of our previous discussion with the traditional presentation plasma physics we will devote some space to clarify these ideas in this section.

First of all, we need a physical or geometrical quantity that allows us to *quantify* the magnetic topology, i.e. the way in which the field lines are organized in a given volume of the plasma. For this we will introduce the topological concept of *linking number* and then relate it to the more general *helicity*, appropriate for continuous flows.

Consider two entangled filaments  $\Gamma_1$  and  $\Gamma_2$  in three dimensions, for instance Fig. 2.6.

If we follow the filament  $\Gamma_2$  it is clear that it pierces *four* times *any* surface delimited by  $\Gamma_1$ . The number of piercings or *linking number* is independent of the shape of the

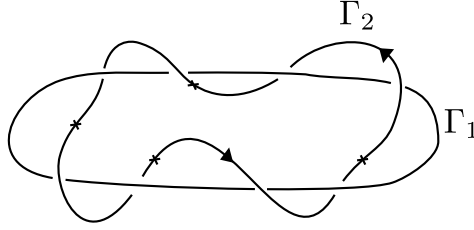


Figure 2.6: Two inter-linked filaments with linking number  $\lambda = 4$ . The small crosses indicate the intersection of  $\Gamma_2$  with a surface bounded by  $\Gamma_1$

filaments and characterizes the way in which  $\Gamma_1$  and  $\Gamma_2$  are mutually entangled. In this situation, it is easy to determine the linking number by inspection, but in most situations we need a more systematic method that does not involve counting piercings or crossings.

Let us use some known concepts to obtain a useful equation. Imagine for a moment that  $\Gamma_2$  carries a current  $I$  in the direction indicated by the arrows in Fig. 2.6. The magnetic field created by this current at an arbitrary location  $\vec{r}$  can be obtained from the Biot-Savart law

$$\vec{B}(\vec{r}) = \frac{\mu_0 I}{4\pi} \oint_{\Gamma_2} \frac{d\vec{r}_2 \times (\vec{r} - \vec{r}_2)}{|\vec{r} - \vec{r}_2|^3}. \quad (2.30)$$

This magnetic field can be used to determine the linking number by means of the Ampere's law in the circuit  $\Gamma_1$ . Notice that the current going through the surface limited by  $\Gamma_1$  is simply  $\lambda_{1,2}I$  and can be obtained by

$$\lambda_{1,2}I = \frac{1}{\mu_0} \oint_{\Gamma_1} \vec{B}(\vec{r}_1) \cdot d\vec{r}_1. \quad (2.31)$$

Inserting (2.30) into (3.2) we obtain a simple formula for the linking number between the filaments  $\Gamma_1$  and  $\Gamma_2$

$$\lambda_{1,2} = \frac{1}{4\pi} \oint_{\Gamma_1} \oint_{\Gamma_2} \frac{(\vec{r}_1 - \vec{r}_2) \cdot (d\vec{r}_1 \times d\vec{r}_2)}{|\vec{r}_1 - \vec{r}_2|^3}. \quad (2.32)$$

Notice that this equation only requires the trajectories of  $\Gamma_1$  and  $\Gamma_2$ , and the current in  $\Gamma_2$  was only introduced to take advantage of familiar concepts in magnetostatics. The resulting equation would be identical if the current was assumed to run along  $\Gamma_1$  instead of  $\Gamma_2$ .

With this equation in hand, consider that we have an arbitrary magnetic field  $\vec{B}(\vec{r})$  inside a given volume  $\Omega$  defined so that its bounding surface  $\Sigma$  is not pierced by any field line (i.e.  $\Sigma$  is a magnetic surface). Now, we want to characterize this magnetic volume by the number of linkages between *all* its field lines (see Fig. 2.7). This involves calculating the linking number between each pair of field lines in  $\Omega$ , but the number of field lines inside a volume is, non-countably infinite.

To avoid this difficulty consider that we subdivide  $\Omega$  in a large number of non-

overlapping flux tubes extending along the field lines (Fig. 2.7). Each tube carries a constant magnetic flux  $\Phi_i = \vec{B} \cdot d\vec{S}_i$  that quantifies the *amount* of field lines contained in it. Let us assume that the tube is sufficiently small so that its swarm of field lines won't spread or twist, i.e. any pair of field lines in the tube are not entangled. Provided this, the linking between the field lines in the tubes  $\Phi_i$  and  $\Phi_j$  is

$$\Lambda_{i,j} = \Phi_i \Phi_j \lambda_{i,j}, \quad (2.33)$$

where  $\lambda_{i,j}$  is the linking number between the one field line in the tube  $i$  and other in the tube  $j$ . Using (2.32) we obtain the total linking between the tubes  $i$  and  $j$

$$\Lambda_{1,2} = \frac{1}{4\pi} \oint_{\Gamma_i} \oint_{\Gamma_j} \frac{\vec{r}_{j,i}}{r_{j,i}^3} \cdot (\Phi_i d\vec{r}_i \times \Phi_j d\vec{r}_j), \quad (2.34)$$

where  $\vec{r}_{j,i} = \vec{r}_i - \vec{r}_j$  and  $r_{j,i} = |\vec{r}_{j,i}|$ .

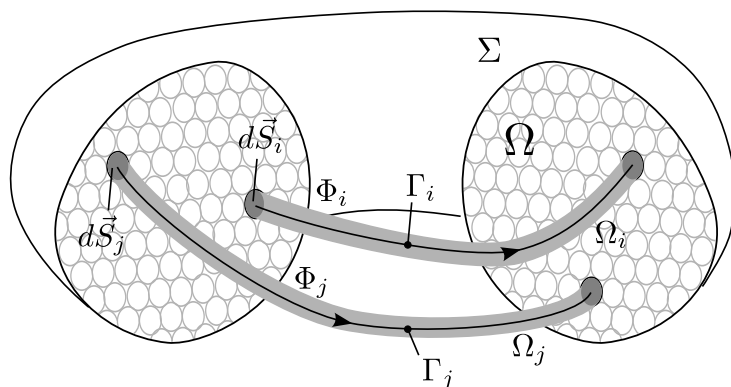


Figure 2.7: Space volume  $\Omega$  bounded by a magnetic surface  $\Sigma$  and subdivided in non-overlapping magnetic flux tubes.

Writing the magnetic flux as  $\Phi_i = \vec{B}(\vec{r}_i) \cdot d\vec{S}_i$ , where  $d\vec{S}_i$  is the transversal surface element of the tube  $\Phi_i$  at  $\vec{r}_i$ , and noticing that because  $d\vec{r}_i$  and  $\vec{B}(\vec{r}_i)$  are parallel, we can write  $\Phi_i d\vec{r}_i = \vec{B}(\vec{r}_i)(d\vec{r}_i \cdot d\vec{S}_i)$ , leading to

$$\Lambda_{i,j} = \frac{1}{4\pi} \int_{\Omega_i} \int_{\Omega_j} \frac{\vec{r}_{j,i}}{r_{j,i}^3} \cdot (\vec{B}(\vec{r}_i) \times \vec{B}(\vec{r}_j)) dV_i dV_j, \quad (2.35)$$

Where  $\Omega_i$  is the volume defining the  $i$ 'th flux tube. Now, recall that the full volume  $\Omega$  was subdivided in non-overlapping flux tubes. This means that adding the volume of each tube gives us the full volume integral. Consequently, the total linking between the field lines in the volume  $\Omega$  is given by

$$\Lambda(\Omega) = \sum_{i,j} \Lambda_{i,j} = \frac{1}{4\pi} \int_{\Omega} \int_{\Omega} (\vec{B}(\vec{r}) \times \vec{B}(\vec{r}')) \cdot \frac{\vec{r} - \vec{r}'}{|\vec{r} - \vec{r}'|} dV dV', \quad (2.36)$$

This double volume integral can be further reduced by using the magnetic vector potential as obtained from the combination of the Ampère's and Biot-Savart laws

$$\vec{A}(\vec{r}) = \frac{1}{4\pi} \int_{\Omega} \vec{B}(\vec{r}') \times \frac{\vec{r} - \vec{r}'}{|\vec{r} - \vec{r}'|^3} dV'. \quad (2.37)$$

Then, the total magnetic linking number, also known as *magnetic helicity*, takes the form

$$\Lambda(\Omega) = \int_{\Omega} [\vec{B}(\vec{r}) \cdot \vec{A}(\vec{r})] dV. \quad (2.38)$$

This elegant expression quantifies the form in which the field lines are organized inside the volume and provides a quantitative way to track topological changes inside  $\Omega$ . Having this in mind we can check under which conditions the plasma evolution leads to topological changes in the region of interest.

## 2.5.2 Evolution of the magnetic helicity

The magnetic helicity is an important quantity for plasma dynamics, as under ideal conditions it plays the role of a topological invariant and in the resistive case it changes at a considerable slower rate than the magnetic energy [Taylor (1986); Qin et al. (2012)]. Before understanding the physical consequences of this, let us determine the equations governing the helicity evolution.

In Appendix A.2, the evolution of a volume integral function is shown to depend on the integrand and on the movement of the bounding surface. In the case of the helicity the temporal change takes the form

$$\frac{d\Lambda}{dt} = \int_{\Omega} \frac{\partial}{\partial t} (\vec{B} \cdot \vec{A}) d^3\vec{r} + \oint_{\Sigma} (\vec{B} \cdot \vec{A}) \vec{v}_{\Sigma} \cdot d\vec{S}, \quad (2.39)$$

where  $\vec{v}_{\Sigma}$  is the velocity of the bounding surface. Using the Faraday's law  $\partial \vec{B} / \partial t = -\nabla \times \vec{E}$  and the single-fluid Ohm's law  $\vec{j} = \sigma(\vec{E} + \vec{v} \times \vec{B})$  [Freidberg (2004)], we show in Appendix A.3 that the evolution of the magnetic helicity is given by

$$\frac{d\Lambda}{dt} = -\frac{2}{\sigma} \int_{\Omega} (\vec{j} \cdot \vec{B}) d^3\vec{r} + \oint_{\Sigma} (\vec{A} \cdot \vec{B}) (\vec{v} - \vec{v}_{\Sigma}) \cdot d\vec{S}, \quad (2.40)$$

where  $\sigma$  is the isotropic conductivity and  $\vec{v}$  is the plasma flow velocity at the bounding surface  $\Sigma$ . This equation depends on both, the conductivity and the difference between the plasma flow velocity and the magnetic surface velocity. In the Appendix A.4 it is shown that in the ideal limit  $\sigma \rightarrow \infty$ , the single-fluid plasma flux velocity is equal to the magnetic surface velocity. This is just another form of the Alfvén's *frozen in*

*theorem* [Alfven (1942)], implying that both terms in the r.h.s of the previous equation vanish and the helicity is a constant of motion, i.e.

$$\Lambda(\Omega, t) = \text{constant}, \quad (2.41)$$

where the volume  $\Omega$  itself may evolve in time. This equation is valid for any plasma volume bounded by one or two magnetic surfaces, so that the previous results are also valid for a given plasma slab between two magnetic surfaces, and actually it is approximately true in the resistive case for a plasma slab containing irrational and non-resonant rational surfaces.

To summarize, for perfectly conducting plasmas, the magnetic topology can not change due to a symmetry break. Magnetic surfaces can be deformed but can not bifurcate to give rise to the magnetic islands as this involves changes in the helicity. This seems like a counter-intuitive result from the KAM theory point of view, where any arbitrarily small symmetry break will lead to the emergence of magnetic islands. However, from the MHD point of view, the helicity conservation on ideal configurations imposes strong topological bounds over the magnetic surfaces that must be provided by some sort of shielding phenomena, that cancels the resonant components of the magnetic field that give rise to the magnetic islands. This shielding is achieved through localized currents at the resonant surfaces that create a response field that cancels, locally, the resonant component of the applied external field that otherwise would cause the bifurcation of the rational magnetic surface [Park et al. (2009)].

### 2.5.3 Magnetic islands in plasmas

Now that we have discussed the topological implications of the high conductivity in plasmas it is clear that, in the context of MHD, emergence of KAM islands or magnetic islands in plasmas involves a finite resistivity, that provides a mechanism for changing the helicity and consequently in the magnetic topology. The reconnection process is very interesting but goes beyond the scope of this work (see [Biskamp (1994)]), however, in the case of interest, an infinite (but countable) number of rational surfaces exist in an axisymmetric MHD equilibrium. Each rational surface can be viewed as a neutral sheet when represented under appropriate helical coordinates. These sheets can be disrupted by a corresponding resonant component of a magnetic perturbation when the resistivity is finite, leading to the formation of magnetic islands. These islands correspond to self-consistent KAM surfaces formed by the perturbing Hamiltonian that accounts for the external magnetic perturbation and the plasma response simultaneously.

Consider a magnetic island formed around an unperturbed rational surface. In a first

approximation, let us consider the hydromagnetic equilibrium with negligible plasma flow, which is independent of the symmetry of the equilibrium configuration and takes the form

$$\vec{j} \times \vec{B} = \nabla p. \quad (2.42)$$

Noting that  $\nabla p \cdot \vec{B} = 0$ , it is clear that the kinetic pressure does not change along the magnetic field lines, then, the magnetic surfaces are isobaric. Now, consider that the magnetic field results from the combination of a large axisymmetric field  $\vec{B}_s$  and a small asymmetric field  $\delta\vec{B}$ , then we use the Ampere's law to define the axisymmetric current density  $\vec{j}_s$  for the corresponding axisymmetric field

$$\vec{j}_s = \mu_0^{-1} \nabla \times \vec{B}_s. \quad (2.43)$$

With this, the asymmetric part of the current density takes the form  $\delta\vec{j} = \vec{j} - \vec{j}_s$ . Now, in analogy with (2.42), we define the axisymmetric pressure gradient that satisfies  $\nabla p_s = \vec{j}_s \times \vec{B}_s$  and asymmetric part of the pressure takes the form  $\delta p = p - p_s$ .

Expliciting the symmetric and asymmetric parts, the general equilibrium can be written as

$$(\vec{j}_s + \delta\vec{j}) \times (\vec{B}_s + \delta\vec{B}) = \nabla(p_s + \delta p). \quad (2.44)$$

Since the symmetric parts satisfy independently the equilibrium condition the remaining terms must satisfy

$$\vec{j} \times \delta\vec{B} + \delta\vec{j} \times \vec{B} = \nabla\delta p. \quad (2.45)$$

where  $\vec{B}$  and  $\vec{j}$  are the complete magnetic field and current density.

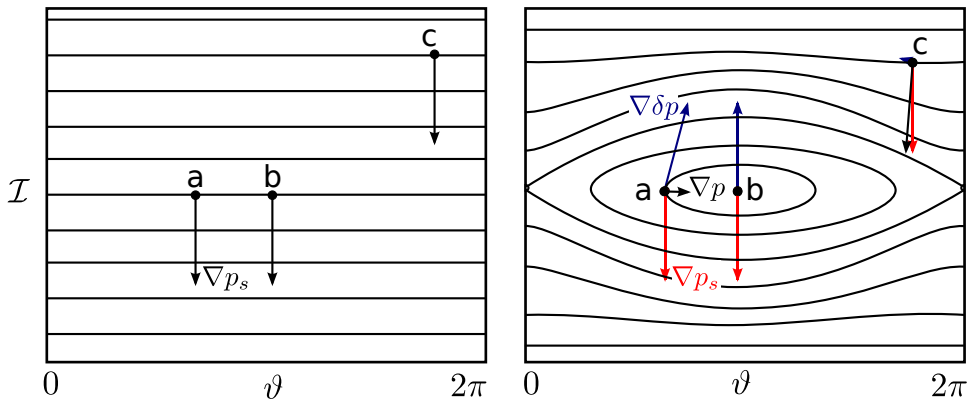


Figure 2.8: The isobaric surfaces in the action-angle space for the axisymmetric (left) and non-axisymmetric (right) configurations. The magnitude of the non-axisymmetric pressure gradient (blue) is responsible for defining the new isobarics, consequently, it must be of the order of the axisymmetric pressure gradient (red).

By definition, we know that  $\delta\vec{B}$  is small compared to  $\vec{B}$ , now, we need to understand

the magnitudes of the non-axisymmetric current density and pressure gradient. If we are at some magnetic surface that preserves its topology under the perturbation (like most irrational surfaces), the pressure gradient will continue to point to the interior of the surface, and the gradient of the non-axisymmetric pressure  $\nabla\delta p$ , can be considered to be small. From this, eq (2.45) can be satisfied with a small non-axisymmetric current  $\delta\vec{j}$ .

If we are in the island region, where the symmetric magnetic topology was altered, something different occurs. Since the magnetic surfaces inside the island are isobaric, the pressure gradient must point inwards or outwards these surfaces, then, the kinetic pressure must be changed drastically (see Fig. 2.8). This does not mean that the non-axisymmetric pressure  $\delta p$  is large, but that its variation is large over the narrow region of the magnetic islands. The gradient of the non-axisymmetric pressure  $\nabla\delta p$  is required to be of the order of the symmetric gradient  $\nabla p_s$ , so that the new isobarics surround the helical axis in the center of the islands.

Since the magnetic perturbation is small, by definition, the first term in (2.45) is not able to balance the RHS, and the second term, containing the non-axisymmetric current  $\delta\vec{j}$ , must be responsible for balancing the non-axisymmetric pressure gradient  $\nabla\delta p$ . To understand how this happens, notice that the total pressure gradient must vanish at the center of the island, then we have

$$(\vec{j}_s^* + \delta\vec{j}^*) \times (\vec{B}_s^* + \delta\vec{B}^*) = 0, \quad (2.46)$$

where the asterisk indicates evaluation at the center of the island. This equation requires the total current density to be parallel to the total magnetic field along the helical island axis. Since  $\delta\vec{B}$  is small, the response current must be large enough to drastically change the direction of  $\vec{j}$  to make it parallel to  $\vec{B}$ . In other words, the current  $\delta\vec{j}$  must be of the order of  $\vec{j}_s$  instead of a small perturbation to it (see Fig. 2.9).

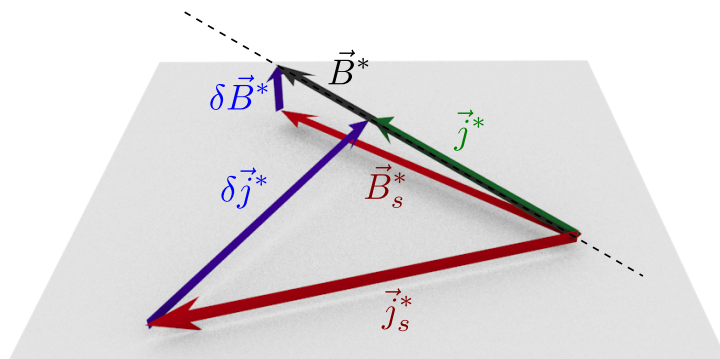


Figure 2.9: The total magnetic field  $\vec{B}^*$  must be parallel to the total current density  $\vec{j}^*$  along the magnetic axis (dashed). To obtain this, the non-axisymmetric current  $\delta\vec{j}$  must be of the order of the axisymmetric one.

The fact that a *large* non-axisymmetric current  $\delta\vec{j}$  is required to have an equilibrium magnetic island implies that  $\delta\vec{B}$  is not close to be a vacuum magnetic field, because it must satisfy  $\nabla \times \delta\vec{B} = \mu_0\delta\vec{j}$ . Actually, the non-axisymmetric magnetic field can be decomposed as

$$\delta\vec{B} = \delta\vec{B}_e + \delta\vec{B}_r, \quad (2.47)$$

where  $\delta\vec{B}_e$  is created by external sources and  $\delta\vec{B}_r$  is created by the plasma response. Clearly,  $\nabla \times \delta\vec{B}_r = \mu_0\delta\vec{j}$ , since the rotational of the field created externally must vanish.

However, these observations do not preclude a vacuum magnetic perturbation  $\delta\vec{B}_v$  to create magnetic islands. Just restricts the formation of *equilibrium* magnetic islands. In other words, adding arbitrary fields to the equilibrium field  $\vec{B}_s$  leads to the formation of non-equilibrium magnetic islands<sup>1</sup>, where the plasma response is not included [Evans et al. (2002); Wingen et al. (2009b)]. Such magnetic configurations are not necessarily self-consistent but are useful to estimate the magnetic topology in regions where the plasma is less dense and approaches the vacuum situation, like the plasma edge, also, it provides important information to model the plasma response, and describes well the real situation in relaxed plasma discharges where pressure gradients are small and the magnetic field and current density are nearly parallel [Taylor (1986); Qin et al. (2012)].

---

<sup>1</sup>The misleading term *vacuum islands* is widely used to identify these surfaces, but it is more appropriate to designate magnetic islands created entirely by vacuum fields, like those formed by the combination of a ring current and an infinite filament current passing *near* the ring's center.

# Chapter 3

## Axisymmetric MHD equilibrium

In this chapter we will discuss the description of the axisymmetric magnetic field that serves as a first approximation of the magnetohydrodynamic equilibrium of a highly conductive plasma, which is required to establish a background magnetic field to be perturbed by external and/or internal non-axisymmetric fields. In the following we discuss briefly the intensive numerical solution through Green's functions and the alternative, but restrictive, semi-analytical solution resulting from specific choices of the arbitrary functions, that turns the equilibrium a linear eigenvalue problem with a continuous family of solutions.

Let us start with the single fluid equations [Bittencourt (2004)] by assuming the equilibrium of the plasma flow, i.e.  $(\partial_t + \vec{v} \cdot \nabla)\vec{v} = 0$  in the momentum equation, and requiring vanishing time variations  $\partial_t = 0$ , for all quantities, which results in a reduced description of the hydromagnetic equilibrium of the plasma.

$$\nabla p = \vec{j} \times \vec{B}, \quad (3.1)$$

$$\nabla \times \vec{B} = \mu_0 \vec{j}, \quad (3.2)$$

$$\nabla \cdot \vec{B} = 0. \quad (3.3)$$

Equations (3.2) and (3.3) are just the Ampere's law in differential form and the divergence-free statement of the magnetic field. Equation (3.3) implies that  $\vec{B} = \nabla \times \vec{A}$ , which written in cylindrical coordinates can be rearranged as

$$\vec{B} = \left[ \hat{z} \frac{\partial}{\partial z} (RA_\phi) + \hat{R} \frac{\partial}{\partial R} (RA_\phi) \right] \times \frac{\hat{\phi}}{R} + B_\phi \hat{\phi}. \quad (3.4)$$

By analogy, we can write the Ampere's law in cylindrical coordinates and obtain a similar

representation for the plasma current density

$$\vec{j} = \mu_0^{-1} \left[ \hat{z} \frac{\partial}{\partial z} (RB_\phi) + \hat{R} \frac{\partial}{\partial R} (RB_\phi) \right] \times \frac{\hat{\phi}}{R} + j_\phi \hat{\phi}. \quad (3.5)$$

Using the gradient in cylindrical coordinates and defining the scalar quantities  $\psi = RA_\phi$  and  $F = RB_\phi$  we get that

$$\vec{B} = \nabla\psi \times \nabla\phi + B_\phi \hat{\phi}, \quad (3.6)$$

$$\vec{j} = \mu_0^{-1} \nabla F \times \nabla\phi + j_\phi \hat{\phi}, \quad (3.7)$$

where the vector fields are decomposed in their poloidal and toroidal components. This can be checked by noticing that the poloidal components  $\vec{B}_p = \nabla\psi \times \nabla\phi$  and  $\vec{j}_p = \nabla F \times \nabla\phi$ , rest in the plane perpendicular to  $\hat{\phi}$ .

Before we continue, it is instructive to determine clearly the nature of the scalar functions  $\psi$  and  $F$ , so that we have a better physical picture of them. First, from the relation  $\vec{B} = \nabla \times \vec{A}$ , the Stoke's theorem guarantees that

$$\int_{\Sigma} \vec{B} \cdot d\vec{S} = \oint_{\Gamma} \vec{A} \cdot d\vec{l}, \quad (3.8)$$

where  $\Sigma$  is a given open surface bounded by  $\Gamma$ , that can be composed by one or several simple curves (in the case of a multiply connected surface). Let us consider  $\Sigma$  to be any surface bounded by the circles  $\Gamma_0 = (R_0, z_0, \phi)$  and  $\Gamma = (R, z, \phi)$ , in cylindrical coordinates (Fig. 3.1).

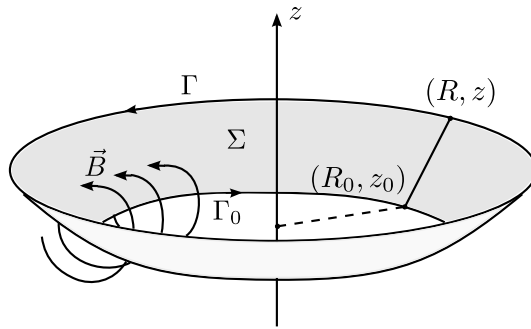


Figure 3.1: The surface  $\Sigma$  is bounded by two axisymmetric circles.

Notice that the LHS of (3.8) corresponds to the poloidal magnetic flux  $\Phi(\Sigma)$ , and the line elements of  $\Gamma_0$  and  $\Gamma$ , are purely toroidal  $d\vec{l} = \hat{\phi} R d\phi$ , then only the toroidal component of  $\vec{A}$  enters in the calculation, i.e.  $A_\phi = \psi/R$ . For this geometry,

$$\vec{A} \cdot d\vec{l} = \psi(R, z) d\phi, \quad (3.9)$$

where, by axial symmetry, the scalar function  $\psi$  is constant along bounding circles  $\Gamma_0$  and  $\Gamma$ , and we obtain the relation

$$\Phi_B(\Sigma) = 2\pi[\psi(R, z) - \psi(R_0, z_0)]. \quad (3.10)$$

Since only the derivatives of  $\psi$  have physical meaning we can choose  $\psi$  to be zero at an arbitrary location. For instance we can define  $\psi(R_0, z_0) = 0$  at the plasma-vacuum interface (plasma edge), so that  $\psi(R, z)$  becomes directly proportional to the poloidal magnetic flux measured from this position

$$\psi(R, z) = \frac{\Phi_B(\Sigma)}{2\pi}. \quad (3.11)$$

Proceeding in the same fashion for the relation  $\mu_0 \vec{j} = \nabla \times \vec{B}$  we obtain the similar relation

$$F(R, z) = \mu_0 \frac{\Phi_j(\Sigma)}{2\pi}, \quad (3.12)$$

where  $\Phi_j(\Sigma)$  is the current density flux through  $\Sigma$ , i.e. the poloidal plasma current passing between the magnetic axis and the circle  $(R, z)$ . In the following we use the terms *poloidal magnetic flux* for  $\psi(R, z)$  and *poloidal plasma current* for  $F(R, z)$  because of their close relation to the exact fluxes.

Replacing the representations (3.6) and (3.7) in (3.1) we obtain

$$\vec{j}_p \times \vec{B}_p = 0, \quad (3.13)$$

$$\vec{j}_p \times \vec{B}_\phi + \vec{j}_\phi \times \vec{B}_p = \nabla p, \quad (3.14)$$

where it was required that  $\nabla p$  does not have a  $\phi$  component due to the axial symmetry. Equation (3.13) implies that  $\vec{B}_p$  and  $\vec{j}_p$  are parallel, which in turn implies that  $\nabla\psi$  and  $\nabla F$  are always parallel inside the plasma. Consequently, the level curves  $F = \text{const.}$  and  $\psi = \text{const.}$  passing through a given point must be the same, i.e.  $F$  is a function of  $\psi$  and vice-versa.

$$\nabla F = \frac{dF}{d\psi} \nabla\psi. \quad (3.15)$$

Replacing this in (3.14) and using  $B_\phi = F(\psi)/R$  we obtain

$$\left( j_\phi - \frac{F}{\mu_0 R} \frac{dF}{dR} \right) \frac{\nabla\psi}{R} = \nabla p, \quad (3.16)$$

This equation implies that the kinetic pressure gradient is also parallel to  $\nabla\psi$  and by the same reasoning used with the poloidal current, we can show that the kinetic pressure  $p$  is

a function of  $\psi$ , then  $\nabla p = \frac{dp}{d\psi} \nabla \psi$ . Leading to the well known expression for the toroidal current density

$$j_\phi = R \frac{dp}{d\psi} + (\mu_0 R)^{-1} F \frac{dF}{d\psi}. \quad (3.17)$$

This representation of the toroidal current density depends on two arbitrary functions  $p(\psi)$  and  $F(\psi)$  that characterize the kinetic and magnetic force balance and define all the plasma parameters. However, the toroidal current is also the source of the poloidal magnetic field  $\vec{B}_p$ , and its resulting magnetic flux  $\psi$ . This relation can be established using the Coulomb gauge  $\nabla \cdot \vec{A} = 0$ , in the Ampere's law written in terms of the vector potential

$$\nabla^2 \vec{A} = -\mu_0 \vec{j}. \quad (3.18)$$

Using cylindrical coordinates, removing terms containing  $\partial_\phi$ , and replacing  $A_\phi = \psi/R$ , the toroidal component of this equation becomes

$$\left( \frac{\partial^2}{\partial R^2} - \frac{1}{R} \frac{\partial}{\partial R} + \frac{\partial^2}{\partial z^2} \right) \psi(R, z) = -\mu_0 R j_\phi. \quad (3.19)$$

At this point, we can use (3.17) to relate the spatial variation of the poloidal flux with the kinetic pressure and poloidal plasma current, which leads to the Grad-Shafranov equation [Shafranov (1966); Grad and Rubin (1958)] without plasma flows

$$\left( \frac{\partial^2}{\partial R^2} - \frac{1}{R} \frac{\partial}{\partial R} + \frac{\partial^2}{\partial z^2} \right) \psi(R, z) = -\mu_0 R^2 \frac{dp}{d\psi} - F \frac{dF}{d\psi}. \quad (3.20)$$

The compact form of (3.20) must not be underestimated, as the arbitrary functions  $p(\psi)$  and  $F(\psi)$  often lead to non-linear forms of the Grad-Shafranov equation that can only be solved numerically. For particular choices of  $p$  and  $F$ , however, the equation becomes linear and can be solved analytically by separation of variables, so that the poloidal magnetic flux becomes a linear superposition of a suitable number of special functions. Also, approximate solutions of this problem for circular plasmas with large aspect ratio  $R_0/a$  can be found in the literature [Freidberg (2004)], and provide important rules of thumb for the tokamak design and operation.

### 3.1 Boundary conditions

Before we enter in more details about the solution of the Grad-Shafranov equation (3.20), it is important to establish appropriate boundary conditions for the poloidal magnetic flux  $\psi$ .

First of all, a combination of vacuum magnetic and electric fields is required to shape,

confine and heat the plasma. The plasma current is created by electromagnetic induction due to a time-dependent current applied to the primary winding (Fig. 3.2), that creates a toroidal electric field that ionizes and subsequently heats the plasma by Joule effect. To restrict the motion of the charged particles inside the chamber a strong toroidal magnetic field is created by a relatively large set of toroidal field coils. This puts the particles into cyclotronic motion around the field lines and reduces the interaction with the vacuum chamber, creating a plasma column.

The shaping and stabilizing magnetic field is provided by the poloidal field coils that create the vertical field that counteracts the hoop forces [Freidberg (2004)] and mold the plasma edge to improve its stability properties (Fig. 3.2). In addition to this, the toroidal conducting chamber provides an automatic feedback control of plasma oscillations since it restricts (or delays) the magnetic field diffusion outside the plasma resulting in an increased magnetic pressure between the plasma and the chamber when the plasma column moves towards the chamber.

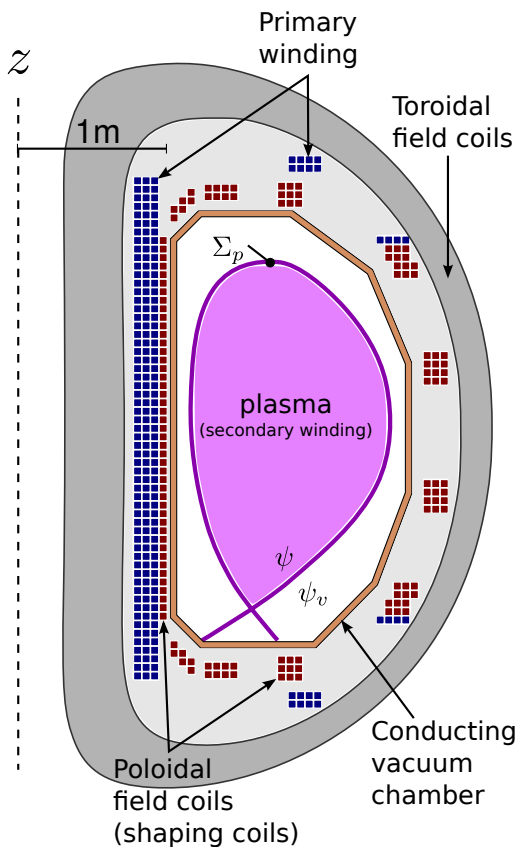


Figure 3.2: Cross section of the DIII-D tokamak presenting the sources of poloidal and toroidal magnetic field. The blue filaments correspond to the primary winding of the transformer, which creates the inductive electric field that drives the plasma current. The plasma itself plays the role of the secondary winding. The red coils (here discretized) are the sources of poloidal field that stabilizes the plasma column and shape it. The large toroidal field coils are, by definition, non-axisymmetric, but in large numbers create an almost axisymmetric toroidal field for confining the charged particles.

When a successful confinement is reached, the plasma occupies a well defined toroidal volume in space. By definition, the poloidal magnetic flux  $\psi$  must be a continuous function even if the kinetic pressure drops rapidly at the plasma edge. For the vacuum region there are not moving (or still) charges, and the current density vanishes, then the Grad-

Shafranov equation is reduced to

$$\left( \frac{\partial^2}{\partial R^2} - \frac{1}{R} \frac{\partial}{\partial R} + \frac{\partial^2}{\partial z^2} \right) \psi_v(R, z) = 0, \quad (3.21)$$

And the solution to this equation must match the value of  $\psi$  at the plasma edge, i.e.  $\psi(\Sigma_p) = \psi_v(\Sigma_p)$ . Although the magnetic flux must be continuous it does not need to be smooth, and the poloidal magnetic field may present discontinuities. This is particularly true when the kinetic pressure presents a step to zero at the plasma edge, then we need the more general integral form of the equilibrium condition [Grad and Rubin (1958)], that leads to the continuity of the scalar energy density everywhere

$$\mathcal{E} = p + \frac{B^2}{\mu_0}, \quad (3.22)$$

which in turn requires a discontinuity in  $\vec{B}$  if an abrupt fall in  $p$  occurs at the plasma edge  $\Sigma_p$ . This, in turn requires the existence of a surface current at the plasma edge given by

$$\vec{\sigma}_\Sigma = \mu_0^{-1} \hat{n}_\Sigma \times (\vec{B}_{out} - \vec{B}_{in}), \quad (3.23)$$

where  $\hat{n}_\Sigma$  is the normal to the plasma boundary. In terms of the poloidal magnetic flux, the toroidal component of this equation takes the form

$$\frac{\partial \psi_v}{\partial n_\Sigma} - \frac{\partial \psi}{\partial n_\Sigma} = \sigma_{\Sigma, \phi}, \quad (3.24)$$

so that the surface current accounts for the discontinuity on the magnetic field and must be obtained self-consistently with the boundary of the plasma.

These considerations are usually avoided by requiring the pressure to vanish smoothly at the plasma edge, leading to a simpler set of boundary conditions

$$\psi_{v, \Sigma} = \psi_\Sigma, \quad \frac{\partial \psi_v}{\partial n_\Sigma} = \frac{\partial \psi}{\partial n_\Sigma}. \quad (3.25)$$

where the boundary surface  $\Sigma$  can be established self-consistently by a functional minimization procedure, or can be specified based on experimental diagnostics.

## 3.2 General numerical solution

Formally, the LHS differential operator in (3.19) is linear and it can be inverted by means of the Green's function for a *point-like* source [Arfken et al. (2013)]. In other words, we

can solve

$$\left( \frac{\partial^2}{\partial R^2} - \frac{1}{R} \frac{\partial}{\partial R} + \frac{\partial^2}{\partial z^2} \right) G(R, z; R', z') = -\mu_0 R I \delta(R, z; R', z'), \quad (3.26)$$

where  $I$  is the toroidal current in the source. This problem is equivalent to calculating the poloidal flux created by a circular filament located at  $(R', z')$  in the point  $(R, z)$ . This flux can be found by determining  $RA_\phi$  for the given geometry with elementary operations [Jackson (1999)], and leads to

$$G(R, z; R', z') = \frac{\mu_0 \sqrt{RR'}}{2\pi k} [(2 - k^2)K(k^2) - E(k^2)], \quad (3.27)$$

where  $K$  and  $E$  are complete elliptic integrals of the first and second kind [Arfken et al. (2013)], and we defined the parameter

$$k^2 = \frac{4RR'}{(R + R')^2 + (z - z')^2}. \quad (3.28)$$

Having the Green's function we can determine the poloidal magnetic flux if we know all the sources of magnetic field. This is

$$\psi(R, z) = \sum_{i=1}^{N_f} I_{f,i} G(R, z; R_i, z_i) + \int_{\Omega} j_\phi(R', z') G(R, z, R', z') dR' dz', \quad (3.29)$$

where the first sum runs over a set of filaments that discretize the external poloidal field coils (like those in red in Fig. 3.2), where the filament at  $(R_i, z_i)$  carries a current  $I_{f,i}$ , and  $N_f$  is the total number of filaments. The integral, on the other side, corresponds to the contribution of each plasma element, carrying a current  $j_\phi(R', z') dR' dz'$  yet to determine.

Equation (3.29), however does not determine the poloidal flux  $\psi$  because the toroidal current density depends on the unknown  $\psi(R, z)$  through the arbitrary functions  $p(\psi)$  and  $F(\psi)$ . In other words, we just write down the problem in an integral form. However, this form of the problem suggests the use of the Picard's method in the form

$$\psi^{(n+1)}(R, z) = \sum_{i=1}^{N_f} I_{f,i} G(R, z; R_i, z_i) + \int_{\Omega} j_\phi[R', \psi^{(n)}(R', z')] G(R, z, R', z') dR' dz', \quad (3.30)$$

where  $\psi^{(n)}(R, z)$  is the  $n$ 'th step approximation of the poloidal magnetic flux, which allows to calculate the  $n + 1$ 'th iterate, and clearly requires an initial guess of the poloidal magnetic flux. Under suitable conditions this procedure converges to the desired solution and can be modified to adjust simultaneously the parameters of the previously defined arbitrary functions  $p(\psi, \vec{\alpha}_p)$  and  $F(\psi, \vec{\alpha}_F)$ , to converge to the desired plasma geometry and parameters [Lao et al. (1985)].

### 3.3 Analytical equilibrium solutions

As was shown before, the toroidal current density and toroidal magnetic field can be written in terms of the kinetic pressure  $p(\psi)$  and poloidal current  $F(\psi)$ , which can be considered *arbitrary* functions of the poloidal magnetic flux  $\psi$  that labels each magnetic surface.

$$j_\phi(R, \psi) = Rp'(\psi) + \frac{FF'(\psi)}{\mu_0 R}, \quad (3.31)$$

$$B_\phi(R, \psi) = \frac{F(\psi)}{R}. \quad (3.32)$$

The form of the arbitrary functions  $p(\psi)$  and  $F(\psi)$  defines the equilibrium properties, and, in general, these functions are unknown and must be defined simultaneously and self-consistently with the boundary conditions. Because of this nonlinear coupling, the problem must be solved numerically, even if we are able to find a family of analytical solutions for the Grad-Shafranov equation.

For the analytical and numerical treatment of the equilibrium problem it is convenient to write all the physical quantities in terms of dimensionless functions

$$\psi = \psi_a \bar{\psi}, \quad (3.33)$$

$$p(\psi) = p_a \bar{p}(\bar{\psi}), \quad (3.34)$$

$$F(\psi) = R_0 B_0 \bar{F}(\bar{\psi}), \quad (3.35)$$

$$R = R_0 x, \quad (3.36)$$

$$z = R_0 y, \quad (3.37)$$

$$j_\phi(R, \psi) = \frac{B_0}{\mu_0 R_0} \bar{j}_\phi(x, \bar{\psi}), \quad (3.38)$$

where, the quantities with sub-index 0 are measured at the plasma center and those with  $a$  are measured at the magnetic axis, and we have adopted the following convention for the poloidal magnetic flux:

$$\psi > 0 : \text{inside the separatrix}, \quad (3.39)$$

$$\psi < 0 : \text{outside the separatrix}. \quad (3.40)$$

Which means that the dimensionless flux and pressure will be always between 0 and 1 inside the plasma. This convention comes from setting the arbitrary zero of the poloidal flux at the magnetic separatrix and taking the poloidal magnetic field as upwards in the mid-plane region between the HFS wall and the magnetic axis. This means that the toroidal current is in the positive toroidal direction.

Now, let us condense some relevant information of the discharge in the parameters

$$\bar{\beta} = \frac{\mu_0 p_a}{B_0^2}, \quad (3.41)$$

$$\varphi = \frac{R_0^2 B_0}{\psi_a}. \quad (3.42)$$

where  $\bar{\beta}$  was defined in analogy to the plasma beta [Freidberg (2004)], and measures the ratio between kinetic and magnetic energy along the magnetic axis, while  $\varphi$  is proportional to the ratio of toroidal and poloidal magnetic fluxes, which is intimately related to the safety factor. In the particular case of DIII-D the toroidal magnetic field is applied opposite to the current density, so  $B_0$  is a negative number and so is  $\varphi$ . This causes the dimensionless current density to be negative, which will be the signature of the direction of the applied toroidal field.

With this replacements the Grad-Shafranov equation takes the dimensionless form

$$\left( \frac{\partial^2 \bar{\psi}}{\partial x^2} - \frac{1}{x} \frac{\partial \bar{\psi}}{\partial x} + \frac{\partial^2 \bar{\psi}}{\partial y^2} \right) = -\varphi^2 (\bar{\beta} x^2 \bar{p}' + \bar{F} \bar{F}'), \quad (3.43)$$

and the dimensionless current density becomes

$$\bar{j}_\phi = \frac{\varphi}{x} (\bar{\beta} x^2 \bar{p}' + \bar{F} \bar{F}'). \quad (3.44)$$

### 3.3.1 Arbitrary functions

To obtain analytical solutions of the G-S equation we can choose the arbitrary functions structure that leads to a linear partial differential equation (PDE). This will lead to a continuous basis to expand the poloidal magnetic flux inside the plasma. This choice of the arbitrary functions, while restricts the type of equilibria we are able to describe, allows us to develop fast equilibrium calculators based on suitable boundary conditions.

In the following, we choose

$$\bar{p}(\bar{\psi}) = \bar{\psi}, \quad (3.45)$$

$$\bar{F}^2(\bar{\psi}) = (a\bar{\psi}^2 - 2c\bar{\psi} + \varphi^2)/\varphi^2. \quad (3.46)$$

This corresponds to the so called dissimilar sources introduced in [McCarthy (1999)]. In [Ciro and Caldas (2014)] we studied this type of solutions and determined some global properties of the current density in relation to the parameters space. We also identified the relation between the magnetic axis safety factor and the eigenvalue of the associated homogeneous problem.

In the following we revisit some of these calculations introducing new physical restrictions to the parameters and important improvements to the numerical optimization methods. This allowed us to search for solutions that match both the magnetic axis safety factor and the total plasma current, which was not included in the numerical optimization of the previous research paper [Ciro and Caldas (2014)]. Requiring  $F^2$  to be less than one (diamagnetic plasma) we obtain from (3.46) a couple of restrictions for the parameters defining the dimensionless poloidal current

$$c > 0, 2c > a. \quad (3.47)$$

We can also ask for the diamagnetic effect to be small, for instance, if we require  $4/5 < \bar{F} < 1$  we obtain a more physical restriction

$$a > 2c - (3\varphi/5)^2, c > 0. \quad (3.48)$$

These limits are useful to control the evolution of the optimization methods, avoiding the convergence to nonphysical solutions where the poloidal current is not well defined. Notice that  $a$  can be both positive or negative, and this will change the nature of the solutions. Using these arbitrary functions the dimensionless G-S equation becomes

$$\left( \frac{\partial^2 \bar{\psi}}{\partial x^2} - \frac{1}{x} \frac{\partial \bar{\psi}}{\partial x} + \frac{\partial^2 \bar{\psi}}{\partial y^2} \right) = -a\bar{\psi} - bx^2 + c. \quad (3.49)$$

where  $b = \bar{\beta}\varphi^2$  is a positive number. A particular solution  $\psi_p$  is required to account for the inhomogeneous term [Arfken et al. (2013)]. In the following we use

$$\psi_p = -\frac{b}{a}x^2 + \frac{c}{a}, \quad (3.50)$$

That leads to an eigenvalue problem for the homogeneous function

$$\left( \frac{\partial^2 \psi_h}{\partial x^2} - \frac{1}{x} \frac{\partial \psi_h}{\partial x} + \frac{\partial^2 \psi_h}{\partial y^2} \right) = -a\psi_h. \quad (3.51)$$

The form of the solutions will depend on the sign of  $a$  and we need to analyze them

separately. For  $a > 0$  and  $s^2 = a$  the solutions to the homogeneous problem becomes

$$\psi_h(x, y) = \begin{cases} x[I_1, K_1(\alpha x)][\sin, \cos(\gamma y)], & \gamma^2 = \alpha^2 + s^2 \\ [1, x^2][\sin, \cos(sy)], & \alpha = 0 \\ x[J_1, Y_1(\alpha x)][\sin, \cos(\gamma y)], & \gamma^2 = s^2 - \alpha^2 \\ x[J_1, Y_1(sx)][1, y], & \gamma = 0 \\ x[J_1, Y_1(\alpha x)][\sinh, \cosh(\gamma y)], & \gamma^2 = \alpha^2 - s^2. \end{cases} \quad (3.52)$$

Another possible solution results from assuming spherical symmetry, which does not involve separation of variables and results in

$$\psi_{sph}(x, y) = [\sin, \cos(s\sqrt{x^2 + y^2})]. \quad (3.53)$$

Clearly, this kind of solution is not physical on its own because defines simply connected magnetic surfaces where the MHD equilibrium is forbidden. However it can be used in combination with other functions, and its presence in the expansion is useful to shape the magnetic surfaces in small aspect ratio situations.

Following the same procedure for  $a < 0$  and  $s^2 = -a$ , the solutions take the form

$$\psi_h(x, y) = \begin{cases} x[J_1, Y_1(\alpha x)][\sinh, \cosh(\gamma y)], & \gamma^2 = \alpha^2 + s^2 \\ [1, x^2][\sinh, \cosh(sy)], & \alpha = 0 \\ x[I_1, K_1(\alpha x)][\sinh, \cosh(\gamma y)], & \gamma^2 = s^2 - \alpha^2 \\ x[I_1, K_1(sx)][1, y], & \gamma = 0 \\ x[I_1, K_1(\alpha x)][\sin, \cos(\gamma y)], & \gamma^2 = \alpha^2 - s^2, \\ [\sinh, \cosh(s\sqrt{x^2 + y^2})]. & \text{spherical solution} \end{cases} \quad (3.54)$$

These continuous families of solutions must take the same asymptotic form when approaching the extremes of the parameters branches.

In Fig.3.3 we summarize all the possible solutions from separation of variables in the parameters space for the different choices of the sign of  $a$ . The asymptotic values of the solutions are depicted at the intersection of the consecutive branches of the solutions. To summarize, the complete poloidal magnetic flux can be written in the form

$$\bar{\psi}(x, y) = \psi_p(x, y) + \psi_h(x, y), \quad (3.55)$$

$$\bar{\psi}(x, y) = \frac{c}{a} - \frac{b}{a}x^2 + \frac{d}{a}\psi_{sph}(x, y) + \sum_{i=1}^n c_i x B(\alpha_i x) H(\gamma_i y), \quad (3.56)$$

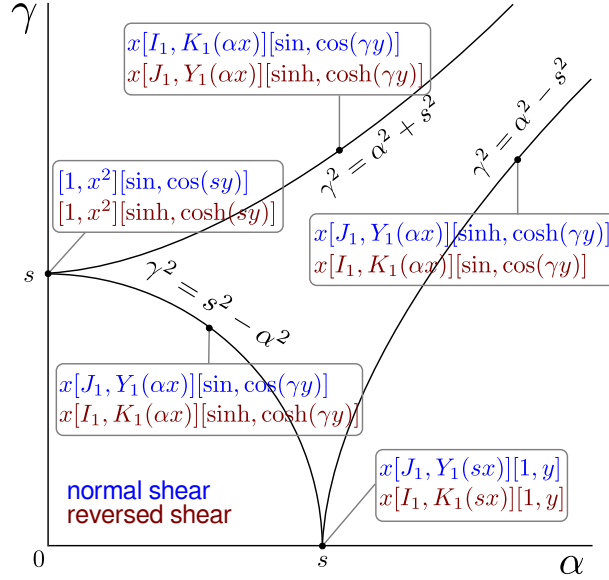


Figure 3.3: Summary of the solutions to the homogeneous problem for different choices of  $a$  and different regions of the parameters space.

where the Bessel and harmonic functions depend on the sign of  $a$  and the number of elements in the expansion is more or less arbitrary. For a given boundary value problem we must optimize the expansion coefficients  $c_i$  and the nonlinear parameters  $\alpha_i$  to match a given set of boundary conditions. Once we have the poloidal flux, we can write back the dimensionless current density as

$$\bar{j}_\phi = \frac{1}{\varphi x} (bx^2 + a\bar{\psi} - c). \quad (3.57)$$

It is clear from the previous expression that the toroidal current density can not vanish simultaneously at the plasma edge in the low and high field sides where  $x = 1 \pm \epsilon$ . This is a limitation of the model and can not be avoided by a suitable choice of parameters. Let us define the current density in low-field side and the high-field side separatrix at the mid-plane as

$$\bar{j}_{LFS} = \frac{b(1 + \epsilon)}{\varphi} - \frac{c}{\varphi(1 + \epsilon)}, \quad (3.58)$$

$$\bar{j}_{HFS} = \frac{b(1 - \epsilon)}{\varphi} - \frac{c}{\varphi(1 - \epsilon)}. \quad (3.59)$$

In particular, we can assume that the current density vanishes in the HFS and is positive in the LFS, but this may cause an overestimation of the plasma current, since in a real situation the current must vanish in both sides simultaneously. Because of this we admit a moderate current inversion in the high-field side, so that both the HFS and LFS current

densities are closer to zero. Then we can write

$$\bar{j}_{HFS} = -\eta\bar{j}_{LFS}, \quad (3.60)$$

where  $0 < \eta < 1$  is an adjustable parameter that will be kept fixed during the optimization procedure. Replacing (3.58, 3.59) in (3.60) we obtain a relation between  $b$  and  $c$ .

$$c = \frac{(1 - \epsilon) + \eta(1 + \epsilon)}{(1 + \epsilon) + \eta(1 - \epsilon)}(1 - \epsilon^2)b = hb \quad (3.61)$$

where  $h$  is related to the geometric parameters of the discharge and the ratio  $\eta$ . Also, it can be shown that the difference between the LFS and HFS current densities has the form

$$\bar{j}_{LFS} - \bar{j}_{HFS} = 2\varphi\epsilon\bar{\beta}, \quad (3.62)$$

so that, for this choice of the arbitrary functions, the increase of  $\bar{\beta}$  or the kinetic pressure leads to a larger difference between the high-field side and low field side current densities. Using the linear relation between  $b$  and  $c$  the toroidal current density becomes

$$\bar{j}_\phi = \frac{1}{\varphi x}(bx^2 - hb + a\bar{\psi}). \quad (3.63)$$

### 3.3.2 Geometrical parameters of the equilibrium

As mentioned before, the boundary of the plasma can be established self-consistently by the numerical optimization procedure, or can be prescribed based in experimental information, like the hot spots in the tokamak chamber located near the intersection of the magnetic separatrix and the vacuum chamber, and the temperature and density profiles measured from Thomson scattering. In the last case the numerical procedure becomes less intensive and is good for quick equilibrium reconstructions. To model the plasma edge we can use a minimalist parametric equation containing the most relevant geometry

$$x_b(\theta) = 1 + \epsilon \cos(\theta + \alpha \sin \theta), \quad (3.64)$$

$$y_b(\theta) = \epsilon \kappa \sin \theta, \quad (3.65)$$

$$\delta = \sin \alpha. \quad (3.66)$$

This describes a D-shape with triangularity  $\delta$ , elongation  $\kappa$  and minor radius  $\epsilon$ . In the case of a single or double null configuration we can trace straight lines that meet at the X-point at a distance  $\eta\epsilon$  from the center with a desired angle  $\xi$  (see Fig. 3.4). For given values of  $\xi$  and  $\eta$ , the positions of the X-point  $p_3$ , and the tangency points  $p_1, p_2$  are

uniquely determined and can be found by solving numerically an implicit equation.

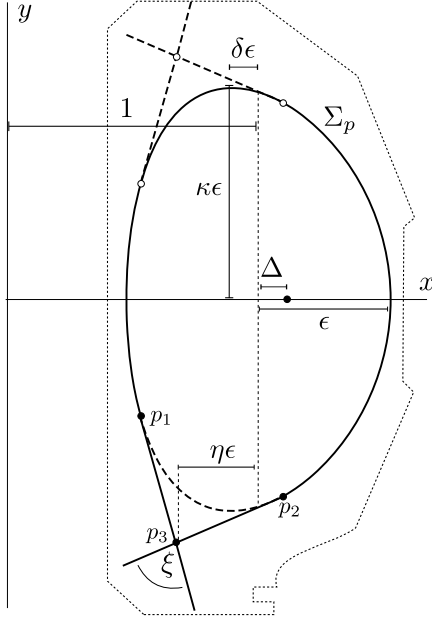


Figure 3.4: The plasma edge is modeled by merging a D-shape with specified elongation  $\kappa$ , and triangularity  $\delta$  with two straight tangents starting at  $p_1$ ,  $p_2$  meeting at the X-point  $p_3$ . The center of the column is at  $x = 1$  and the magnetic axis is displaced by  $\Delta$ .

Once we obtain the experimental information about the plasma shape and the location of the magnetic axis we can set the dimensionless poloidal flux at the prescribed boundary  $\bar{\psi}(\Sigma_p) = 0$ , and  $\bar{\psi}(1 + \Delta, 0) = 1$  at the magnetic axis.

### 3.3.3 Control functions

To control the iterative procedure that solves the G-S equation we need to define a set of target functions depending on a set of parameters that will be optimized by an iterative numerical procedure. As mentioned before, the first requirement is that the poloidal magnetic flux vanishes along the predefined plasma edge  $\Sigma_p$ . At the same time we need to optimize the location of the magnetic axis with an specified safety factor, that can be measured with Motional Stark Effect (MSE) [Rice (1996)] and a given toroidal current obtained from the poloidal magnetic field probes.

At the magnetic axis, the safety factor can be obtained by [Bateman (1987)]

$$q_a = \frac{\bar{B}_\phi}{|\partial_x(x\bar{B}_y)\partial_y(x\bar{B}_x)|^{1/2}}. \quad (3.67)$$

In terms of our dimensionless variables this becomes

$$q_a = \frac{\bar{B}_{a,\phi}}{x_a \bar{j}_{a,\phi}} (\zeta + \zeta^{-1}). \quad (3.68)$$

where the subscript  $a$  indicates evaluation at the magnetic axis and the quantity  $\zeta = \lim_{\Delta x \rightarrow 0} \Delta y / \Delta x$  measures the elongation of the innermost magnetic surface and can be

calculated using the poloidal magnetic flux as

$$\zeta = \sqrt{\frac{\partial_{xx}\bar{\psi}}{\partial_{yy}\bar{\psi}}}, \quad (3.69)$$

where the derivatives are also evaluated at the magnetic axis. Using the arbitrary functions defined in our model we have

$$q_a = \text{sgn}(\varphi) \frac{\sqrt{a - 2hb + \varphi^2}}{x_a(bx_a^2 + a - hb)} (\zeta + \zeta^{-1}). \quad (3.70)$$

We can find the safety factor exactly in terms of the parameters of the particular solution and the eigenvalue of the system. This is an example of a local parameter, but more general restrictions often involve global quantities that depend on surface or line integrals.

The plasma current fall in this category. Using the arbitrary functions we have

$$I_p = \frac{R_0 B_0}{\mu_0} \int_{\Omega} \frac{1}{\varphi x} (bx^2 + a\psi - hb) dx dy, \quad (3.71)$$

where the surface integral is calculated on the cross section of the plasma  $\Omega$  bounded by  $\Sigma_p$ . In dimensionless form, this current can be split in three different contributions.

$$\bar{I} = \frac{b}{\varphi} \left[ \int_{\Omega} x dx dy - h \int_{\Omega} \frac{dx dy}{x} \right] + \frac{a}{\varphi} \int_{\Omega} \frac{\psi(x, y)}{x} dx dy. \quad (3.72)$$

The first two integrals are constants depending on the definition of the cross-section, but the last one depends on the poloidal flux, meaning that it changes as we optimize the problem parameters. In the following we discuss the numerical optimization method that allows us to search for solutions matching the desired values of the safety factor and plasma current, while satisfying the geometrical constrains imposed by the plasma edge and the magnetic axis.

### 3.4 Semi-analytical solution

Using the analytical solutions resulting from the dissimilar sources approach we can model the poloidal magnetic flux as a linear superposition of a discrete set of functions depending parametrically to the eigenvalue of the system and one separation constant. Then, we need to optimize the parameters of this superposition to reproduce the plasma shape, current and safety factor. Such optimization can be achieved by a functional minimization algorithm, like the one presented in Appendix B.1.

The form of the algorithm presented in the Appendix is useful for fitting the poloidal

flux function when we prescribe the plasma edge and the magnetic axis. Since we are working with dimensionless variables, the desired values for the poloidal flux are *one* at the magnetic axis and *zero* at the separatrix. However, we need to modify the method to optimize the magnetic axis safety factor and the toroidal current density as well. To do this we can imagine that the points  $x_i$  can be both positions and labels for different kinds of functions and  $y_i$  are the desired values of the flux in those points or the functions labeled by  $x_i$ . For instance, we can define the function to be optimized as

$$\vec{f}(\vec{k}) = \{\bar{\psi}_1, \bar{\psi}_2, \dots, \bar{\psi}_{n_p}, \bar{I}_p(\vec{k}), q_a(\vec{k})\}, \quad (3.73)$$

where  $\bar{\psi}_i = \bar{\psi}(\vec{k}, x_i, y_i)$  is the value of the poloidal flux model at the points  $\{x_i, y_i\}$  and  $n_p$  is the number of control points that may include the magnetic axis and the lower portion of the separatrix.  $\bar{I}_p(\vec{k})$  is the modeled plasma current and  $q_a(\vec{k})$  is the modeled magnetic axis safety factor. Since the nature of these quantities is different and there are more elements related to the geometry of the system we need to modify the error functional to weight this quantities

$$\mathcal{E}(\vec{k}) = \sum_{i=1}^m w_i (y_i - f_i(\vec{k}))^2 \quad (3.74)$$

where the weights  $w_i$  are used to scale the quantities so that they contribute evenly to the error. The new linear problem to find the variation takes the form

$$\left( w_i \frac{\partial f_i}{\partial k_j} \frac{\partial f_i}{\partial k_n} - \lambda \delta_{j,n} w_i \frac{\partial f_i}{\partial k_j} \frac{\partial f_i}{\partial k_n} \right) \delta k_n = w_i \frac{\partial f_i}{\partial k_j} (y_i - f_i), \forall j \quad (3.75)$$

where three repeated indexes indicate summation. A similar procedure can be employed if we want to give more weight to some spatial locations that can be narrowed experimentally, like the separatrix saddle or the magnetic axis.

### 3.4.1 Numerical implementation

First, we need to give a global structure to the basis functions. For this we define  $f[i, s, a, x, y]$ , where  $i$  is an index that identifies the type of solution,  $s$  is the square-root of the eigenvalue,  $a$  plays the role of  $\alpha$  in the solutions (3.54, 3.52), and  $\{x, y\}$  are the dimensionless cylindrical coordinates  $\{R/R_0, z/z_0\}$ . Numerically, we need to state explicitly which numbers are positive or negative (when known) to prevent the system to converge to a nonphysical solution where the poloidal current is imaginary and the safety factor is not defined. To do this we relate our parameters to positive defined quantities with an explicit sign.

$$\{c_1^2, c_2^2, -c_3^2\} = \{a, b, \varphi\} \quad (3.76)$$

doing this, the safety factor becomes

$$q_a = \frac{\sqrt{c_1^2 - 2hc_2^2 + c_3^4}}{x_a(c_2^2 x_a^2 + c_1^2 - hc_2^2)} (\zeta + \zeta^{-1}), \quad (3.77)$$

and the plasma toroidal current takes the form

$$\bar{I} = \frac{c_2^2}{c_3^2} \left[ h \int \frac{dx dy}{x} - \int x dx dy \right] - \frac{c_1^2}{c_3^2} \int \frac{\psi(x, y)}{x} dx dy. \quad (3.78)$$

Provided these definitions the derivatives of the control functions will vanish when the redefined parameters go to zero. This suppresses the gradients towards negative values and the optimization process won't evolve to nonphysical solutions where poloidal current and magnetic axis safety factor are not defined. This new feature is an improvement to the method presented in [Ciro and Caldas (2014)] where the numerical method could eventually evolve to such negative values, giving complex solutions that reduce the error but do not have necessarily a physical meaning.

In terms of the redefined parameters the poloidal magnetic flux takes the form

$$\bar{\psi}(c_j, h_j, a_j, x, y) = (h - x^2) \frac{c_2^2}{c_1^2} + \sum_{i=1}^{n_f} d_i x f[n_i, c_1, a_i, x, y]. \quad (3.79)$$

where  $c_1 = s$  is the eigenvalue of the problem,  $n_f$  is the number of basis functions used in the expansion, and  $n_i$  is an index that identifies internally the basis elements. We need to combine all the optimization parameters in a single vector to address them simultaneously.

$$\vec{k} = \{ \{d_i\}, \{a_i\}, \{c_i\} \}. \quad (3.80)$$

Also, the model function  $\vec{f}(\vec{k})$  that combines the poloidal flux at the control points  $\bar{\psi}(\vec{r}_i)$  with the safety factor  $q_a$  and the plasma current  $\bar{I}$  becomes

$$f_j(\vec{k}) = (h - x^2) \frac{k_{2n_f+2}^2}{k_{2n_f+1}^2} + \sum_{i=1}^{n_f} k_i f[n_i, k_{2n_f+1}, k_{n_f+i}, x_j, y_j], \text{ for } j < n_p \quad (3.81)$$

$$f_{n_p+1}(\vec{k}) = \frac{\sqrt{k_{2n_f+1}^2 - 2hk_{2n_f+2}^2 + c_{2n_f+3}^4}}{x_a(c_{2n_f+2}^2 x_a^2 + k_{2n_f+1}^2 - hk_{2n_f+2}^2)} (\kappa + \kappa^{-1}), \quad (3.82)$$

$$f_{n_p+2}(\vec{k}) = \frac{k_{2n_f+2}^2}{k_{2n_f+3}^2} \left[ h \int \frac{dx dy}{x} - \int x dx dy \right] - \frac{k_{2n_f+1}^2}{k_{2n_f+3}^2} \int \frac{\psi(x, y)}{x} dx dy. \quad (3.83)$$

with  $n_p$  the number of control points distributed along the magnetic separatrix, the magnetic axis and possibly the divertor legs. Clearly, the corresponding target values  $\vec{y}$  have

the values

$$y_j = \tilde{\psi}_j, \text{ for } j < n_p, \quad (3.84)$$

$$y_{n_p+1} = \tilde{q}_a, \quad (3.85)$$

$$y_{n_p+2} = \tilde{I}_p. \quad (3.86)$$

The dimensionless current  $\tilde{I}_p$  and magnetic axis safety factor  $\tilde{q}_a$  are the experimental values that we want to adjust with our model function.

An important issue that must be taken into account is that the function that calculates the magnetic axis safety factor requires the existence of an elliptic point inside the calculation domain, then  $f_{n_p+1}$  may be not defined in the first iterate where the initial values of  $\vec{k}$  are set more or less arbitrarily. Also, during the optimization process the obtained variation  $\delta\vec{k}$  may lead to configurations without magnetic axis. To handle this, the last two elements of the model function are only optimized when there is an elliptic point located inside the computational box [Jardin (2010)], otherwise the method only optimizes the parameters of the poloidal magnetic flux.

In the first cycle, the whole parameter vector  $\vec{k}$  is optimized so that the poloidal flux value at the prescribed separatrix is *zero*, and *one* at the prescribed magnetic axis. After this step is carried the algorithm searches for a point inside the separatrix where the poloidal field vanishes. If found the system checks if it is a magnetic axis is a saddle point using

$$\partial_{x,y}^2 \bar{\psi} < \partial_{x,x} \bar{\psi} \times \partial_{y,y} \bar{\psi}. \quad (3.87)$$

If this is true the elongation of the innermost magnetic surface is calculated and the method includes the magnetic axis safety factor and the toroidal current in the optimization calculations.

During the optimization there is a competition between the geometric and the physical quantities and the error can momentarily grow when the magnetic axis is created or destroyed, but in the overall picture the error is reduced by the optimization and its saturation value is a property of the choice of the basis functions and the initial condition of the optimization algorithm.

### 3.4.2 Safety factor profile

In general, the safety factor of a magnetic surface is the constant ratio between the toroidal  $\Delta\phi$ , and poloidal  $\Delta\vartheta$ , angular displacements of the magnetic field lines. However, the poloidal angle does not change uniformly when depicted in the Cartesian space, so, to calculate the safety factor profile in a shaped discharge we need to follow the magnetic

field lines until they perform a complete poloidal cycle, which guarantees  $\Delta\vartheta = 2\pi$ , then measure the total toroidal angle subtended by the line. The safety factor at some particular surface becomes

$$q(\bar{\psi}) = \frac{\Delta\phi}{2\pi}, \quad (3.88)$$

To follow the magnetic field line for one poloidal cycle we need to define its differential equations and integrate numerically. In Appendix B.2 we present an effective integration method and the magnetic field lines can be obtained by putting (2.11) in cylindrical coordinates. The dimensionless poloidal magnetic field is  $\vec{B}_p = \nabla\psi \times \nabla\phi/B_0$ , then

$$\vec{B}_p = \frac{\nabla\bar{\psi} \times \hat{\phi}}{\varphi x}. \quad (3.89)$$

On the other side, the toroidal component of the magnetic field satisfies

$$B_\phi = \frac{\bar{F}(\bar{\psi})}{x} = \frac{\sqrt{a\bar{\psi}^2 - 2hb\bar{\psi} + \varphi^2}}{\varphi x}. \quad (3.90)$$

In dimensionless coordinates a line element parallel to the magnetic field satisfies  $d\vec{l} = \alpha\vec{B}$ , where  $\alpha$  is some proportionality factor. This vector equation leads to a system of coupled differential equations governing the field line in cylindrical coordinates, with the toroidal angle  $\phi$  as the independent coordinate

$$\frac{dx}{d\phi} = x \frac{B_x}{B_\phi} = -\frac{x\partial_y\bar{\psi}}{\sqrt{a\bar{\psi}^2 - 2hb\bar{\psi} + \varphi^2}}, \quad (3.91)$$

$$\frac{dy}{d\phi} = x \frac{B_y}{B_\phi} = \frac{x\partial_x\bar{\psi}}{\sqrt{a\bar{\psi}^2 - 2hb\bar{\psi} + \varphi^2}}. \quad (3.92)$$

Solving numerically this set of equations for a sequence of magnetic surfaces we can interpolate the safety factor as a function of the poloidal magnetic flux.

### 3.5 Comparison with EFIT

To finalize this chapter we want to show the results of the implementation of our equilibrium reconstruction procedure for a real discharge of the DIII-D tokamak (General Atomics, San Diego CA), and compare with the equilibrium reconstruction obtained with the EFIT equilibrium reconstruction code [Lao et al. (1985)]. To solve the Grad-Shafranov equation using the arbitrary functions presented above we have implemented the Levenberg-Marquardt algorithm in *Mathematica* language to use both its numerical and symbolic capabilities. The routine was named DISFUNSOL (acronym for DISSimilar

FUNCTIONS SOLver). The physical and geometrical parameters correspond to the shot #147170 of DIII-D at the time 2.375s. The equilibrium information of the discharge was loaded from a G-file generated by the EFIT MHD reconstruction code using the routine `g_file_loader` written for this purpose.

The parameters of the discharge are the following

$I_p(MA)$	$q_a$	$B_0(T)$	$R_0(m)$	$\epsilon$	$\delta$	$\kappa$
1.61	0.85	-1.95	1.7	0.35	0.3	1.57

This correspond to a single null discharge. The coordinates of the magnetic axis and the X-point are

$R_a(m)$	$Z_a(m)$	$R_s(m)$	$Z_s(m)$
1.76	-0.01	1.3	-1.23

With this information we can calculate the corresponding dimensionless quantities required to run our Grad-Shafranov solver. For the poloidal flux expansion we use a predominant set of even functions in  $y$  and the structure of the solutions is chosen so that we include elements in all the branches of the continuous family of solutions. The expansion used has the form

$$\begin{aligned}
\bar{\psi}(x, y) = & (h - x^2)d_1xI_1(k_1x) \cos(\sqrt{k_1^2 + s^2}y) + d_2xK_1(k_2x) \cos(\sqrt{k_2^2 + s^2}y) + d_3 \cos(sy) \\
& + d_4x^2 \cos(sy) + d_5xJ_1(k_5x) \cos(\sqrt{s^2 - k_5^2}y) + d_6xY_1(k_6x) \cos(\sqrt{s^2 - k_6^2}y) + d_7xJ_1(sx) \\
& + d_8xY_1(sx) + d_9xJ_1(k_9x) \cosh(\sqrt{k_9^2 - s^2}y) + d_{10}xY_1(k_{10}x) \cosh(\sqrt{k_{10}^2 - s^2}y) \\
& + d_{11} \sin(s\sqrt{x^2 + y^2}) + d_{12} \cos(s\sqrt{x^2 + y^2}) + d_{13}xJ_1(k_{13} * x) \sin(\sqrt{s^2 - k_{13}^2}y) \\
& + d_{14}xY_1(k_{14}x) \sin(\sqrt{s^2 - k_{14}^2}y) + d_{15}xyJ_1(sx) + d_{16}xyY_1(sx).
\end{aligned} \tag{3.93}$$

As explained before, the vector of parameters includes the expansion coefficients  $d_i \equiv k_{n_f+i}$ , the parameters multiplying the coordinates in the arguments  $k_i$ , the eigenvalue of the homogeneous problem  $s \equiv k_{2n_f+1}$  and the parameters appearing in the safety factor and total current  $\{k_{2n_f+2}, k_{2n_f+3}\}$ .

In Fig. 3.5 we show the evolution of the parameters as we iterate the Levenberg-Marquardt algorithm. The dashed line indicates the iterate after which all the parameters become almost stationary. This indicates that the system reaches its optimum configuration and the error its minimum value. This is more clear in Fig. 3.6 where the global error  $\epsilon(\vec{k})$  defined in (B.1) drops by two orders of magnitude between iterates 26 and 28 and then becomes almost stationary at about  $5 \times 10^{-6}$ .

Once we have an optimized set of parameters we may proceed to calculate the equilibrium profiles and figures of merit. Since we have optimized using the objective values

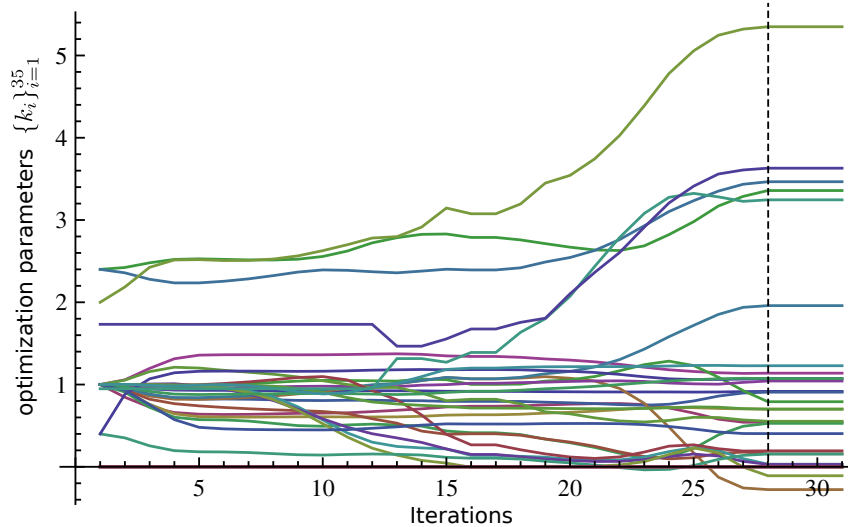


Figure 3.5: Evolution of the optimization parameters by the Levenberg-Marquardt algorithm. The dashed line marks the iterate for which the method converges.

of EFIT we can compare directly with this equilibrium. We start checking if the magnetic surfaces have the desired shape and topology. In Fig. 3.7 we show the contours of the poloidal magnetic flux obtained by the EFIT code and the routine DISFUNSOL. In both cases the contours are equally spaced in the poloidal flux value, then, the magnetic flux grows more rapidly near the edge in DISFUNSOL and becomes more flat in the central region. This will have consequences in the safety factor profile and the magnetic shear. Also, there are some differences in the shape of the separatrix where the DISFUNSOL reconstruction depicts a wider X-point located at larger distance from the divertor plates. This, however, can be corrected in the future by introducing the location of the experimental strike points in the set of control points with a larger weight than the others.

Before introducing the equilibrium profiles, a word of caution about the contours outside the separatrix is needed. In its actual form DISFUNSOL only solves the poloidal magnetic flux inside the plasma and does not use the real position of the poloidal field coils outside the chamber. This means that the depicted contours outside the separatrix do not correspond to a vacuum field and are presented only to illustrate the required magnetic topology outside the plasma. To calculate the actual vacuum field we need to use the *virtual casing principle* [Shafranov and Zakharov (1972)] to tune the currents in the poloidal field coils and calculate the vacuum field contribution from the plasma. This calculation will be included in a future version of DISFUNSOL. The interesting thing about the presented contours outside the separatrix is that the magnetic topology presents the required features of the vacuum field in EFIT, in other words the fictitious current density outside the separatrix is accumulating in the same spots where the poloidal field coils of

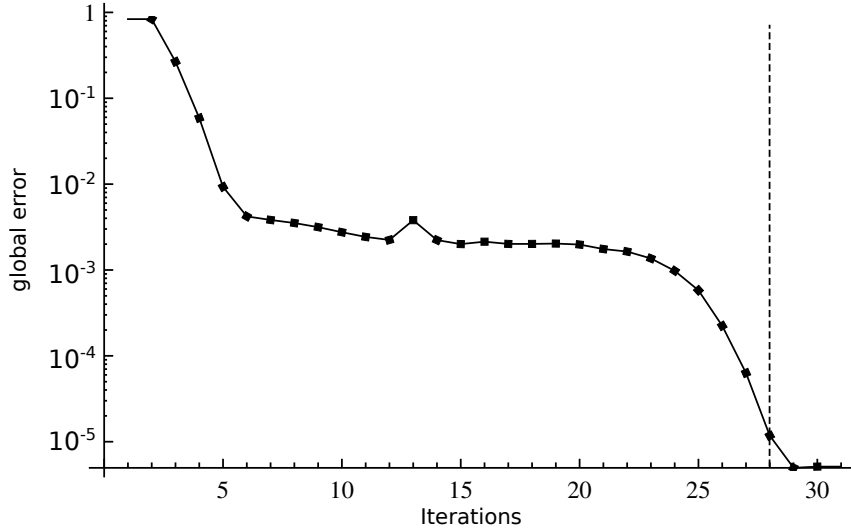


Figure 3.6: Evolution of the global error during the DISFUNSOL optimization. During  $\sim 20$  iterates the error changes little, while the parameters reorder from the initial configuration. Then convergence becomes fast and the error drops to  $\lesssim 10^{-5}$ .

DIII-D are positioned.

Now that we have the poloidal magnetic flux inside the plasma the calculation of the equilibrium profiles is straightforward, except for the safety factor that involves following the field lines for one poloidal cycle.

As a consequence of the different packing of the magnetic surfaces, the safety factor of DISFUNSOL grows slower from the magnetic axis to the edge. This can cause important differences in stability because of the shear differences respect to EFIT. Also, the current density profiles peak at different locations indicating a larger  $\beta$  in the DISFUNSOL prediction. To check this we calculate the toroidal and poloidal beta Freidberg (2004) given by

$$\beta_t = \frac{2\mu_0 \langle p \rangle}{B_0^2}, \quad (3.94)$$

$$\beta_p = 4\pi^2 a^2 (1 - \kappa^2) \frac{\langle p \rangle}{\mu_0 I^2}, \quad (3.95)$$

where  $a$  is the minor radius at the mid-plane,  $\kappa$  is the elongation of the plasma column and  $I$  is the plasma current. In the following table we collect the figures of merit obtained from EFIT and DISFUNSOL.

Solver / fig. merit	$\beta_t$	$\beta_p$	$\beta$	$I_p$	$\epsilon$	$q_a$
EFIT	1.52%	34.8%	1.46%	1.61 MA	0.35	0.85
DISFUNSOL	5.02%	50%	5.59%	1.58 MA	0.348	0.848

All the parameters involved in the optimization process converged to the desired values, i.e. the magnetic axis safety factor  $q_a$ , the plasma current  $I_p$  and the geometrical features

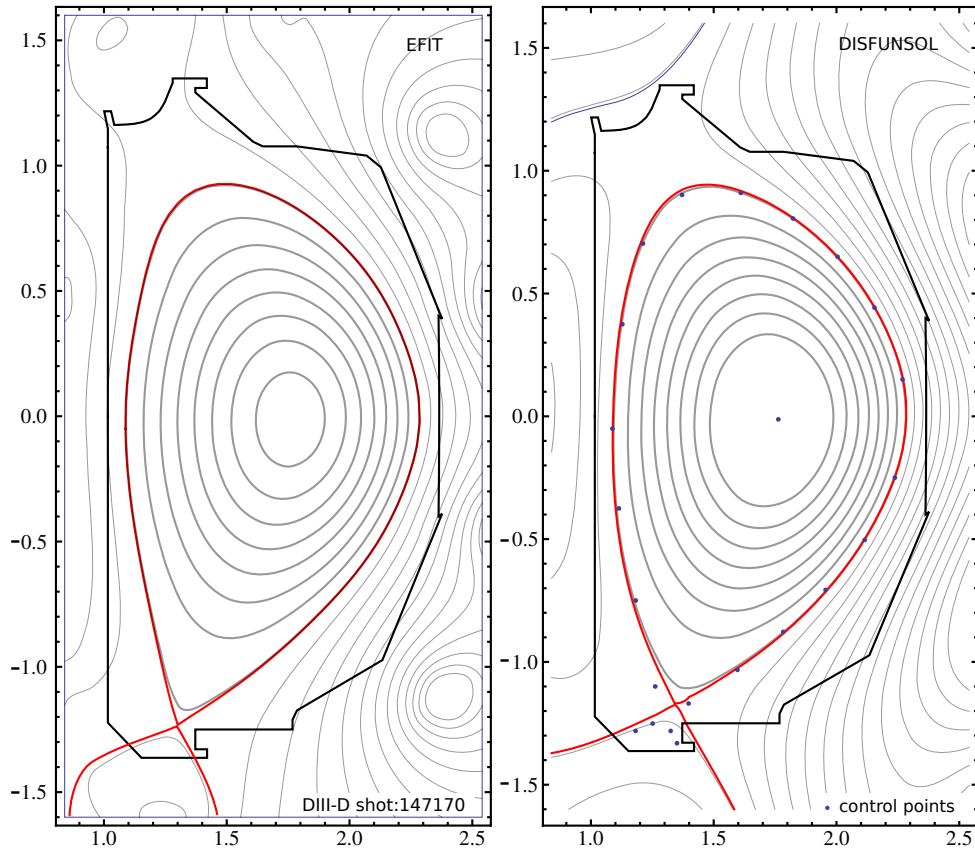


Figure 3.7: Poloidal magnetic flux contours from EFIT and DISFUNSOL for discharge #147170 at  $t = 2.375s$ .

of the discharge. However, the beta values are very different from those of EFIT and must be introduced in the optimization process in a similar way to the plasma current which is an integral control function. Another possibility is setting the value of the kinetic pressure at the magnetic axis, which can be obtained experimentally from density and temperature measurements. Numerically, this sets an explicit relation between  $b$  and  $\varphi$  that restricts further the evolution to the desired solution. Now that we have developed the theoretical basis for accounting for this type of control functions in the optimization process it will be relatively straightforward to introduce these new constrains in future versions of DISFUNSOL.

In its current form DISFUNSOL allows us to optimize simultaneously global quantities like the plasma current and local quantities like the magnetic axis safety factor, and the adjustments for including the kinetic pressure in the calculations are straightforward from this point. The obtained solutions present the desired magnetic topology and realistic equilibrium profiles. Also, the execution of the code demands little computational resources and normally converges in a few tens of iterates taking about 5 min. to run in a single core (1.60GHz Proc., 5.7 Gb RAM).

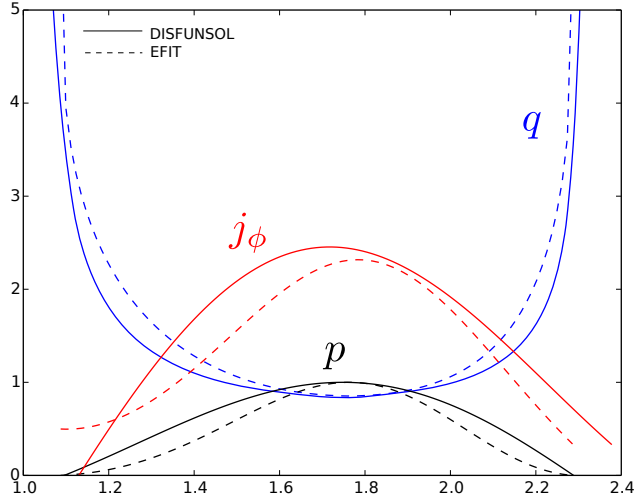


Figure 3.8: The equilibrium profiles from EFIT and DISFUNSOL for discharge #147170 at  $t = 2.375s$ . The current density is measured in units of  $B_0/\mu_0 R_0$  and the kinetic pressure is normalized by its value at the magnetic axis.

### 3.6 Chapter conclusions

The analytical treatment of the Grad-Shafranov equation provides a relevant insight on the relation of the parameters that characterize the plasma and the eigenvalue of the associated linear problems. However, the fact that the plasma edge does not carry any special symmetry compel us to use numerical methods to adjust the linear and non-linear parameters of the poloidal flux expansion, even when a complete family of analytical solutions is available. In this work we have introduced a more sophisticated numerical minimization method that the presented in [Ciro and Caldas (2014)] to solve the Grad-Shafranov equation, and our results were now benchmarked against EFIT. The DISFUNSOL routine, developed in this work, allows us to control the convergence by weighting differently the error contributions from different quantities, giving to the user more control over the convergence of the numerical solution and to strengthen the description of relevant characteristics of the discharge in an experimental situation. Additionally, at the end of the run, the solution can be expressed as a numerical grid of poloidal flux values or as a symbolic superposition of special functions with a few numerical parameters. The last form of the solution is portable and independent of file architectures and may be valuable in calculations demanding continuous second order derivatives everywhere, which is not satisfied by cubic interpolators in a grid.

# Chapter 4

## Non-axisymmetric discharges

This chapter will be devoted to the description of the magnetic field in weakly non-axisymmetric situations. In these configurations the axisymmetric part of the magnetic field is dominant, but small internal and external non-axisymmetric currents are also considered. Such currents break the axial symmetry of the system and modify the magnetic topology by introducing small magnetic perturbations that play the role of a perturbing Hamiltonian over an integrable system. Other strongly non-axisymmetric configurations, like the achieved in an Stellarator or a Torsatron [Teller (1981)] require a complete three-dimensional treatment that is out of the scope of the present work [Biskamp (1993)].

The magnetic fields under consideration may be inherent to the tokamak design, like the magnetic ripples due to the discrete nature of the toroidal field coils [Zwingmann et al. (2006)], also may be caused by internal plasma instabilities [Biskamp (1993)], or created artificially with external coils in a controlled fashion [Evans et al. (2013)]. As discussed in Chapter 2, the presence of resonant components of the vacuum magnetic field in the rational surfaces tend to create magnetic islands, but the high conductivity of the plasma restricts this behavior through localized plasma currents that suppress the resonant components of the field. When reconnection is allowed, magnetic islands develop and the force-balance condition, if maintained, requires the formation of non-axisymmetric currents in the islands, that act as an additional source of non-axisymmetric magnetic field.

The magnetic field  $\delta\vec{B}$ , created by a stationary non-axisymmetric current density distribution  $\delta\vec{j}$  satisfies [Jackson (1999)]

$$\delta\vec{B}(\vec{r}) = \frac{\mu_0}{4\pi} \int_{\Omega} \frac{\delta\vec{j}(\vec{r}') \times (\vec{r} - \vec{r}')}{|\vec{r} - \vec{r}'|^3} dV'. \quad (4.1)$$

In absence of current sources and sinks the current density is a solenoidal vector field  $\nabla \cdot \vec{j} = 0$ , and can be decomposed in non-overlapping flux tubes like the magnetic field

in Chapter 2, then, the integral becomes a summation over current flux tubes (or current filaments)

$$\delta\vec{B}(\vec{r}) = \sum_i \frac{\mu_0 I_i}{4\pi} \oint_{\Gamma_i} d\vec{r}_i \times \frac{\vec{r} - \vec{r}_i}{|\vec{r} - \vec{r}_i|^3}, \quad (4.2)$$

where  $I_i d\vec{r}_i = \delta\vec{j}(\vec{r}_i) dV_i$ , and  $I_i$  is the current density flux (or simply, the current) along the filament  $\Gamma_i$ , which can be modeled to be closed<sup>1</sup>.

Equation (4.2) can be viewed as the linear superposition of the magnetic fields created by each current filament  $\Gamma_i$ , and the final problem is to define the geometry and current for each one of them. For the case of externally created magnetic perturbation this is straightforward, but in the case of the plasma response the problem becomes more involved. At the end of this chapter we discuss the numerical procedure developed to perform this task, but for now let us introduce the numerical procedure to obtain the magnetic field for a given current configuration.

## 4.1 Magnetic field from known sources

In this section we want to provide some detail on the numerical aspects of determining the magnetic field for a given current coil configuration.

Assume a three-dimensional filament  $\Gamma_i$  carrying a current  $I_i$ . Its magnetic field at  $\vec{r}$  is given by

$$B_i(\vec{r}) = \frac{\mu_0 I_i}{4\pi\epsilon_0} \oint_{\Gamma_i} d\vec{r}_i \times \frac{\vec{r} - \vec{r}_i}{|\vec{r} - \vec{r}_i|^3}. \quad (4.3)$$

To solve this equation numerically we can subdivide the filament in straight segments, so that for an appropriate discretization of the coil we can add together the contributions from all segments (Fig. 4.1).

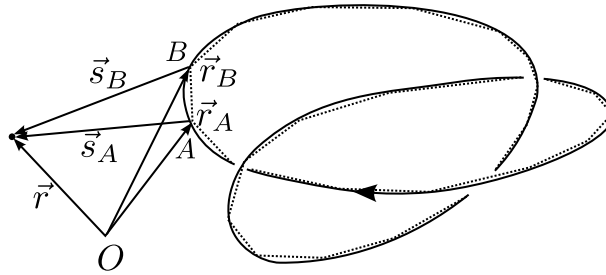


Figure 4.1: Decomposition of an arbitrary three-dimensional filament in a sequence of small straight segments (sizes exaggerated for clarity).

The magnetic field created by the straight segment  $\overline{AB}$  (see Appendix A.5), is given

<sup>1</sup>If the current lines span along surfaces they may not be closed, however, their behavior can be arbitrarily well approximated by continued fractions, that correspond to rational numbers and lead to closed filaments

by

$$\vec{B}_{AB}(\vec{r}) = \frac{\mu_0 I}{4\pi} \vec{B}^\dagger(\vec{r} - \vec{r}_A, \vec{r} - \vec{r}_B), \quad (4.4)$$

where the vector function  $\vec{B}^\dagger(\vec{u}, \vec{v})$  was defined by convenience as

$$\vec{B}^\dagger(\vec{u}, \vec{v}) = \frac{\mu_0 I}{4\pi} \left( \frac{1}{|\vec{u}|} + \frac{1}{|\vec{v}|} \right) \frac{\vec{u} \times \vec{v}}{|\vec{u}||\vec{v}| + \vec{u} \cdot \vec{v}} \quad (4.5)$$

Clearly, this equation only makes sense if the superposition of straight segments defines a closed loop. Individually it does not describe a stationary situation because the charge would be flowing from  $A$  to  $B$  and accumulating, such that the displacement current  $\epsilon_0 \frac{\partial \vec{E}}{\partial t}$  must be taken into account.

If we subdivide the three-dimensional filament  $\Gamma_i$  in a sequence of vertices  $\{\vec{r}_{i,0}, \vec{r}_{i,1}, \vec{r}_{i,2}, \dots, \vec{r}_{i,N_i}\}$ , such that  $\vec{r}_{i,0} = \vec{r}_{i,N_i}$ , the contribution of this filament can be approximated by

$$\vec{B}_i(\vec{r}) \approx \frac{\mu_0 I_i}{4\pi} \sum_{j=0}^{N_i} \vec{B}^\dagger(\vec{s}_{i,j}, \vec{s}_{i,j+1}), \quad (4.6)$$

where  $\vec{s}_{i,j} = \vec{r} - \vec{r}_{i,j}$ , then, the complete non-axisymmetric field becomes

$$\delta \vec{B}(\vec{r}) \approx \frac{\mu_0}{4\pi} \sum_{i=0}^{N_c} I_i \sum_{j=0}^{N_i} \vec{B}^\dagger(\vec{s}_{i,j}, \vec{s}_{i,j+1}), \quad (4.7)$$

where  $N_c$  is the number of coils that describe the non-axisymmetric sources.

The calculation of this magnetic field only involves elementary operations that can be efficiently implemented for numerical calculations. In this research, we have implemented this operations in the module `magnetic_field.h`, which requires an input file with the number of coils, number of nodes per coil, the list of coil currents and a list of vertices in Cartesian coordinates such that the first and last vertex of each filament are the same.

To illustrate the implementation of this calculation, in Fig. 4.2 we show the magnetic vector field created by the Resonant Magnetic Perturbation (RMP) coils at the plasma edge of the DIII-D tokamak discharge #158826, calculated with the module `magnetic_field.h`.

## 4.2 Modeling the plasma response

Now that we have presented the numerical approximations that allows us to calculate the magnetic field for an arbitrary set of current loops, we can consider the problem of modeling the magnetic field created by an unknown non-axisymmetric distribution of current inside the plasma. This internal structure may be created by the plasma response to

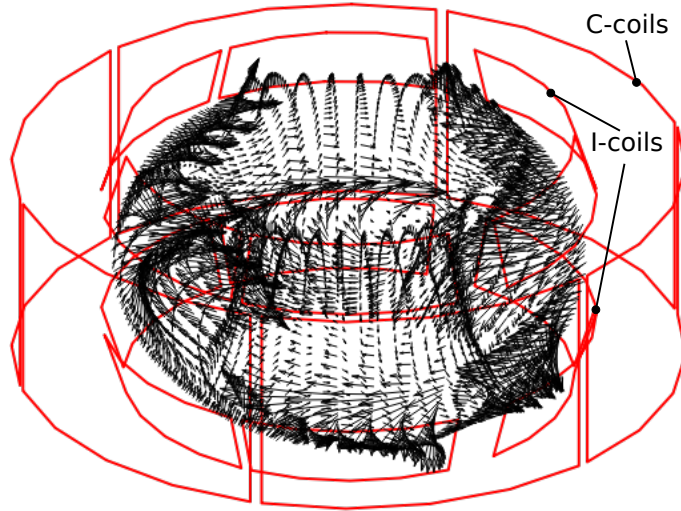


Figure 4.2: Magnetic field created by the Resonant Magnetic Perturbation coils for discharge #158826 of the DIII-D tokamak at the magnetic separatrix of the equilibrium reconstruction.

an external magnetic perturbation, or by the inherent dynamics of the plasma. In strict sense we need to solve the three-dimensional equilibrium problem through some numerical method, however, most tractable procedures extremize the plasma potential energy by performing ideal variations of the magnetic field, precluding topological changes at the resonant surfaces and the plasma edge. This preserves numerically the nested topology and prevents the numerical simulations to reproduce the topological changes observed experimentally [Hudson and Nakajima (2010)]. On the other side, resistive MHD simulations of the tearing modes can be used to calculate the non-axisymmetric fields created in other regions of the plasma, or the vacuum, but these calculations are numerically more involved and require the definition of a considerable set of model parameters.

In this work, we are interested in an effective field modeling based on magnetic measurements that intends to pack a large number of complex effects in a *simple* non-axisymmetric field. With this, we will be able to study the magnetic topology and its effects in the plasma configuration and its interaction with the materials around it.

Assume that we have access to the magnetic field value at several locations outside the plasma, so that we are endowed with a list pairs of the form  $\{\vec{r}_i, \vec{B}_i^{(e)}\}$ , where  $\vec{r}_i$  is the location of the magnetic probe and  $\vec{B}_i^{(e)}$  is the experimental magnetic field. This magnetic field can be decomposed into an axisymmetric part  $\vec{B}_s(\vec{r}_i)$  and a non-axisymmetric part  $\vec{B}_a(\vec{r}_i)$

$$\vec{B}_i^{(e)} = \vec{B}_s(\vec{r}_i) + \vec{B}_a(\vec{r}_i), \quad (4.8)$$

where the subscripts (*s*) and (*a*) stand for “symmetric” and “asymmetric”, in regards to the continuous symmetry respect to  $\phi$ . The axisymmetric part of the plasma magnetic

field can be recovered by doing

$$\vec{B}_s(\vec{r}) = \nabla\psi_{s,v} \times \nabla\phi + \frac{R_0 B_0}{R} \hat{\phi}, \quad (4.9)$$

where  $\psi_v$  is the magnetic poloidal flux created by all the axisymmetric currents in the system which include the toroidal current in the plasma and the poloidal field coil currents. Recalling equation (3.29), this flux can be written as

$$\psi_{s,v}(R, z) = \sum_{i=1}^{N_f} I_{f,i} G(R, z; R_i, z_i) + \int_{\Omega} j_{\phi}(R', z') G(R, z, R', z') dR' dz', \quad (4.10)$$

where  $G(R, z; R', z')$  is the Green's function of the Grad-Shafranov operator defined in (3.27),  $I_{f,i}$  are the currents in the filaments that discretize the poloidal field coils, which can be obtained from the discharge information, and  $j_{\phi}(R', z')$  is the toroidal plasma current obtained by solving the axisymmetric equilibrium problem (see Chapter 3). The subscript  $v$  indicates that the magnetic measurements are taken in the vacuum where the kinetic pressure and diamagnetic effects are absent.

The non-axisymmetric magnetic field, in turn, can be decomposed in two parts, one generated by the unknown non-axisymmetric plasma currents, and the field generated by the external non-axisymmetric coils

$$\vec{B}_a(\vec{r}_i) = \vec{B}_a^{(p)}(\vec{r}_i) + \vec{B}_a^{(c)}(\vec{r}_i), \quad (4.11)$$

where the superscript  $(p)$  stands for “plasma” and  $(c)$  for “coils”. The magnetic field corresponding to the coils can be easily determined using the Biot-Savart calculator introduced in the previous section, and the information about the currents applied in the discharge of interest. Inserting (4.11) into (4.8) we can estimate the magnetic field corresponding to the unknown non-axisymmetric plasma currents

$$\vec{B}_{a,i}^{(p)} = \vec{B}_i^{(e)} - \vec{B}_s(\vec{r}_i) - \vec{B}_a^{(c)}(\vec{r}_i). \quad (4.12)$$

The last expression combines fields determined experimentally with fields modeled by a numerical Biot-Savart calculation and equilibrium reconstruction, so, strictly speaking, it is not an experimental value, but can be used as the target values for an optimization routine that attempts to determine the structure of the plasma current response compatible with the measurements.

From the discussion carried in Chapter 2, for ideal plasmas, the current sheets that suppress the resonant components of the magnetic field reside around the rational surfaces. These currents are defined so that they prevent the formation of magnetic islands. In a

similar fashion, for resistive plasmas, the formation of equilibrium magnetic field islands require significant alterations in the current density near the rational surfaces. These changes occur so that the new current density satisfies the equilibrium condition  $\vec{j} \times \vec{B} = \nabla p$  for the new isobaric surfaces.

With this in mind, our modeling attempts must consider non-axisymmetric currents in these locations. Experimentally, the development of a tearing mode leads to a phase inversion on the electron cyclotron emission (ECE) signal across the rational surface [Berrino et al. (2005); Bornatici et al. (1983)], and this can be used to determine the precise location of the most relevant rational surface to model the plasma response.

From this point we just need to model the relevant currents at the rational surface. For now, let us consider that the response current can be described by the superposition of a discrete set of helical filaments aligned with the magnetic field lines at the relevant magnetic surface(s). The response current density, then takes the form

$$\delta\vec{j}(\vec{k}, \vec{r}) = \sum_{j=1}^{N_h} I_j \delta(\vec{r} - \vec{r}_h^{(j)}(\phi - \phi_{0,j})) \hat{b}, \quad (4.13)$$

where  $\delta(\vec{r})$  is the Dirac delta function,  $\vec{r}_h^{(j)}(\phi)$  is the parametric equation describing the  $j$ 'th helix starting in the low field side (LFS<sup>2</sup>) of the magnetic surface at  $\phi = 0$ , and carrying a current  $I_j$  in the direction of the magnetic field  $\hat{b}$  at  $\vec{r}$ . Notice that the current density depends on the parameters vector  $\vec{k}$ , containing the currents and phases of every filament composing the plasma response  $\vec{k} = \{I_1, I_2, \dots, \phi_{0,1}, \phi_{0,2}, \dots\}$ .

Since the elementary currents are aligned with the magnetic field lines they can be determined by integrating the equations for the magnetic field lines starting in  $\phi_0$  at the LFS mid-plane. These equations take the form

$$\frac{dR}{d\phi} = \frac{RB_{s,R}}{B_{s,\phi}}, \quad \frac{dz}{d\phi} = \frac{RB_{s,z}}{B_{s,\phi}}, \quad (4.14)$$

where the subscript  $s$  indicates the use of the axisymmetric fields for this calculation. In this work we use an adaptive Runge-Kutta method with the Cash-Karp Butcher tableau, which results in a better numerical stability. Comparison with other flavors of the Runge-Kutta method can be checked in Appendix B.2. In this work we use several helical filaments with the same shape but starting at different relative phases and carrying different currents.

The parameters vector  $\vec{k}$  must be optimized to obtain the best possible fit of the target values described in equation (4.12). The magnetic field created by these filaments can be

---

<sup>2</sup>The low field side corresponds to the region of the plasma with weaker toroidal magnetic field, i.e. the outer region measured from the  $z$  axis.

written in terms of the unknown currents and phases  $\{I_j, \phi_{0,j}\}$ . To do this we use the Biot-Savart calculator discussed above,

$$\delta\vec{B}(\vec{k}, \vec{r}) \approx \frac{\mu_0}{4\pi} \sum_{j=0}^{N_h} I_j \sum_{k=0}^{N_j} \vec{B}^\dagger(\vec{s}_{j,k}, \vec{s}_{j,k+1}), \quad (4.15)$$

where

$$\vec{s}_{j,n} = \vec{r}_h^{(j)}(n\Delta\phi - \phi_{0,j}) - \vec{r}, \quad (4.16)$$

is the location of the  $n$ 'th node of the filament. The filaments are discretized by following the field lines in portions of size  $\Delta\phi = 2\pi q_h/N_h$ , where  $q_h$  is the safety factor of the corresponding magnetic surface and  $N_h$  is number of nodes in the discretization.

To find the currents and phases of the collection of filaments that better describe the available magnetic measurements we need a functional that reaches its minimum when the measurements are well approximated. For this we define

$$\mathcal{E}(\vec{k}) = \sum_{j=1}^{N_p} \left[ \vec{B}_{a,j}^{(p)} - \delta\vec{B}(\vec{k}, \vec{r}_j) \right]^2, \quad (4.17)$$

where  $\vec{r}_j$  is the location of the  $j$ 'th magnetic probe and  $\vec{B}_{a,j}^{(p)}$  is the magnetic field measured in this location. The optimum configuration corresponds to the vector  $k$  for which this functional is minimum (Fig. 4.3)

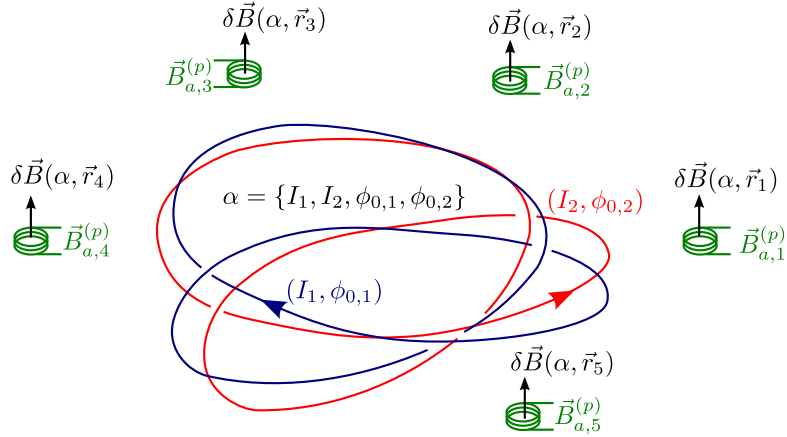


Figure 4.3: Example of the use of five probes to adjust the parameters of two filaments. The optimization problem consists in performing variations  $\delta\vec{k}$ , of the parameters  $\vec{k} = \{I_1, I_2, \phi_{0,1}, \phi_{0,2}\}$ , until the magnetic field  $\delta\vec{B}(\vec{k}, \vec{r})$ , created by the model filaments at the tokamak probes approximates well the experimental measurements in these locations  $\vec{B}_{a,j}^{(p)}$ .

Notice that the error function (4.17) depends linearly on the currents  $\{I_j\}$  but non-linearly on the phases  $\{\phi_{0,j}\}$ , consequently, the minimization can not be casted in a linear form and we require a numerical minimization scheme. The fundamental idea behind any

optimization method is to perform a variation  $\delta\vec{k}$ , such that the error gets reduced, this is, such that

$$\mathcal{E}(\vec{k} + \delta\vec{k}) < \mathcal{E}(\vec{k}). \quad (4.18)$$

Assuming that  $\delta\vec{k}$  is small and performing a first order expansion in the LHS we get that

$$\nabla_k \mathcal{E}(\vec{k}) \cdot \delta\vec{k} < 0. \quad (4.19)$$

This is quite intuitive, if  $\delta\vec{k}$  is in a direction contrary to the gradient of  $\mathcal{E}(\vec{k})$  we are moving to a new set of parameters where the error is smaller. To determine  $\delta\vec{k}$  various approaches exist, in our case we use a damped least-squares algorithm as the Levenberg-Marquardt method presented in Appendix B.1. For this situation, the components of the magnetic field created by the filaments in the locations of the probes play the role of the model function, and the experimental measurements of the magnetic field are the target values of the function. At this point the numerical procedure used to optimize this functional is very similar to the one used to adjust the parameters of the equilibrium expansion in the semi-analytical solutions of Chapter 3. The routine `adjust_helices.c` was developed to perform this task. It requires a list with the magnetic probe measurements for the target function, and an equivalent list for the magnetic field at the probes for a single helix with current 1.0 A. These magnetic fields must be provided for the same helix at different phases  $\phi_0$ , at regular intervals  $\Delta\phi_0$ . Using this information, the routine simulates the effect of several helices at different toroidal phases and different currents, then optimizes these parameters to obtain the optimum configuration that is then used to create a file `.coils` that can be interpreted by our Biot-Savart calculator to calculate the magnetic field at arbitrary locations.

To illustrate this section we want to show the resulting filament configuration for the DIII-D shot #158826, where a tearing mode develops and breaks the axial symmetry, leading to a slowly rotating internal structure (Fig. 4.4).

It was observed that for this shot the phase inversion of the ECE signal occurs at the radial position of the  $q = 2$  surface of the equilibrium reconstruction. For this situation the magnetic field evolves in time, but as will be shown in the last chapter there is a non-inertial rotating frame where the problem becomes approximately stationary and we can solve the problem with the methods described in this section. For the discharge of interest the magnetic field in the LFS probes is well approximated by three filament currents with safety factor  $q_h = 2$ . When provided a reasonable initial guess for the parameters, the routine converges to a minimum value of the error, where  $\{I_1, I_2, I_3\} = \{24.4, -17.2, -14.5\}$  kA and  $\{\phi_1, \phi_2, \phi_3\} = \{348.3^\circ, 70.2^\circ, 117.9^\circ\}$ . The number of filaments was determined by requiring a significant error reduction for an small increase in the number of filaments,

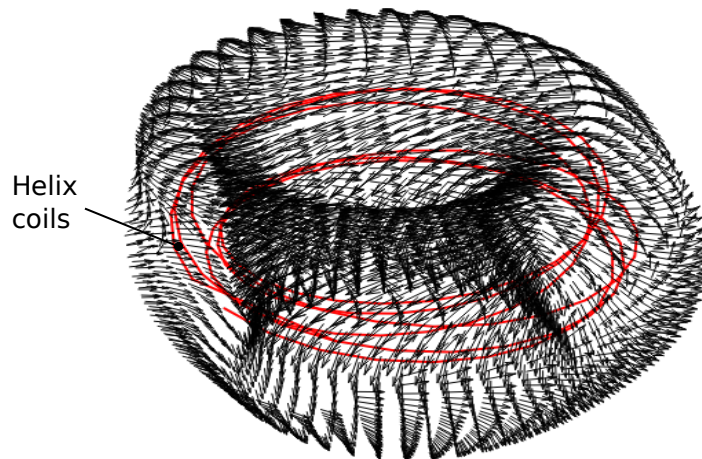


Figure 4.4: Magnetic field created by three helical coils that model the magnetic contribution from a tearing mode in the DIII-D tokamak discharge #158826. The magnetic field is only represented at the axisymmetric separatrix of the equilibrium reconstruction.

thereby, *three* filaments gave a large error reduction respect to *two* filaments, while *four* or more filaments give a poor improvement respect to *three*. The details about the approximations involved in the determination of the rotating reference frame will be presented in Chapter 5 to conclude this work.

### 4.3 Magnetic invariant manifolds

In Chapter 3 and the previous sections we were concerned with the description of the axisymmetric and non-axisymmetric components of the magnetic field in real single-null tokamak discharges. This involved solving the Grad-Shafranov equation for the axisymmetric equilibrium problem with realistic boundary conditions and external currents. Then we studied the problem of describing the magnetic field from non-axisymmetric source currents, where a fast Biot-Savart calculator was implemented for arbitrary coil geometries and the plasma response itself modeled from filamentary field-aligned currents. In this section we want to show a relevant application of these fields in the determination of the plasma edge of non-axisymmetric discharges and its importance for magnetic confinement devices.

In tokamak devices, an ideally axisymmetric magnetic field is created to confine a high-temperature plasma in a toroidal volume. Formally, from the divergence-free nature of the magnetic field, its streamlines can be obtained from the Hamilton equations (Chapter 2) and, consequently, the axial symmetry must lead to the conservation of the magnetic flux along the field lines, which in turn are integrable and span well defined toroidal surfaces. In modern tokamak discharges, a magnetic saddle is created at the plasma edge

and the plasma becomes limited by a homoclinic magnetic surface. This separatrix is, however, structurally unstable in three-dimensions [Guckenheimer and Holmes (1983)], consequently, any arbitrary small departure from axisymmetry will break the magnetic separatrix into a pair of invariant manifolds converging or diverging from the perturbed magnetic saddle.

To understand this concept, consider Fig. 4.5. In the axisymmetric case, the poloidal magnetic field vanishes at the same point for all toroidal angles, and the combined X-points at every poloidal section define a circle  $(R, z) = (R_s, z_s), 0 \leq \phi < 2\pi$ , where the magnetic field is purely toroidal. Because of this, a magnetic field line starting at  $(R_s, z_s)$  describes a closed circle passing through every X-point (Fig.4.5-left). The separatrix, is a continuous surface composed of magnetic field lines that converge to this circle when followed in any direction

In non-axisymmetric situations we can say, equivalently, that the X-points are defined by a field line closing after one toroidal cycle (Fig. 4.5-right). In the following we will refer to this field line as an Unstable Periodic Orbit (UPO) [Guckenheimer and Holmes (1983)], or a saddle orbit. With this we can implement the definition of a separatrix for non-axisymmetric situations with an alteration. Now, the surface is defined by the field lines converging to the UPO when followed in one direction. This causes the existence of two different surfaces or invariant manifolds defining the confined region. The *unstable manifold* is spanned by field lines converging to the UPO when followed opposite to the field direction, and, conversely, the *stable manifold* is spanned by the field lines converging to the UPO when followed in the direction of the field. Both surfaces are infinite and non-self-intersecting, but can intersect each other in very intricate patterns. The set of orbits converging to the UPO when followed in any direction lie on the intersections of the stable and unstable manifolds, referred to as homoclinic points, and they do not span a continuous surface, i.e. there are gaps between these orbits and they can not be the generalization of the axisymmetric separatrix.

Experimental evidence of these invariant manifolds have been observed in numerous tokamak laboratories, by tangential imaging of single-null discharges in MAST [Kirk et al. (2012)] and by heat deposition patterns on the divertor tiles of DIII-D [Evans et al. (2005)], JET [Rack et al. (2014)], Asdex [Eich et al. (2005)] and others. In a first approximation, the magnetic field lines close to the manifolds drive the charged particles to collide with the divertor tiles in coherent structures delimited by the manifold intersection with the material surfaces. Calculation of these structures by means of laminar plots evidences the intricate patterns produced by the invariant manifolds in suitable Poincaré sections [Wingen et al. (2005); Kroetz et al. (2010); da Silva et al. (2002); Roeder et al. (2003)], and, consequently, the precise determination of these curves is an important factor

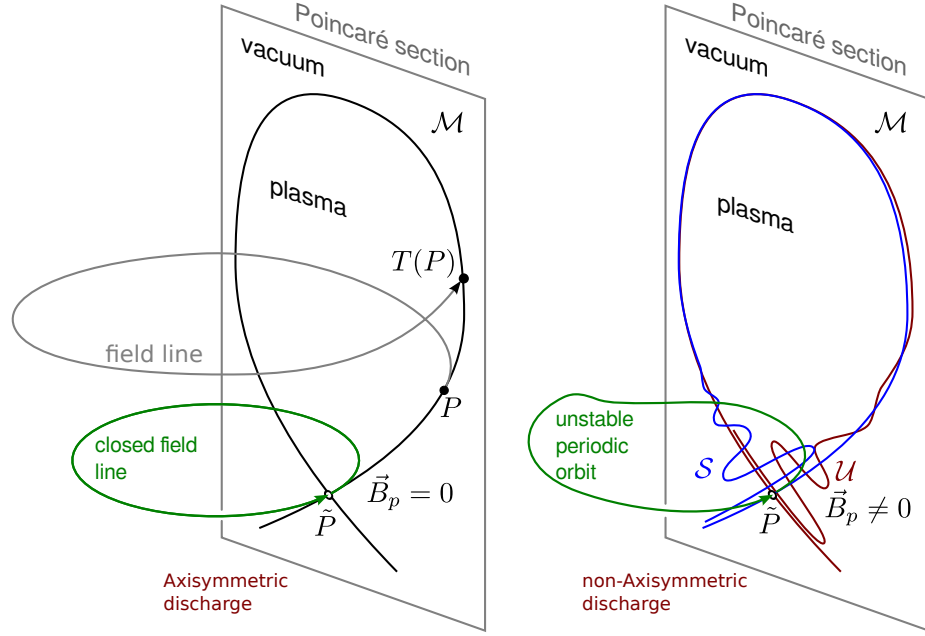


Figure 4.5: The invariant manifolds in the Poincaré section. In the axisymmetric case (left) the manifolds are degenerated and form a unique curve in the plane  $\mathcal{M}$ , while in the non-axisymmetric case (right), the manifolds split and oscillate back and forth intersecting each other. For this figure, the toroidal field and plasma current are considered counterclockwise.

to determine the features of the plasma edge subjected to non-axisymmetric magnetic perturbations.

Let us formalize the concept of invariant manifolds in a Poincaré section. First of all, a *Poincaré section* is a surface  $\mathcal{M}$  which is everywhere transverse to the magnetic field. In Fig. 4.5 it is simply a  $\phi = \text{const.}$  plane. The *Poincaré map* is a function  $T$  that transforms one point  $(R, z) \in \mathcal{M}$  to another point  $(R', z') \in \mathcal{M}$  by following the magnetic field line starting at  $(R, z)$  until it crosses again  $\mathcal{M}$ . The inverse map  $T^{-1}$  does the same but following the field line in the opposite direction. Consequently,  $T^{-1}(T) = T(T^{-1}) = I$  is the identity map that applies the point  $(R, z)$  on itself.

With the previous definitions, it is clear that the point  $\tilde{P} = (R_s, z_s)$  belongs to the UPO if it satisfies  $T(\tilde{P}) = \tilde{P}$ , so that it corresponds to a fixed point of the Poincaré Map. Provided that such a fixed point exists, its *stable manifold* is defined as the set

$$\mathcal{S}(\tilde{P}) = \{P \in \mathcal{M} | T^n(P) \rightarrow \tilde{P} \text{ when } n \rightarrow \infty\}. \quad (4.20)$$

In other words, is the set of points in  $\mathcal{M}$  such that converge to  $\tilde{P}$  upon repeated application of the Poincaré map  $T$ . The stable manifold is a continuous family of points, i.e. they form a continuous curve in  $\mathcal{M}$  (Fig. 4.5-right). In analogy, the *unstable* manifold is the

set

$$\mathcal{U}(\tilde{P}) = \{P \in \mathcal{M} | T^{-n}(P) \rightarrow \tilde{P} \text{ when } n \rightarrow \infty\}. \quad (4.21)$$

Once we identify these invariant manifolds in the Poincaré plane we can obtain the three-dimensional invariant surfaces by following all the field lines passing through the invariant manifolds in the Poincaré plane, and that give us the non-axisymmetric version of the plasma edge, which now involves a pair of intersecting invariant surfaces. For numerical details on the determination of  $\tilde{P}$ , see Appendix B.3. Once identified this point it can be used to build the UPO by integrating the magnetic field starting at  $\tilde{P}$  until it closes after one toroidal cycle.

In the neighborhood of the fixed point  $\tilde{P}$ , at the transverse plane, the invariant manifolds can be approximated using polynomials that adjust the behavior of neighboring field lines. Then, small segments of the manifold cuts can be mapped forward or backwards to build the rest of the manifold cuts far from the UPO. In this work we have developed a high resolution adaptive method for calculating the invariant manifolds in a given Poincaré section to arbitrary extent and precision [Ciro et al. (2016a)]. This method was then generalized in a C routine named MAGMAN (acronym for MAGnetic MANifolds), to describe the invariant manifolds as continuous surfaces in three-dimensions, such that its intersection with any arbitrary surface of interest, like the tokamak chamber, can be determined *a posteriori* without restricting the original calculation. In Appendix B.3 we present a detailed discussion in the numerical aspects of this calculation at the Poincaré section, and here we will paraphrase its generalization of the surface calculation.

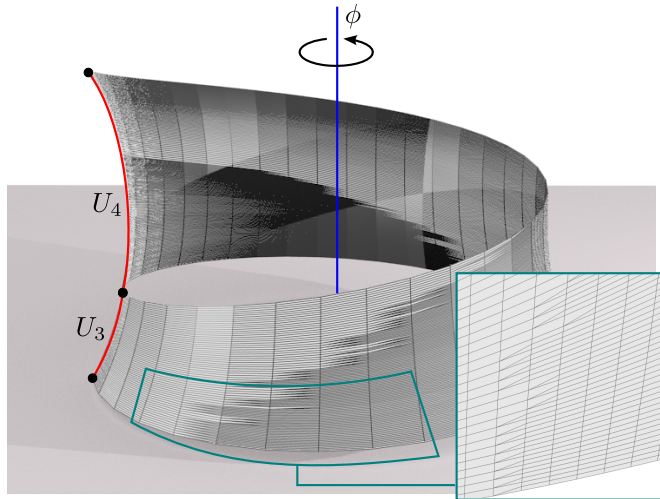


Figure 4.6: Advection of the unstable manifold by the tokamak magnetic field after one toroidal cycle. In the detail we can see the simultaneous refinement of the mesh, where new intermediate points are created when neighboring points get too sparse.

In essence, the MAGMAN routine consists in the advection of manifold segments by the magnetic field. The resolution of the manifold is maintained by requiring that the

separation between consecutive points do not surpass a established critical distance. In Fig. 4.6 we can see how the 3th elementary segment of the unstable manifold gets advected along the field lines towards the segment  $U_4$ , while the resolution is maintained by the mesh refinement process. This advection-refinement method is more efficient and precise than starting all the orbits near the Saddle Orbit, that may lead to considerable roundoff error.

To illustrate the behavior of the manifolds in a typical non-axisymmetric situation we consider a simplified configuration in which the DIII-D equilibrium of discharge #158826 is perturbed by the C-coils alone (see Fig. 4.2), carrying currents of  $\pm 2.5kA$  in a configuration  $(+, -, +, -, +, -)$ , such that the dominant toroidal mode is  $n = 3$ . For now, let us dismiss the plasma response, and consider the C-coils as the only source of non-axisymmetric field, i.e. the magnetic perturbation only involves  $\vec{B}_a^{(c)}(\vec{r})$  (see Eq. (4.11)).

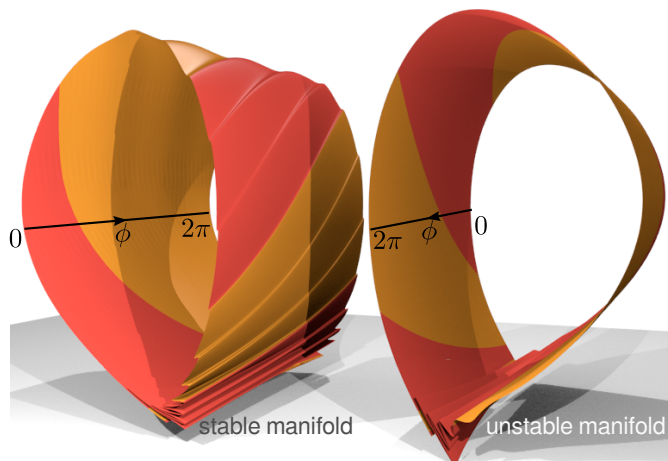


Figure 4.7: Stable and unstable manifolds calculated with MAGMAN for discharge #158826, subjected to an external perturbation with dominant  $n = 3$ . For clarity, toroidal coordinate was straightened to have a better view of the surface folding, and the manifolds are shown separated. The colors red and orange are used to differentiate between the elementary segments after each toroidal turn.

As the field lines pass through the LFS they get pushed and pulled by the magnetic field of the C-coils. This creates oscillations in the manifold surface that get advected forward (and backwards) by the magnetic field lines, and accumulate near the saddle due to the low poloidal magnetic field. The intersection of the stable and unstable manifolds defines the so called *homoclinic crossings* that give rise to the separatrix chaos in non-integrable Hamiltonian systems [Guckenheimer and Holmes (1983)], which is driven by the proliferation of unstable periodic orbits of different periods.

Another important consequence of the accumulating oscillations near the magnetic saddle is the formation of *homoclinic lobes* that get stretched and can intersect the tokamak chamber carrying an important heat load to the divertor tiles. In chapter 5 we study

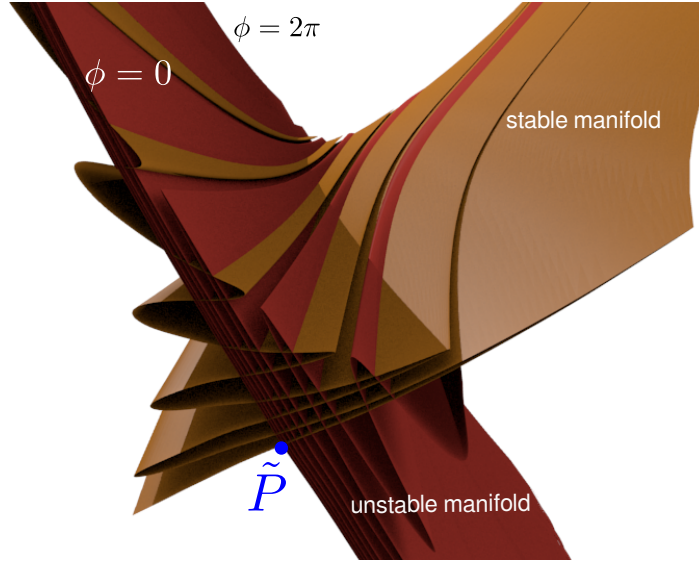


Figure 4.8: Detail of the manifolds intersection that leads to the separatrix chaos at the plasma edge. The manifolds intersect at magnetic field lines that converge to the saddle orbit (indicated by  $\tilde{P}$ ) when followed in any direction. Here the red color is used for the unstable manifold and the yellow for the stable one.

these heat fluxes in more detail, but for now we want to point out that any sufficiently large non-axisymmetric current distribution has the potential to cause separatrix splitting and delivering the hot plasma to the tokamak components in unexpected locations. This is why the precise determination of these structures is important, as it plays an important role in the design of the Plasma Facing Components and their location.

## 4.4 Chapter conclusions

For stationary, divergence-free currents, the magnetic field can be decomposed into partial contributions from several current tubes. In this fashion the magnetic field can be calculated as a superposition of the contributions from currents in the plasma and the external currents used to confine and control the plasma. Based in this perspective we have introduced a method for modeling the measured magnetic field in tokamak devices using a suitable set of helical currents inside the plasma. The parameters of the currents array can be adjusted by minimizing an error functional based on the experimental data and the Biot-Savart calculation of the magnetic field. This allows us to model the magnetic field in regions where it was not measured, which can be useful in the solutions of inverse equilibrium problems and the determination of important topological artifacts like magnetic islands and the non-axisymmetric plasma boundary. Another important task was the development of an adaptive method for the invariant manifolds calculation, which allowed us to determine the impact of internal non-axisymmetric currents in the magnetic

topology of the plasma edge. The homoclinic lobes and the intersection of the stable and unstable manifolds were determined with great detail and can be calculated for realistic situations to compare with optical diagnostics.



# Chapter 5

## Modeling time-dependent heat patterns in DIII-D tokamak

In this chapter we want to show a practical application of all the concepts and methods introduced so far. The problem of interest is a DIII-D discharge developing a slowly rotating tearing mode at the  $q = 2$  surface. The main objective of this chapter is understanding the interaction of the internal non-axisymmetric currents with the magnetic separatrix in single-null discharges. As mentioned in the previous chapter, this knowledge is important to understand the influence of the plasma instabilities on the heat deposition in the divertor tiles. In ITER discharges a rotating non-axisymmetric divertor heat flux will cause periodic variation in the thermal loading of the target plates and cooling lines resulting in thermal and mechanical fatigue of these components leading to premature failures. This type of slowly rotating non-axisymmetric internal mode must be controlled to prevent damage to the divertor.

### 5.1 Experimental observations

The basic evidence of the interplay between the magnetic topology and the plasma edge, or, even, the definition of the plasma edge through the invariant manifolds, is the temporal correlation between the magnetic fluctuations at the magnetic probes and the evolution of the heat-flux pattern in the Plasma Facing Components (PFCs).

In this work, we consider the discharge #158826 of DIII-D where a small stationary  $n = 2$  field was applied. A non-rotating locked mode forms at 1625 ms and remains stationary until 2015 ms when it begins to rotate slowly at approximately 6.67 Hz. During the non-rotating phase two heat flux peaks form at the outer strike point and remain fixed until the mode begins to rotate. In Fig. 5.1 we show the poloidal magnetic field fluctuations at different toroidal positions in the Low Field Side (LFS) mid-plane and the

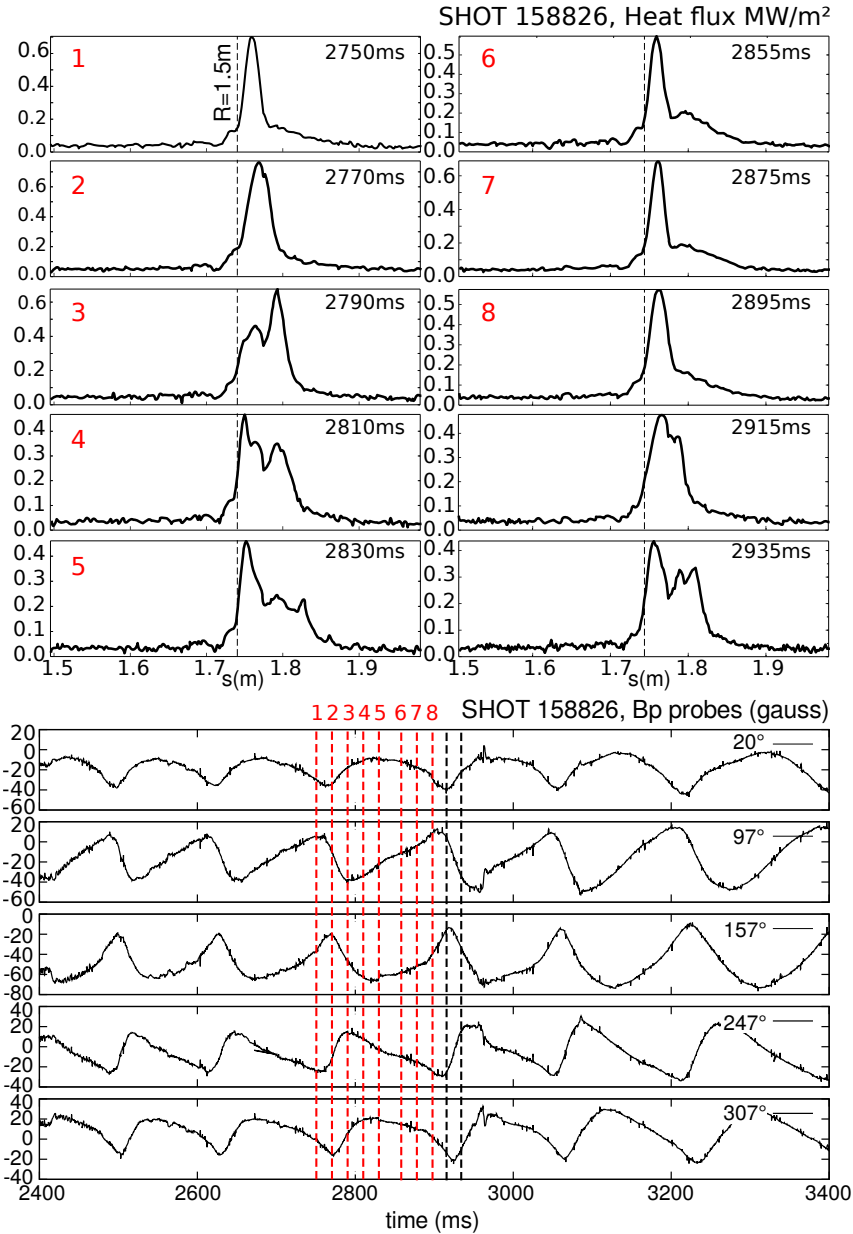


Figure 5.1: Heat flux profiles in the LFS strike point for discharge #158826 for ten time slices between 2750 ms and 2935 ms (top) and poloidal magnetic field fluctuations for various toroidal positions measured on the LFS mid-plane (bottom). The black dashed line in the heat flux profiles identify the strike point position obtained from the equilibrium reconstruction of the discharge, and the red dashed lines in the probe signals correspond to the times for the heat profile measurements during one period of the magnetic signals (150 ms). The coordinate  $s$  in the heat flux profiles corresponds to the poloidal distance along the DIII-D wall, measured counterclockwise from the HFS mid-plane. For these profiles  $s = R + 0.239$  m, with  $R$  the cylindrical radial coordinate.

corresponding measurements of the heat flux from an infrared (IR) camera pointing to the lower divertor region during the rotating stage. As the magnetic signals complete one cycle, the heat flux profile completes one bifurcation cycle, where a single peak splits into

two or three peaks that spread to the LFS and vanish.

This type of behavior is expected if the non-axisymmetric field created by an internal instability is changing periodically the magnetic topology, resulting in a periodic separation of the strike points measured by the IR camera [Evans et al. (2005)].

In this shot, the ECE signal presents a phase inversion across the  $q = 2$  surface indicating the presence of a tearing island. Also, the modulation in the radial and poloidal magnetic fields measured at several toroidal positions for the same poloidal location are consistent with a  $q = 2$  tearing mode rotating at approximately 6.67 Hz. The amplitude of the mode grows slowly, but it is modeled to be constant during the heat flux measurements. It is important to point out that although the phase differences between the signals are consistent with the rigid rotation of the mode, the waveforms captured at different toroidal locations present different shapes, indicating that the internal structure is not rotating rigidly, but may contain elements moving at different frequencies or even oscillating. However, these effects are not included in the model as they do not introduce information that can be resolved with the IR camera, also, the dominant mode provides substantial agreement with the available experimental data.

## 5.2 Magnetic perturbation modeling

In order to show a clear correlation between the magnetic signals and the divertor heat flux we will concentrate in modeling the time-dependent part of the magnetic field, which coincides experimentally with the heat flux becoming non-stationary. In analogy with Chapter 4, we split the total magnetic field in its axisymmetric and non-axisymmetric components  $s$  and  $a$  respectively

$$\vec{B}(R, \phi, z, t) = \vec{B}_s(R, z) + \vec{B}_a(R, z, \phi, t). \quad (5.1)$$

Where  $\vec{B}_s$  is the axisymmetric part of the magnetic field, that we also assume to be stationary during the period of interest, and  $\vec{B}_a$  is the time-dependent non-axisymmetric part. The symmetric field  $\vec{B}_s$  can be determined by solving the Grad-Shafranov equation while adjusting a set of plasma profiles consistent with the measured plasma parameters Lao et al. (1985). For this part we use the EFIT equilibrium reconstruction of the discharge #158826 during the period of interest. Just like in the stationary case, let us decompose the non-axisymmetric field in two parts, one due to the external non-axisymmetric coils ( $c$ ), and the other corresponding to the non-axisymmetric plasma current ( $p$ ), i.e.

$$\vec{B}_a(R, z, \phi, t) = \vec{B}_a^{(p)}(R, z, \phi, t) + \vec{B}_a^{(c)}(R, z, \phi). \quad (5.2)$$

Where the field due to the external sources, like the I and C-coils of DIII-D, is stationary, and  $\vec{B}_a^{(p)}(R, z, \phi, t)$  encompasses the time-dependent plasma response to the external perturbation and the field created by the internal instabilities like tearing or kink modes.

As will be discussed at the end of this section, the non-axisymmetric magnetic field created by the plasma currents is much stronger than the created by the external currents in the separatrix region of discharge #158826. For this reason it is safe at this point to approximate the total non-axisymmetric field by the one created by the internal asymmetric currents

$$\vec{B}_a(R, z, \phi, t) \approx \vec{B}_a^{(p)}(R, z, \phi, t). \quad (5.3)$$

In more general situations the magnetic field changes in time and the field lines description becomes four-dimensional. In this scenario, the magnetic invariants and the strike patterns evolve in time and must be calculated for each moment. However, in the special case in which the magnetic perturbation rotates toroidally we can calculate the invariants in a rotating frame and then recover the temporal evolution in the laboratory frame. Experimental observations of heat deposition patterns consistent with the rigid rotation of an invariant manifold have been observed in Evans et al. (2005), where the heat pattern evolution was phase correlated with a slowly rotating or quasi-stationary tearing mode. However, a quantitative agreement between the heat pattern and the manifold calculation requires modeling the non-axisymmetric fields created by the plasma response.

Based on the previous section, the experimental phase shift between magnetic fluctuations at different probes suggests a dominant rigid rotation of the internal source currents, and a smaller contribution from non-rotating sources that reflect in the waveform difference between probes. From this point, we consider the influence of the dominant rotating component to obtain a simple three-dimensional rigid description that describes reasonably well the experimental heat patterns in Fig. 5.1. To model this field we consider a non-axisymmetric current distribution inside the plasma, rotating toroidally at the measured dominant frequency of  $\nu_0 = 6.67Hz$ , and creating the measured magnetic fluctuations outside the plasma. In the present situation, the rotation is quite slow, and we can approximate

$$\vec{B}_a^{(p)}(R, z, \phi, t) \approx \delta\vec{B}(R, z, \phi - \Omega t), \quad (5.4)$$

where  $\delta\vec{B}(R, z, \phi)$  is the response magnetic field created by the internal currents as measured in a non-inertial rotating frame with angular velocity  $\Omega = 2\pi\nu_0$ . In a first approximation, the toroidal motion is considered to be uniform, so that the phase changes linearly with  $t$ .

For clarity, we will study the three-dimensional topology of the magnetic field in the rotating frame where the perturbation becomes stationary. Then we will recover

the spatio-temporal dynamics in the laboratory frame to compare with the experimental observations. In a strict sense,  $\vec{B}_s$  must be transformed to this non-inertial frame, but given the low frequency of rotation we use the field obtained through MHD equilibrium in the laboratory frame. To estimate the error of this assumption, notice that the fictitious force density  $nM_i R_0 \Omega^2$  is of the order  $10^{-4} N/m^3$ , while the laboratory magnetic forces  $\vec{j} \times \vec{B}$  and pressure gradient  $\nabla p$  are of the order  $10^3 N/m^3$ . Consequently, no significant changes on  $\vec{j}_s$  and  $\vec{B}_s$  are expected in the rotating frame.

To model the response field  $\delta\vec{B}$  we consider a minimal set of internal helical filaments, carrying the non-axisymmetric currents inside the plasma and use the magnetic measurements at different angular positions to adjust simultaneously the currents and phases of all the filaments. This simple approach allows us to approximate the experimental magnetic field near the plasma edge without knowing the exact current sources, and without requiring MHD calculations.

To model the non-axisymmetric field produced by the helical modes at  $q = 2$  we consider a set of helical filamentary currents resting at an internal magnetic surface of the EFIT axisymmetric equilibrium reconstruction of the shot [Lao et al. (1985)]. This approach is similar to the one used to model the plasma response to applied resonant magnetic perturbations (RMPs) in COMPASS-D [Buttery et al. (1996); Cahyna et al. (2011)]. However, in this situation, we do not prescribe the filaments using the X and O points induced by the RMPs, but use a non-linear optimization technique to adjust the phases and currents of the filaments to reproduce the measured magnetic fluctuations at the magnetic probes in the (LFS) mid-plane where the probes are located.

Before we proceed to the adjustment of the helical currents we need to make additional comments on the helices location. The modeling of the plasma response through helical filaments is reasonable when we measure the response fields far from these sources. This happens because the actual plasma response currents are distributed along surfaces or volumes and we are trying to capture their relevant features using discrete filaments.

For the DIII-D discharge #158826, the  $q = 2$  surface is very close to the magnetic separatrix, and locating helical filaments at this surface to model the plasma response may cause unphysical near field effects due to the discrete nature of the filaments. Increasing the number of filaments, while reducing the current in each filament will not improve the near-field situation, because the invariant manifolds oscillate across several axisymmetric surfaces near the unperturbed separatrix and it can, in principle, move across the  $q=2$  surface. In this situation, regardless of the large number of filaments or their small current, the perturbation field grows unbounded near the filaments and can nonphysically distort the manifold. Consequently, we need to move the source to more internal surfaces.

Since our approximations are not intended to model the internal magnetic topology

self-consistently, we can locate the perturbation sources arbitrarily, whenever we can maintain the spectral properties of the actual perturbation source and reproduce the measured magnetic fluctuations. The location of the source currents do affect the internal structure of the invariant manifolds, but their more explicit features like number of lobes, lobe width, and the lobe radial excursion, are mostly determined by the dominant mode numbers and their relative intensities, and these figures can be conserved when changing the location of the sources.

In this work, we maintain the *safety factor* of the model helices while changing the helix location. This is achieved by integrating the field lines in the surface of interest until it completes two poloidal cycles, then the toroidal coordinates of the filament nodes are rescaled so that the filament becomes closed. This gives us the same topology of the  $q = 2$  field lines in any internal surface. Since the poloidal magnetic fluctuations drive the manifold deformations, we characterize the helical source at different magnetic surfaces by measuring the ratio between the normal and tangential magnetic fluctuations at the unperturbed separatrix. In Fig. 5.2 we show the fluctuations ratio for 100 helical sources at different magnetic surfaces between the magnetic axis and the plasma edge. Clearly, this ratio depends weakly on the chosen magnetic surface and we can use filaments in a more internal surface such that the near field effects are not important.

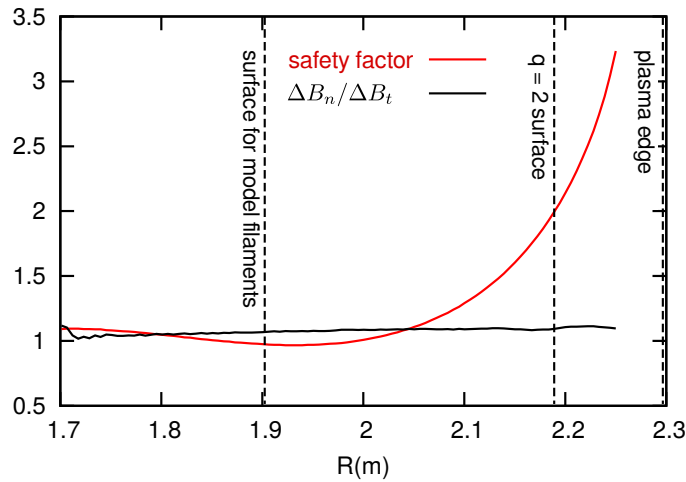


Figure 5.2: The Ratio between normal and tangential magnetic fluctuations created at the separatrix by the  $q_h = 2$  helical filament in an internal surface depends weakly on the surface position. The  $q = 2$  surface of discharge #158826 is at  $\sim 12$  cm from the plasma edge in the LFS mid-plane causing important near-field effects in the separatrix. To avoid these undesired effects the magnetic surface for the helical filaments is taken at 40 cm from the plasma edge.

In analogy with the stationary situation, for a set of  $N_f$  filaments with helicity  $q_h$  on an *arbitrary* magnetic surface, the non-axisymmetric part of the current density inside in

the rotating frame takes the form

$$\delta \vec{j}(\vec{r}) = \sum_{i=1}^{N_f} I_i \delta(\vec{r} - \vec{r}_h^{(i)}(\phi - \phi_{0,i} - \Omega t)) \hat{h}, \quad (5.5)$$

where  $I_i$  is the current of the  $i$ 'th filament and  $\hat{h}$  is the current direction at  $\vec{r}$ . The position of the  $i$ 'th filament  $\vec{r}_h^{(i)}(\phi - \phi_{0,i})$ , depends on the toroidal angle  $\phi$  and the phase  $\phi_{0,i}$ , which is the toroidal angle for which the helix is at the midplane in the low field side. Since the filaments rotate with angular frequency  $\Omega$ , this phase differs for different time slices. The number of filaments, as described in Chapter 4, is determined by requiring a maximum drop in the fitting error for a small increase in the number of filaments. In the present situation three filaments gives us a considerable error minimization.

Now we need to determine the configuration of the currents that better reproduces the experimental measurements at the probes. For this, we define the parameters vector  $\vec{k} = \{I_1, I_2, I_3, \phi_{0,1}, \phi_{0,2}, \phi_{0,3}\}$  which involve the filaments current and phases, and must be determined simultaneously. As mentioned in Chapter 4 we use a Levenberg-Marquardt routine [Marquardt (1963)] to minimize the corresponding error functional (see Appendix B.1). The only difference here is that the model function must be adjusted for each measurement to account for the rotation of the helical currents.

$$\mathcal{E}(\vec{k}) = \sum_{n=1}^N \sum_{m=1}^M \left( \tilde{B}_z^{(m)}(t_n) - \delta B_z[\vec{k}, (\tilde{R}_m, \tilde{z}_m, \tilde{\phi}_m - \Omega t_n)] \right)^2. \quad (5.6)$$

Where  $\tilde{B}_z^{(m)}(t_n)$  is the poloidal field fluctuation measured by the  $m$ 'th magnetic probe located in  $\vec{r}_m = (\tilde{R}_m, \tilde{z}_m, \tilde{\phi}_m)$  for the time slice  $t_n$ , and  $\{N, M\}$  are the number of time slices and magnetic probes respectively. The simulated magnetic perturbation  $\delta B_z[\vec{k}, \vec{r}_m(t)]$  is calculated using our Biot-Savart calculator for the corresponding angles of each probe in the rotating frame, where  $\Omega = 2\pi \times 6.67$  Hz is the measured toroidal rotation frequency, and the adjusted time interval contains the heat measurements in Fig. 5.1. For a reasonable initial guess for the parameters the optimization routine converges to a minimum value of the error, where  $\{I_1, I_2, I_3\} = \{24.4, -17.2, -14.5\}$  kA and  $\{\phi_1, \phi_2, \phi_3\} = \{348.3^\circ, 70.2^\circ, 117.9^\circ\}$  (Fig. 5.3). The magnetic field pattern created by these filaments at the magnetic separatrix was depicted in the previous chapter in Fig. 4.4.

In Fig. 5.4 we show the comparison between the poloidal magnetic field measured by four magnetic probes at  $(R, z) = (2.4, 0.0)$  m in different toroidal positions, and the modeled field value from the helical currents using a Biot-Savart calculator. For the modeled portion of the shot between 2700 and 3000 ms the filament currents and their relative phases were kept constant in the rotating frame. Between 2400 and 2900 ms,

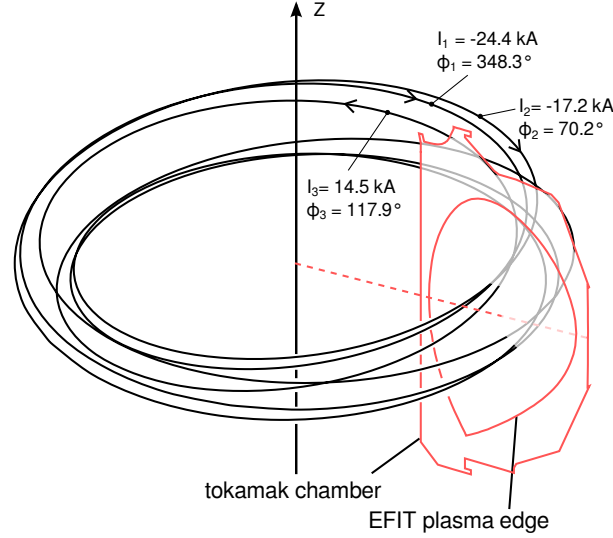


Figure 5.3: The error functional is well minimized by three internal helical filaments with  $q_h = 2$  at 40cm from the separatrix in the LFS mid-plane, rotating toroidally at the measured dominant frequency 6.67Hz.

the magnetic fluctuations have an approximately constant amplitude and frequency, but at the end of the heat flux measurements, after 2900 ms, the magnetic fluctuations are slightly increased.

After the parameter optimization, the filamentary currents account for the amplitude, phase, frequency and general shape of the magnetic oscillations in most of the magnetic probes signals, with some variations caused by small departures from a rigid rotation of the currents comprising the plasma response (Fig. 5.4).

The departure from rigid rotation of the internal currents may be due to the magnetic torque created by stationary magnetic fields produced internally and externally, but modeling the interaction of the stationary field with the model filaments is outside the scope of this work. Also, a simple addition of the static fields to the response field without interaction with the filaments will not affect the modeling of the magnetic signals because stationary fields only add a bias to the simulation of the measurement, without affecting the waveform. However, the addition of a stationary field for the manifold calculations can reshape the lobes in time causing measurable effects in the heat flux patterns, but this effect will only be observed if the stationary field plays a significant role in the definition of the non-axisymmetric field in the separatrix region.

In the discharge of interest the I and C-coils were operating during the heat measurement, causing possible departure from the rigid rotation in the manifolds. To estimate the importance of this external field  $\vec{B}_a^{(c)}$ , it was calculated in a uniform grid along the unperturbed separatrix and compared to the field created by the internal filaments  $\vec{B}_a^{(p)}$ .

In Fig. 5.5 we show the mean of the ratio  $|\vec{B}_a^{(c)}|/|\vec{B}_a^{(p)}|$  at the magnetic separatrix

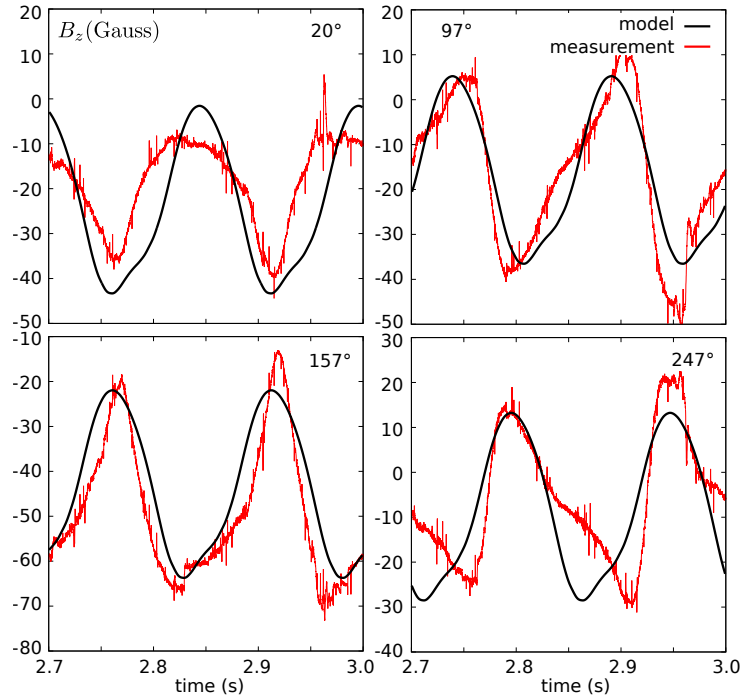


Figure 5.4: Comparison between the magnetic probe signals presented in the bottom of Fig. 5.1 (red), and the magnetic field created by the modeled rotating internal filaments at the probe locations (black). The comparison corresponds to the time interval containing the heat flux measurements. A reasonable match between maxima and minima is generally observed, while the waveform shape is not necessarily reproduced at some locations due to the approximation of rigid rotation.

as a function of the phase difference between helical filaments and the static array of coils. Clearly, the magnetic field from stationary sources would only modify the non-axisymmetric field in the separatrix region by less than 2%, while adding unnecessary complexity to the analysis of the manifolds in space and time. In the following, we disregard the stationary fields and consider the rigid rotating filaments as the only source of non-axisymmetry, which allows us to perform a simplified description of the non-axisymmetric field in the rotating frame and calculate the corresponding non-axisymmetric separatrix that expectedly delimits the time-dependent region of increased heat flux at the divertor targets.

### 5.2.1 Magnetic separatrix and footprints

Using the methods described in Appendix B.3, we were able to identify the intersection of the UPO with the plane  $\phi = 0$  for the equilibrium perturbed by the three filamentary currents in Fig. 5.6. The fixed point was located at  $(R_s, z_s) = (1.3931, -1.1023)$  m, at approximately 3.7 cm from the unperturbed saddle  $(R_s^0, z_s^0) = (1.3816, -1.0672)$  m, of the equilibrium reconstruction. Then we calculated the intersection of the invariant manifolds

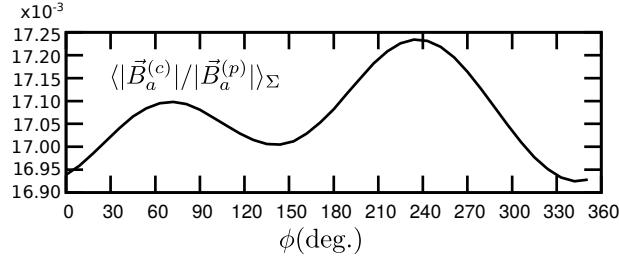


Figure 5.5: Magnetic surface mean of the ratio between the fields created by the external stationary currents and the internal helical currents at the magnetic separatrix for the DIII-D shot #158826 as a function of the rotation phase of the internal filaments.

with the poloidal plane at  $\phi = 0$  using the adaptive advection of elementary segments implemented in MAGMAN.

In Fig. 5.6, we show the cut of the invariant manifolds at  $\phi = 0$  in the rotating frame, where the helical filaments are stationary. The invariant manifolds develop the characteristic *homoclinic lobes* [Guckenheimer and Holmes (1983)] created by the magnetic perturbation on the invariant manifolds as they get stretched and folded to preserve the toroidal magnetic flux. The multiple intersections of the invariant manifolds lead to the proliferation of UPOs of higher periods by the *horseshoe mechanism* [Smale (1967)] which drives the chaotic behavior of the field lines at the plasma edge.

As we move toroidally in the rotating frame, (or as the time advances in the laboratory frame), the lobes move towards the UPO, and get stretched and folded. During the stretching, the invariant manifold crosses the tokamak wall in several regions that rotate toroidally in the laboratory frame. These crossings can be calculated with MAGMAN in the same way that the continuous poloidal section was calculated. The manifold cut at the tokamak chamber delimits the magnetic footprints or escape patterns and defines the internal boundaries through which there are abrupt changes in the connection lengths in a laminar plot [Wingen et al. (2009a)]. Provided that the parallel transport is dominant for the modeled discharge the interior of the manifold corresponds in a first approximation with the heat pattern. In magnetically diverted configurations the field lines intersect the divertor targets in static spiral regions in agreement with the experimental heat distribution for L-mode plasmas [Buttery et al. (1996); Schmitz et al. (2011)], and with the particle flux distribution for H-mode plasmas [Wingen et al. (2014)].

To compare the MAGMAN manifolds in the rotating frame with the heat deposition patterns measured at a fixed location in the laboratory we need to transform the times of the heat measurements to the corresponding toroidal phases of the rotating frame. This is achieved by

$$\phi'_i = \phi_c - \Omega(t_i - t_0), \quad (5.7)$$

where  $t_i$  is the time of the  $i$ 'th measurement,  $\phi_c$  is the toroidal phase of the IR camera,

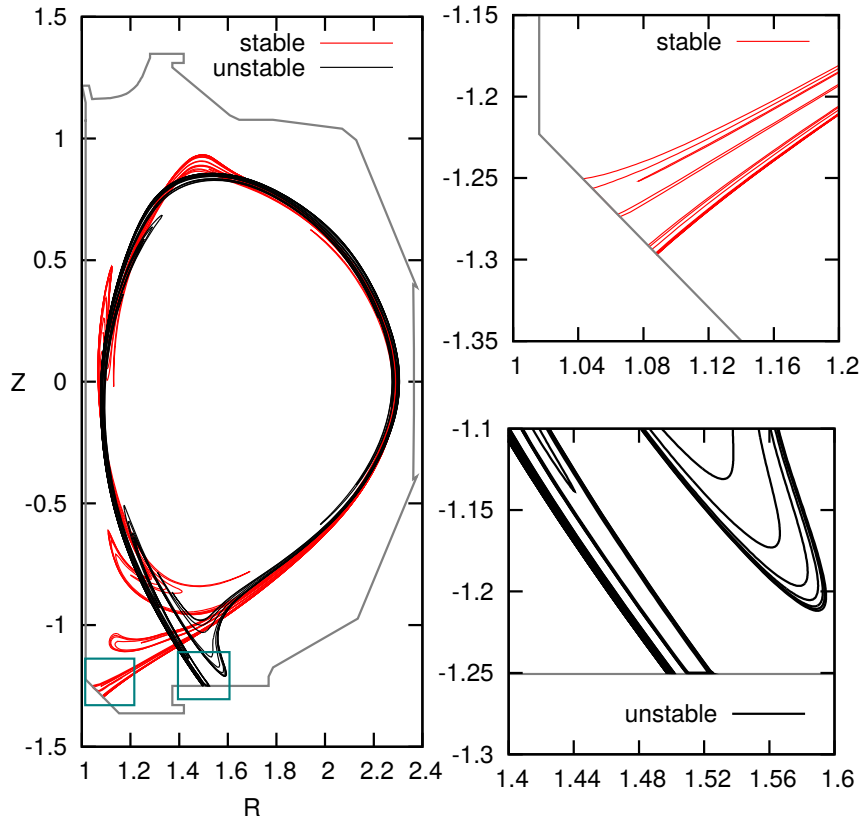


Figure 5.6: Cut of the invariant manifolds in the plane  $\phi = 0$ , for discharge #158826 subjected to the non-axisymmetric field created by the modeled helical filaments. The detail of the manifold intersection with the chamber reveals the layered interior of the magnetic footprints.

and  $\Omega = 2\pi \times 6.67$  Hz was determined from the waveforms captured by the magnetic probes. In Fig. 5.7 we depict the intersection of the unstable manifold with the chamber wall for the LFS strike region in the rotating frame. Overlapped on the manifold, we depict the experimental heat flux measurements introduced in Fig. 5.1 at the phases in the rotating frame corresponding to the time of each heat flux profile in the laboratory frame.

Notice that the heat flow peaks match reasonably well with the manifold interiors, and the observed peak splitting agrees well with the multiple interiors for each toroidal phase of the rotating frame. As discussed before, the invariant manifolds delimit the volume of confined field lines in non-axisymmetric situations. Consequently, the field lines inside the manifold can access the plasma interior driving the hot plasma by parallel transport to the Plasma Facing Components (PFC), while the field lines outside the manifold can not access the plasma and will only drive particles that leave the manifold interior by cross-field transport, which is small compared to the parallel transport.

For the region  $240^\circ < \phi < 360^\circ$ , the camera sees a single heat peak moving from 1.520 m to 1.525 m, which is well aligned with the clustered lobes, but as the lobes get

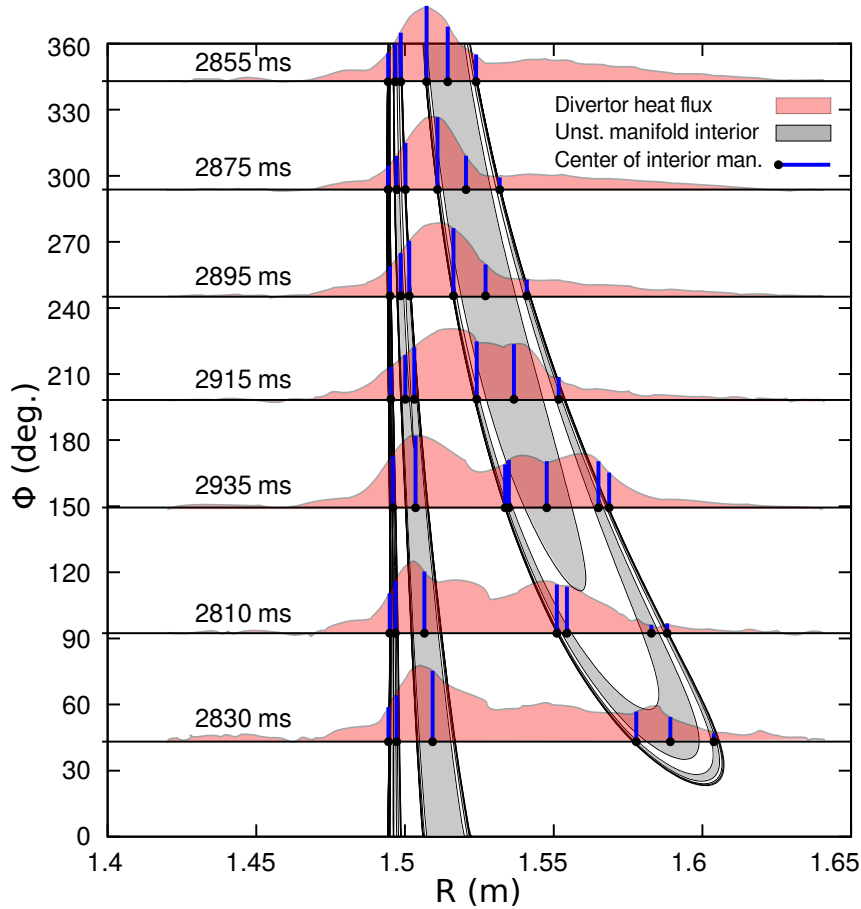


Figure 5.7: The interior of the unstable invariant manifold intersecting the DIII-D divertor plates in discharge #158826 in a rotating frame with toroidal frequency of 6.67 Hz (gray region), and an overlay of the experimental heat flux measurements for the corresponding toroidal phases of the rotating frame (profiles filled in light-red). The heat flux peaks are well correlated with the center of the manifold interior (blue lines) for most phases, and the secondary heat flux peak disappears where the lobes get too close radially to be resolved by the IR camera. The heat pattern evolves periodically, as expected if the manifold rotates rigidly.

separated the peak splits and the main peak moves to the HFS following another piece of the manifold with a smaller radial extension. Clearly, the heat load is not aligned with the axisymmetric strike line from EFIT at  $R \approx 1.5$  m but follows the wider lobes. This behavior explains the observed misalignment between the main flux peak and the strike point position from the axisymmetric reconstruction in Fig. 5.1. This measurement is consistent with the invariant manifold delimiting the region of enhanced heat flux in non-axisymmetric discharges and indicates that the heat flux may be concentrated in the lobes instead of the region where the manifold gets compressed near the unperturbed axisymmetric strike line.

It is important to point out that the calculation of the manifold interior is not intended to describe the heat flux profile, but to identify the regions of the chamber affected by

parallel transport. Heat flux profile features as intensity, width and peak locations require transport simulations that include particle drifts Wingen et al. (2014), but it is interesting to notice that the plasma edge calculation through invariant manifolds delimits well the radial extension of the heat load and approximates well the locations of the main peaks.

### 5.3 Chapter conclusions

In this chapter we have shown that the measured heat flux to the divertor plates of a single-null discharge evolves in agreement with the interior of a rotating invariant manifold calculated for a minimalist model of the plasma response field created by a rotating tearing instability. The non-axisymmetric field was calculated with a filamentary model of the source currents consisting of three helical wires with helicity  $q_h = 2$  located at 40cm from the separatrix in the mid-plane. The model parameters were adjusted to reproduce the measured magnetic signals at several probes outside the plasma. A more sophisticated treatment involving multiple helicities, several surfaces and more filamentary currents can provide more details of the heat patterns and the topological changes experienced by the manifolds, but in terms of experimental observations a simple model with reasonable properties gives a good quantitative match, suggesting that the extension and overall shape of the heat pattern is mainly controlled by the size and wave numbers of the magnetic perturbations at the plasma edge. The study of the interplay between the magnetic topology and the heat flow provides a relevant insight on the nature of the helical structures developing at the plasma edge. Whenever the parallel transport is dominant we can describe important features of real discharges using simple effective models like the one presented here.

The identification of the invariant manifolds with the plasma edge brings interesting possibilities for the interpretation and modeling of plasma structures near the plasma-vacuum interface and the evolution of the heat loads on the chamber components. These structures may emerge from parallel transport along the field lines resulting from the overlapping of dynamic and stationary magnetic fields in the presence of a magnetic saddle. This general situation may be relevant during the ELM suppression by resonant magnetic perturbations where a non-stationary magnetic perturbation caused by evolving currents in the plasma is combined with an externally applied magnetic perturbation. Also, the so-called filamentary structures may be a manifestation of time-dependent helical features developing at the invariant manifolds Eich et al. (2003), but this may require more detailed modeling of the non-axisymmetric source currents.



# Chapter 6

## Conclusions and perspectives

In this work we have demonstrated the viability of simple models to describe the self-consistent magnetic field in tokamak devices. For the axisymmetric situation we have implemented a specific choice of the pressure and poloidal current dependences on the poloidal magnetic flux that allowed us to solve analytically the equilibrium problem. The Grad-Shafranov equation became an eigenvalue problem so that the magnetic flux is a linear superposition of a family of orthogonal solutions. To implement the solution we developed the numerical routine `DISFUNSOL` that uses analytical functions with adjustable parameters to describe the plasma parameters measured during a tokamak discharge and the necessary boundary conditions. Our results were compared with the equilibrium reconstruction of `EFIT` obtaining a reasonable match between the plasma profiles and magnetic topology. For the non-axisymmetric situation we introduced a generic description of the non-axisymmetric currents in the plasma and external coils, then we introduced an efficient method for calculating the resultant non-axisymmetric magnetic field and implemented it in the library `magnetic_field.h`. These methods were then used to describe the non-axisymmetric vacuum fields from the C and I-coils of the DIII-D tokamak. In addition to this, the magnetic field created by the plasma response was modeled by adjusting the currents and phases of a prescribed number of internal helical currents. The helices carrying the current were designed to have the same topology of the magnetic field lines at the rational magnetic surface where the instability develops. The instability surface was identified by locating the phase inversion surface of the electron cyclotron emission signals. The numerical routine `adjust_helices.c` was developed for this task and resulted in a set of helical filaments that reproduce the external magnetic measurements and provide sources to calculate the magnetic field in the separatrix region. With the magnetic field from the axisymmetric plasma, the external coils and the non-axisymmetric plasma currents, it was possible to model the complete magnetic field everywhere in the separatrix region and determine the separatrix structure by means of

an invariant manifolds calculation. For this part of the work we developed the MAGMAN routine, that implements an advective, adaptive calculation of the invariant manifolds based on the magnetic field values, resulting in a continuous surface delimiting the internal field lines in a divertor discharge. This work was concluded with the application of all the methods in a particular DIII-D discharge presenting interesting features of the plasma-wall interaction. In discharge #158826 a slowly rotating tearing mode develops and at the same time the heat patterns in the divertor tiles evolve, presenting a periodic proliferation of heat-flux peaks. It was determined that the magnetic oscillations and the heat bifurcation period were approximately equal, so that a rotating invariant manifold created by the internal instability was proposed. The magnetic field from the internal currents was modeled using a rigid rotating filamentary description of the plasma response and the invariant manifolds were calculated with MAGMAN and intersected with the divertor tiles region. After the calculations it was observed a clear correspondence between the phase, extension and number of peaks between the magnetic footprints of the rotating manifold and the evolving heat flux patterns in the divertor region. This interesting result links the development of coherent structures in the plasma edge with the magnetic contribution from internal instabilities, and may represent a significant step towards self-consistency from a simplified description of the magnetic field and its sources.

From this point, the developed methods can be enhanced by considering various magnetic helicities and a non-rigid filamentary description that allow us to describe more precisely the response magnetic field and the resulting invariant manifolds. In this situation the invariant manifold would be an evolving three-dimensional surface instead of a rigid one, and this can lead to interesting dynamical aspects not studied before in the context of fusion plasmas. In addition to this, the filamentary description of the plasma response can be used to understand better the deleterious mode locking that leads to disruptions in tokamaks and can be a considerable threat to the integrity of larger fusion reactors.

# Appendices



# Appendix A

## Useful derivations

### A.1 The Euler-Lagrange Equations

Consider a functional of the form

$$J = \int_1^2 f(y_i, \dot{y}_i, t) dt \quad (\text{A.1})$$

where the integral takes place along a path  $\{y_i(x), \dot{y}_i(x)\}$  in the configuration space  $(\vec{y}, \dot{\vec{y}})$  between the points 1 and 2 and the curve is parametrized by  $x$ . The problem here is to find the trajectory that extremizes the functional  $J$  between the points 1 and 2, i.e. such that  $\delta J$  vanishes.

Considering that the limits 1 and 2 in the configuration space are fixed, then the variation takes the form

$$\delta J = \int_1^2 \left[ \frac{\partial f}{\partial y_i} \delta y_i + \frac{\partial f}{\partial \dot{y}_i} \delta \dot{y}_i \right] dt = 0, \quad (\text{A.2})$$

where repeated indexes indicate summation. An orbit  $y_i(t, \lambda)$  that is close to the solution  $y_i^0(t)$  can be written as

$$y_i(t, \lambda) = y_i^0(t) + \lambda \eta_i(t) \quad (\text{A.3})$$

such that  $\eta_i(t_1) = \eta_i(t_2) = 0$ . In this representation it is clear that  $\delta y_i = (\partial y_i / \partial \lambda) \delta \lambda = \eta_i(t) \delta \lambda$ . From this, it is also clear that

$$\delta \dot{y}_i = \frac{d}{dt} \delta y_i. \quad (\text{A.4})$$

Replacing this into (A.2) and using the chain rule we can write

$$\int_1^2 \left[ \frac{\partial f}{\partial y_i} - \frac{d}{dt} \frac{\partial f}{\partial \dot{y}_i} \right] \delta y_i dt + \left[ \frac{\partial f}{\partial \dot{y}_i} \delta y_i \right]_1^2 = 0. \quad (\text{A.5})$$

Since the functions  $\delta y_i(t)$  are arbitrary and vanish at the boundaries, the integrand must vanish independently, leading to

$$\frac{\partial f}{\partial y_i} - \frac{d}{dt} \frac{\partial f}{\partial \dot{y}_i} = 0. \quad (\text{A.6})$$

Solving these equations for all  $i$  give us the required trajectory  $y_i(t)$  between the end-points.

## A.2 Evolution of a surface function

Assume that there is an integral quantity  $G(\Omega)$  dependent on the volume and shape of a given region  $\Omega(t)$ , delimited by the surface  $\Sigma(t)$  (see Fig. A.1).

$$G(\Omega, t) = \int_{\Omega(t)} g(\vec{r}, t) d^3\vec{r}. \quad (\text{A.7})$$

Here,  $\Omega(t)$  is the volume enclosed by some connected surface  $\Sigma$  at the time  $t$ . The time evolution of  $G$  for a given magnetic surface depends on the evolution of the surface itself.

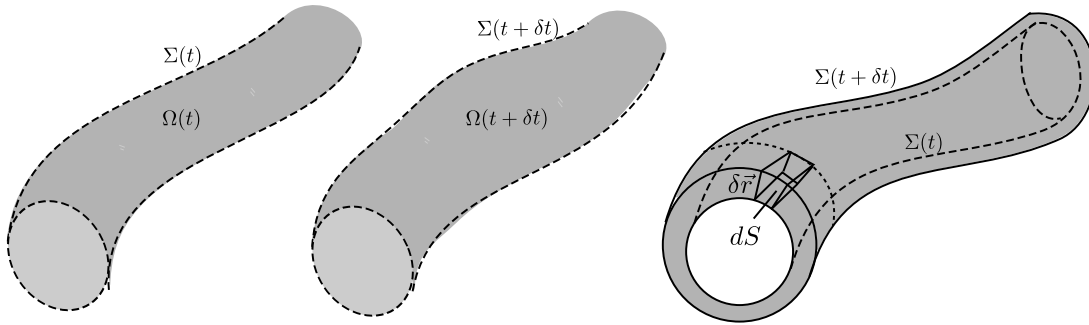


Figure A.1: Evolution of an integration volume in time.

After a short time  $\delta t$  the surface defining the integral moves, and  $G$  becomes to a first order in  $\delta t$

$$G(\Omega, t + \delta t) = \int_{\Omega(t + \delta t)} g(\vec{r}, t + \delta t) d^3\vec{r} = \int_{\Omega(t)} \left[ g(\vec{r}, t) + \frac{\partial g(\vec{r}, t)}{\partial t} \delta t \right] d^3\vec{r} + \int_{\delta\Omega} g(\vec{r}, t) d^3\vec{r}, \quad (\text{A.8})$$

where  $\delta\Omega$  is the volume between the surfaces  $\Sigma(t + \delta t)$  and  $\Sigma(t)$  that delimit  $\Omega(t + \delta t)$  and

$\Omega(t)$  respectively. Also, we dropped the  $\delta t$  term on the last integral, since it will lead to a superior order term that vanishes for arbitrarily small variations. For the last integral, the volume element may be written as  $d^3\vec{r} = d\vec{S} \cdot \delta\vec{r}$ , with  $\delta\vec{r}$  the displacement of the magnetic surface after  $\delta t$ . Without restricting ourselves to ideal MHD, we consider an arbitrary velocity for the displacement of the magnetic surface, i.e  $\delta\vec{r} = \vec{v}_\sigma \delta t$ . For small  $\delta t$ , the difference between (A.8) and (A.7) divided by the time interval gives

$$\frac{\delta G(\Omega, t)}{\delta t} = \frac{dG(\Omega, t)}{dt} = \int_{\Omega(t)} \frac{\partial g(\vec{r}, t)}{\partial t} d^3\vec{r} + \oint_{\Sigma(t)} g(\vec{r}, t) \vec{v}_\sigma \cdot d\vec{S}, \quad (\text{A.9})$$

where the last term appears as a contribution due to the displacement of the integration boundary and vanishes for  $\vec{v}_\sigma = 0$ .

### A.3 Evolution of the magnetic helicity

In the following lines it will be shown that the evolution of the magnetic helicity is related to the plasma conductivity and the relative velocity between the plasma flow velocity and the magnetic surface velocity. The magnetic helicity  $\Lambda$ , in a given volume  $\Omega$ , is defined as

$$\Lambda(\Omega) = \int_{\Omega} (\vec{B} \cdot \vec{A}) d^3\vec{r}. \quad (\text{A.10})$$

If we want  $\Lambda(\Omega)$  to be a physical quantity, then it must be invariant under the gauge change  $\vec{A} + \nabla\chi$ , that requires

$$\int_{\Omega} (\vec{B} \cdot \nabla\chi) d^3\vec{r} = \int_{\Omega} \nabla \cdot (\chi\vec{B}) d^3\vec{r} = \oint_{\Sigma} \chi\vec{B} \cdot d\vec{S} = 0. \quad (\text{A.11})$$

The last integral vanishes for arbitrary  $\chi(\vec{r}, t)$  only if  $\vec{B} \cdot d\vec{S} = 0$ . In other words, the magnetic helicity is a physical quantity only if the volume is enclosed by some magnetic surface, this means that  $\Lambda(\Omega)$  is a surface quantity. Interestingly, the fact that the bounding surface must be a magnetic surface was demonstrated in the body of the text when developing the concept of magnetic helicity from that of linking number.

If the magnetic surface evolves in time, its bounded volume changes and we have

$$\Lambda(\Omega, t) = \int_{\Omega(t)} (\vec{B} \cdot \vec{A}) d^3\vec{r}. \quad (\text{A.12})$$

To calculate the change of  $\Lambda$  we need to use (A.9)

$$\frac{d\Lambda}{dt} = \int_{\Omega(t)} \frac{\partial}{\partial t} (\vec{B} \cdot \vec{A}) d^3\vec{r} + \oint_{\Sigma(t)} (\vec{B} \cdot \vec{A}) \vec{v}_\sigma \cdot d\vec{S} \quad (\text{A.13})$$

From the Faraday's law  $\frac{\partial}{\partial t} \vec{B} = -\nabla \times \vec{E}$  and  $\vec{B} = \nabla \times \vec{A}$  we have

$$\frac{\partial}{\partial t} \vec{A} = -\vec{E} + \nabla \xi, \quad (\text{A.14})$$

where  $\xi$  is another arbitrary gauge function. Now, we can use the single-fluid MHD equations to write the electric field in terms of the plasma current density and velocity. The Ohm's law reads

$$\vec{j} = \sigma(\vec{E} + \vec{v} \times \vec{B}) = \frac{1}{\mu_0} \nabla \times \vec{B}, \quad (\text{A.15})$$

with  $\sigma$  the plasma conductivity. This leads to  $\vec{E} = \sigma^{-1} \vec{j} - \vec{v} \times \vec{B}$ , and we can insert this in (A.14)

$$\frac{\partial}{\partial t} \vec{A} = \vec{v} \times \vec{B} - \sigma^{-1} \vec{j} + \nabla \chi. \quad (\text{A.16})$$

The integrand in the volume integral of (A.13) changes in a fixed spatial position as  $\frac{\partial}{\partial t} (\vec{A} \cdot \vec{B}) = \vec{A} \cdot \frac{\partial}{\partial t} \vec{B} + \vec{B} \cdot \frac{\partial}{\partial t} \vec{A}$ . The first term may be written

$$\vec{A} \cdot \frac{\partial}{\partial t} \vec{B} = \vec{A} \cdot \nabla \times \frac{\partial}{\partial t} \vec{A} = \vec{B} \cdot \frac{\partial}{\partial t} \vec{A} - \nabla \cdot (\vec{A} \times \frac{\partial}{\partial t} \vec{A}), \quad (\text{A.17})$$

so, adding the second term leads to

$$\frac{\partial}{\partial t} (\vec{A} \cdot \vec{B}) = 2\vec{B} \cdot \frac{\partial}{\partial t} \vec{A} - \nabla \cdot (\vec{A} \times \frac{\partial}{\partial t} \vec{A}). \quad (\text{A.18})$$

Using (A.16) we obtain

$$\vec{B} \cdot \frac{\partial}{\partial t} \vec{A} = \nabla \xi \cdot \vec{B} - \sigma^{-1} \vec{B} \cdot \vec{j}. \quad (\text{A.19})$$

Using  $\nabla \cdot \vec{B} = 0$  we can put everything together to get

$$\frac{\partial}{\partial t} (\vec{A} \cdot \vec{B}) = -2\sigma^{-1} \vec{B} \cdot \vec{j} + \nabla \cdot (2\xi \vec{B} - \vec{A} \times \frac{\partial}{\partial t} \vec{A}). \quad (\text{A.20})$$

Now we can integrate this in a volume bounded by a magnetic surface and transform the last term into a surface integral, where obviously  $\vec{B} \cdot d\vec{S} = 0$ . Then we obtain

$$\int_{\Omega} \frac{\partial}{\partial t} (\vec{A} \cdot \vec{B}) d^3\vec{r} = -\frac{2}{\sigma} \int_{\Omega(t)} (\vec{j} \cdot \vec{B}) d^3\vec{r} - \oint_{\Sigma(t)} \left( \vec{A} \times \frac{\partial}{\partial t} \vec{A} \right) \cdot d\vec{S}. \quad (\text{A.21})$$

Using again (A.16) and writing only the non-vanishing terms we get:

$$\int_{\Omega(t)} \frac{\partial}{\partial t} (\vec{B} \cdot \vec{A}) d^3\vec{r} = -\frac{2}{\sigma} \int_{\Omega(t)} (\vec{j} \cdot \vec{B}) d^3\vec{r} - \oint_{\Sigma(t)} (\vec{A} \cdot \vec{B}) \vec{v} \cdot d\vec{S}. \quad (\text{A.22})$$

Replacing (A.22) in (A.13) we obtain the change in the magnetic helicity

$$\frac{d}{dt}\Lambda(\Omega, t) = -\frac{2}{\sigma} \int_{\Omega(t)} (\vec{j} \cdot \vec{B}) d^3\vec{r} + \oint_{\Sigma(t)} (\vec{A} \cdot \vec{B})(\vec{v} - \vec{v}_\Sigma) \cdot d\vec{S}, \quad (\text{A.23})$$

where  $\vec{v}_\Sigma$  is the velocity of the magnetic surface and  $\vec{v}$  is the plasma flow velocity. This equation is valid for general non-ideal MHD, however the information about the surface displacement becomes an issue, since the labeling may not be preserved due to reconnection and the velocity must be written in terms of non-local conditions.

## A.4 Magnetic field frozen into the plasma

One of the fundamental properties of a perfectly conducting plasma is that the magnetic field lines are attached to the fluid and follow its motion. To demonstrate this we first assume that the magnetic lines are labeled by corresponding flux surfaces. Then we consider a plane that cuts some portion of the magnetic surfaces transversely and we will follow the evolution of the magnetic surface labeled by  $\psi$  through the curve  $\Gamma(t)$  defined on the intersection and enclosing a region  $\sigma(t)$  of the plane.

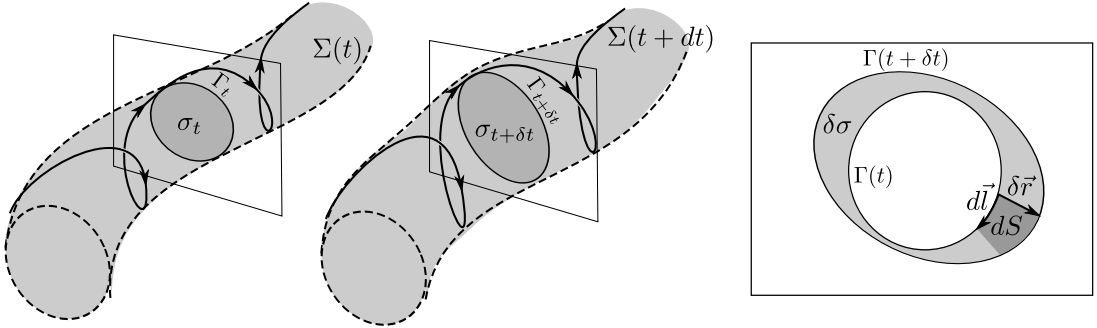


Figure A.2: Evolution of a magnetic surface in time.

The curve  $\Gamma(t)$  evolves in time according to the modifications in the magnetic surface labeled by the flux  $\psi$  that must be maintained constant.

$$\psi = \int_{\sigma(t)} \vec{B}(\vec{r}, t) \cdot d\vec{S} \quad (\text{A.24})$$

As we are interested in following a given magnetic surface its flux label must not change and we can write

$$\int_{\sigma(t+\delta t)} \vec{B}(\vec{r}, t + \delta t) \cdot d\vec{S} - \int_{\sigma(t)} \vec{B}(\vec{r}, t) \cdot d\vec{S} = 0, \quad (\text{A.25})$$

where the first surface integral may be written like (see Fig.A.2)

$$\int_{\sigma(t+\delta t)} \vec{B}(\vec{r}, t + \delta t) \cdot d\vec{S} = \int_{\sigma(t)} \vec{B}(\vec{r}, t + \delta t) \cdot d\vec{S} + \int_{\delta\sigma} \vec{B}(\vec{r}, t) \cdot d\vec{S} \quad (\text{A.26})$$

The last surface integral is defined in the region between  $\Sigma(t)$  and  $\Sigma(t + \delta t)$ . Clearly the element of area in  $\delta\Sigma$  can be written as  $d\vec{S} = d\vec{l} \times \delta\vec{r}$ , where  $\delta\vec{r}$  is the displacement vector of the circuit  $\Gamma(t + \delta t)$  on the cutting plane from its original position in  $\Gamma(t)$  and  $d\vec{l}$  is the line element on the time  $t$ . With this, the last surface integral in (A.26) may be written as a line integral

$$\int_{\sigma(t+\delta t)} \vec{B}(\vec{r}, t + \delta t) \cdot d\vec{A} = \int_{\sigma(t)} \vec{B}(\vec{r}, t + \delta t) \cdot d\vec{S} + \oint_{\Gamma(t)} \vec{B}(\vec{r}, t) \cdot (\delta\vec{r} \times d\vec{l}). \quad (\text{A.27})$$

Now, we can replace (A.27) in (A.25) and take the limit of small  $\delta t$  to obtain

$$\int_{\sigma(t)} \delta t \frac{\partial}{\partial t} \vec{B}(\vec{r}, t) \cdot d\vec{S} + \oint_{\Gamma(t)} \vec{B}(\vec{r}, t) \cdot (\delta\vec{r} \times d\vec{l}) = 0. \quad (\text{A.28})$$

To conclude this demonstration, let us consider an ideal MHD plasma. In this limit,  $\vec{E} = -\vec{v} \times \vec{B}$ , leading to  $\frac{\partial}{\partial t} \vec{B} = \nabla \times (\vec{v} \times \vec{B})$ . Replacing this into (A.28) and using the Stokes theorem we get

$$\oint_{\Gamma(t)} \left( \vec{v} - \frac{\delta\vec{r}}{\delta t} \right) \times \vec{B} \cdot d\vec{l} = 0, \quad (\text{A.29})$$

which we can reorder to obtain

$$\oint_{\Gamma(t)} (\vec{B} \times d\vec{l}) \cdot (\vec{v} - \vec{v}_\Sigma) = 0, \quad (\text{A.30})$$

where we define the magnetic surface velocity  $\vec{v}_\Sigma = \frac{\delta\vec{r}}{\delta t}$ . Notice that this equation is valid for any magnetic surface and the cutting plane can be chosen arbitrarily, then, the integrand vanishes identically and the displacement of the magnetic surfaces must satisfy  $(\frac{\delta\vec{r}}{\delta t} - \vec{v}) \cdot \hat{n} = 0$ , where  $\hat{n}$  is the normal vector to the surface, indicating that the normal displacement of the magnetic surfaces and the normal fluid motion occur at the same rate, and can be only detached through the plasma resistivity.

## A.5 Magnetic field from a finite segment

Provided that a sequence of straight segments describe a closed path, we can find a generic equation for the magnetic field contribution of each element, when a current  $I$  is passed through it. Without loss of generality we can use a convenient reference frame for an

arbitrary segment (Fig. A.3).

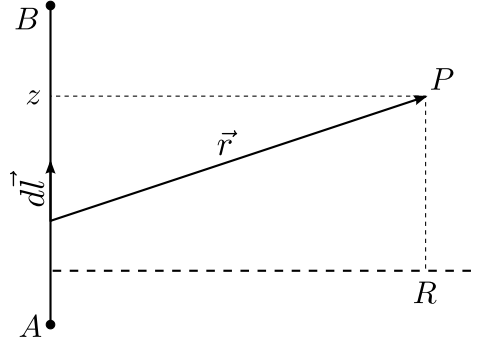


Figure A.3: Integration segment

The magnetic field contribution from the current passing from  $A$  to  $B$  can be found using the Biot-Savart integral with open ends, so that the magnetic field is only meaningful when all the elements were accounted for and the path closes

$$\vec{B}_{AB}(\vec{r}) = \frac{\mu_0 I \hat{\phi}}{4\pi} \int_A^B \frac{r \sin \theta dz'}{r^3} = \frac{\mu_0 I R \hat{\phi}}{4\pi} \int_A^B \frac{dz'}{[(z - z')^2 + R^2]^{3/2}}, \quad (\text{A.31})$$

where  $r = |\vec{r}|$ , and  $\hat{\phi}$  is the unit vector orthogonal to the plane containing  $ABP$ . After solving this elementary integral we obtain

$$\vec{B}_{AB}(\vec{r}) = \frac{\mu_0 I}{4\pi R} \left( \frac{z + L/2}{\sqrt{R^2 + (z + L/2)^2}} - \frac{z - L/2}{\sqrt{R^2 + (z - L/2)^2}} \right) \hat{\phi}_i. \quad (\text{A.32})$$

This result can be written terms of the vectors joining the points  $A, B$  and  $P$ .

$$\vec{B}_i = \frac{\mu_0 I}{4\pi R} \left( \frac{\vec{AP}}{|\vec{AP}|} - \frac{\vec{BP}}{|\vec{BP}|} \right) \cdot \frac{\vec{AB}}{|\vec{AB}|} \hat{\phi}. \quad (\text{A.33})$$

where the normal vector  $\hat{\phi}$  can be obtained from the previous vectors by elementary operations

$$\hat{\phi} = \frac{\vec{PA} \times \vec{PB}}{|\vec{PA} \times \vec{PB}|}, \quad (\text{A.34})$$

To complete the calculation we need to write  $R$  in terms of  $A, B$  and  $P$  in the equation of the magnetic field. Using the equation for the area of the triangle  $ABP$  it can be shown that

$$R = \frac{|\vec{PA} \times \vec{PB}|}{|\vec{AB}|}. \quad (\text{A.35})$$

With this, the magnetic field created by the wire element  $\overrightarrow{AB}$  at the point  $P$  is

$$\vec{B}_{AB} = \frac{\mu_0 I}{4\pi} \left[ \left( \frac{\overrightarrow{PB}}{|PB|} - \frac{\overrightarrow{PA}}{|PA|} \right) \cdot \overrightarrow{AB} \right] \frac{\overrightarrow{PA} \times \overrightarrow{PB}}{|\overrightarrow{PA} \times \overrightarrow{PB}|^2}. \quad (\text{A.36})$$

Using  $\overrightarrow{AB} = \overrightarrow{PB} - \overrightarrow{PA}$  it can be shown that

$$\vec{B}_{AB}(P) = \frac{\mu_0 I}{4\pi} \frac{|PA|^{-1} + |PB|^{-1}}{|PA||PB| + \overrightarrow{PA} \cdot \overrightarrow{PB}} \overrightarrow{PA} \times \overrightarrow{PB}. \quad (\text{A.37})$$

Notice that this result is independent of the original choice of the coordinate system and can be used for any arbitrary orientation and position of the segment  $AB$  respect to  $P$ .

# Appendix B

## Numerical methods

### B.1 Levenberg-Marquardt optimization

In this appendix we present the general form of a damped least squares method, useful for fitting functions depending non-linearly on a given set  $\vec{k} = \{k_1, k_2, \dots, k_N\}$ , of optimization parameters [Marquardt (1963)]. Start considering the error functional

$$\varepsilon(\vec{k}) = \sum_{i=1}^m (y_i - f(x_i, \vec{k}))^2, \quad (\text{B.1})$$

Where the  $y_i$  are the known values of some unknown function at the points  $x_i$  and  $f$  is a function we use to mimic those values at those positions. The vector  $\vec{k}$  contains all the parameters that control the model function.

To minimize the functional we need to perform a small variation in the parameters such that  $\varepsilon(\vec{k} + \delta\vec{k}) < \varepsilon(\vec{k})$ . This can be achieved by solving the linear problem

$$(J^T J + \lambda \text{diag}(J^T J)) \delta\vec{k} = J^T (\vec{y} - \vec{f}(\vec{k})), \quad (\text{B.2})$$

with  $\vec{y} = (y_1, y_2, \dots, y_m)^T$ ,  $\vec{f}(\vec{k}) = (f(x_1, \vec{k}), f(x_2, \vec{k}), \dots, f(x_m, \vec{k}))^T$  and  $J$  the Jacobian matrix of the system. The diagonal of the product  $J^T J$  introduces a weighted damping on the direction of each variable, while increasing the step size in directions that lead to little variations in the error. Explicitly, the linear problem can be written

$$\left( \frac{\partial f_i}{\partial k_j} \frac{\partial f_i}{\partial k_n} - \lambda \delta_{j,n} \frac{\partial f_i}{\partial k_j} \frac{\partial f_i}{\partial k_n} \right) \delta k_n = \frac{\partial f_i}{\partial k_j} (y_i - f_i), \forall j \quad (\text{B.3})$$

The damping factor  $\lambda$  is a positive number that can be adjusted dynamically to take larger steps when we are far from the desired parameters and more refined variations when we are closer to the minimum. To do this we can calculate  $\varepsilon(\lambda)$  and  $\varepsilon(r\lambda)$  with

$0 < r < 1$ . at each iteration. Then we redefine  $\lambda$  to be the one that provided the largest error reduction. If we do not get any error reduction we do not apply the parametric variation, redefine  $\lambda \rightarrow \lambda/r$  and repeat the step. The iterative process is stopped when the functional falls below some predefined *small* tolerance value.

## B.2 Numerical integration routine

One of the issues that deserved attention in this work was the implementation of efficient and accurate numerical integrators, since the built-in methods of softwares like *Mathematica* and *Matlab* presented some unexpected features, like numerical dissipation larger than the reported in the documentation and ineffective error control features that lead to long-term instability.

Consequently, the numerical integrators were written from scratch in C language. A generic explicit Runge-Kutta method with adaptive step-size was implemented as an independent C module named `field_tracer.h`. The developed module implements the Butcher Tableaux [Butcher (2008)] for the Fehlberg [Fehlberg (1969)], Kash-Karp [Cash and Karp (1990)], Dormand Prince [Dormand and Prince (1980)] and the classical RK4 integration methods. In this way we were able to compare the performance of each one for the same axisymmetric equilibrium reconstruction. Notice also that the default integrator used by General Atomics in the code TRIP3D is a RK4 with back-step error estimation [Evans et al. (2002)].

To measure the integrators performance we integrate a field line for several toroidal cycles and calculate the poloidal magnetic flux at the points composing the orbit. In the axisymmetric case, the flux must be a constant, since the associated Hamiltonian system is integrable and the field line must be attached to a single magnetic surface. In this way, the departure from constancy is a good indicator of the integrator performance.

In Fig. B.1 we compare the variations in the poloidal flux for all the integrators in such a way that all of them take approximately the same number of steps. In other words, the fixed step-size of the RK4 was chosen after knowing the number of steps required by the adaptive integrators. Additionally, the tolerance of the variable step-size methods was set to the same value, leading to similar number of steps. Clearly, the classical, fixed step RK4 method shows a poor performance compared to any of the variable step methods.

The Cash-Karp method, with order five, showed the best performance with an intermediate computational time, faster than the Fehlberg (order five) and slower than the Dormand-Prince (order five with six evaluation steps). Also, the Cash-Karp method takes about twice the time of the RK4 method due to the comparison stage, where two different approximations of the following point in the orbit are used to estimate the error and to

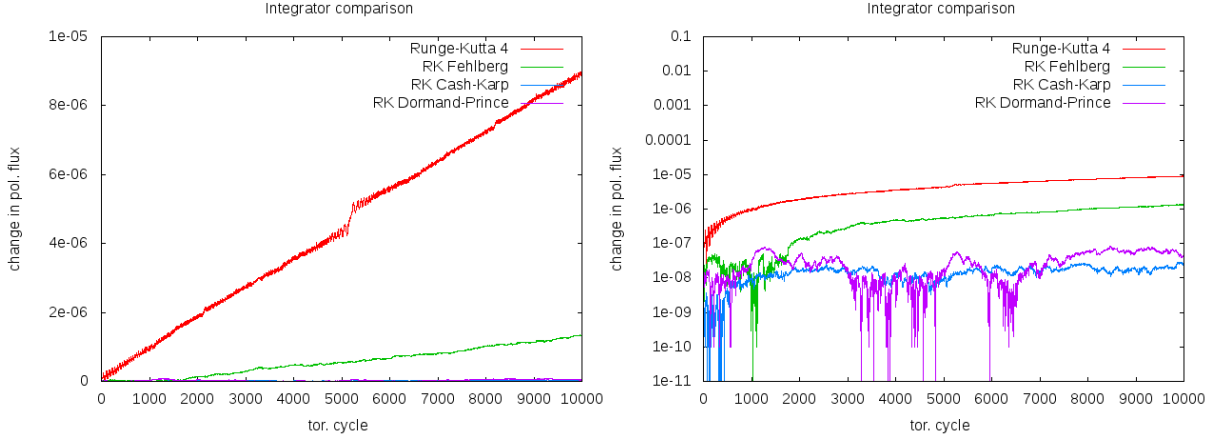


Figure B.1: Change in the poloidal magnetic flux for a field line integrated for  $10^4$  toroidal cycles with the four numerical integrators implemented in `field_tracer.h`. In the left we depict the curves in a linear scale and in the right in a logarithmic scale to fully appreciate the details of the fluctuations for the integrators that perform better.

modify the step-size. Clearly, doubling the computational time is a good choice when the magnetic flux fluctuations are reduced by three orders of magnitude, specially if we are dealing with a conservative (divergence-free) vector field. Consequently, the Cash-Karp integrator is the default choice for all the subsequent calculations. In general, we want to solve an equation of the form

$$\frac{dy}{dt} = f(y, t), \quad (\text{B.4})$$

for the initial conditions  $(y_0, t_0)$ . The numerical solution consists in finding a discretization  $y_n = y(t_n)$  for a sequence  $\{t_1, t_2, \dots\}$ . For any explicit Runge-Kutta integrator the dynamical system position at the time  $t_{n+1}$  is given by

$$y_{n+1} = y_n + h \sum_{i=1}^s b_i k_i, \quad (\text{B.5})$$

where  $t_{n+1} = t_n + h$ , and

$$\begin{aligned} k_1 &= f(t_n, y_n), \\ k_2 &= f(t_n + c_2 h, y_n + h(a_{21} k_1)), \\ k_3 &= f(t_n + c_3 h, y_n + h(a_{31} k_1 + a_{32} k_2)), \\ &\vdots \\ k_s &= f(t_n + c_s h, y_n + h(a_{s1} k_1 + a_{s2} k_2 + \dots + a_{s,s-1} k_{s-1})). \end{aligned} \quad (\text{B.6})$$

The relevant parameters of the integration method are usually defined in a Butcher tableau

[Butcher (2008)], with the form:

$$\begin{array}{c|cccc}
 0 & & & & \\
 c_2 & a_{21} & & & \\
 c_3 & a_{31} & a_{32} & & \\
 \vdots & & \ddots & & \\
 c_s & a_{s1} & a_{s2} & \dots & a_{ss-1} \\
 \hline
 & b_1 & b_2 & \dots & b_{s-1} & b_s
 \end{array} \tag{B.7}$$

where the  $c$ 's can be obtained by adding up horizontally the array values

$$c_i = \sum_{j=1}^{i-1} a_{ij}. \tag{B.8}$$

In the case of the Cash-Karp method, the Butcher tableau is given by

$$\begin{array}{c|cccccc}
 0 & & & & & \\
 \frac{1}{5} & \frac{1}{5} & & & & \\
 \frac{3}{10} & \frac{3}{40} & \frac{9}{40} & & & \\
 \frac{3}{5} & \frac{3}{10} & -\frac{9}{10} & \frac{6}{5} & & \\
 1 & -\frac{11}{54} & \frac{5}{2} & -\frac{70}{27} & \frac{35}{27} & \\
 \frac{7}{8} & \frac{1631}{55296} & \frac{175}{512} & \frac{575}{13824} & \frac{44275}{110592} & \frac{253}{4096} \\
 \hline
 & \frac{37}{378} & 0 & \frac{250}{621} & \frac{125}{594} & 0 & \frac{512}{1771} \\
 & \frac{2825}{27648} & 0 & \frac{18575}{48384} & \frac{13525}{55296} & \frac{277}{14336} & \frac{1}{4}
 \end{array} \tag{B.9}$$

where the first row of  $b$ 's give us a fourth order solution for  $y_{n+1}$ , while the last row a fifth order one. Having two solutions is useful to estimate the error of the step performed, and this can be used to perform a step control to maintain the error below some predefined value.

In Fig. B.2 we show the Poincaré section calculated through the Cash-Karp method for several initial conditions in both regular and chaotic regions. The remaining toroidal surfaces and the new invariants created by the perturbation (magnetic islands) are well preserved by the numerical integrator, i.e. they maintain a continuous appearance, which is not the case when there is numerical dissipation caused by the integration method.

### B.3 Invariant manifolds calculation

The first step to calculate the invariant manifolds is the determination of the Unstable Periodic Orbit (UPO), or saddle orbit, which is the three-dimensional generalization of

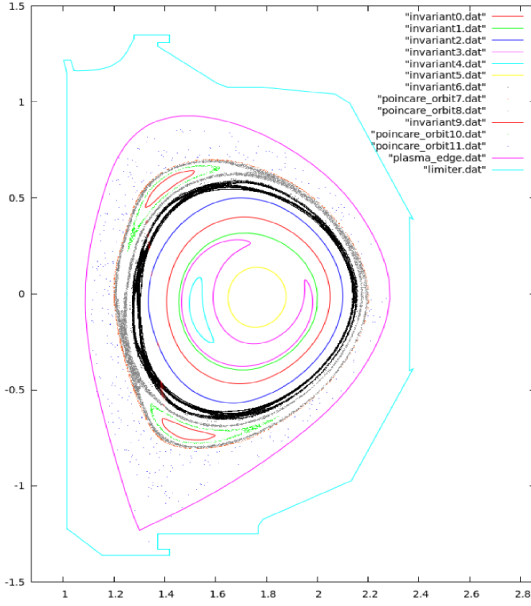


Figure B.2: Poincaré section of various orbits calculated with the Cash-Karp method for the DIII-D shot #158608 at  $t = 3\text{s}$  subjected to an  $n=3$  vacuum perturbation created by the C-coils.

the axisymmetric X-point in tokamak discharges.

Let us introduce the Poincaré map  $M : S \rightarrow S$ , where  $S$  is a given surface, for instance  $\phi = \text{const.}$ , which is always transverse to the magnetic field, and  $M(P)$  is the position of a field-line starting at  $P \in S$  after one toroidal transit in the direction of the field (Fig. B.3). The inverse map  $M^{-1}$  is obtained when we follow the line in opposite direction to the field. Notice that,  $M(M^{-1}(P)) = M^{-1}(M(P)) = P$ .

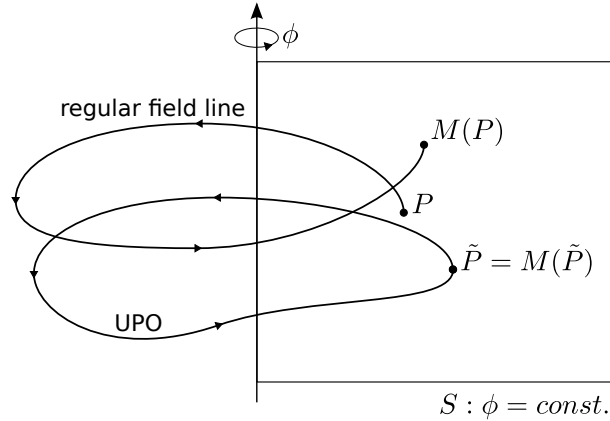


Figure B.3: Intersections of a regular field line and the UPO with a Poincaré plane.

The explicit form of  $M$  is unknown and we can only calculate it numerically through the integration of the field lines. The field line tracing is performed with the Kash-Karp integrator described in Appendix B.2. The error estimate was adjusted to  $10^{-12}$  m per step, so that cumulative errors are expected to be small.

Formally, we can look for the fixed point  $\tilde{P}$  satisfying  $M(\tilde{P}) = \tilde{P}$ , which belongs to the UPO (Fig. B.3). This can be accomplished numerically using a Levenberg-Marquardt algorithm [Marquardt (1963)] with a tracking stage or the Broyden's method [Broyden

(1965)]. Both methods involve the approximation of the Jacobian matrix of  $M$  using finite differences. Provided a good initial guess of  $\tilde{P}$  the method converges in few iterations, usually, less than 10. For a perturbed single-null discharge the unperturbed saddle becomes good initial guess for the UPO.

In the neighborhood of the fixed point  $\tilde{P} \in S$  the invariant manifolds dominate the geometry of the field lines (Fig. B.4). A localized set of points around  $\tilde{P}$  will be stretched along the unstable manifold as we apply the Poincaré map  $M$  repeatedly, and the same set of points will be stretched along the stable manifold upon repeated applications of  $M^{-1}$ . To only visualize the manifold cut it is sufficient to initialize a large number of

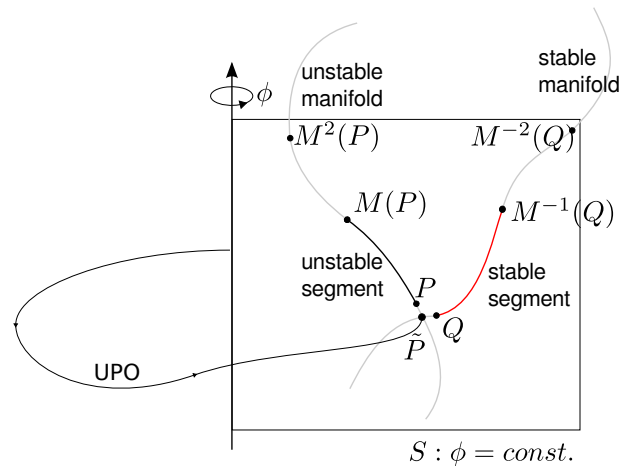


Figure B.4: The invariant manifolds are calculated by applying the Poincaré map to small segments of the invariants close to the UPO. The local invariants are obtained by fitting the mapped points from a neighborhood of  $\tilde{P}$ .

points around  $\tilde{P}$ , and apply repeatedly the map or its inverse respectively. However, this method results in a scattered representation of the manifold, which can not be optimized in a controlled fashion and can not be generalized to represent the manifold in three-dimensions, which may be desirable for comparison with tangential imaging of the plasma edge. In this work we use the local behavior of the field lines around  $\tilde{P}$  to calculate a local representation of the manifolds by adjusting a set of stretched points with a polynomial of order 5 or 7 containing the fixed point for both the stable and unstable manifolds. Then we use an adaptive algorithm to build the rest of the manifold in the transverse surface  $S$ .

For this task we use the `MAGMAN` routine, which consists in applying the Poincaré map repeatedly to a local segment of the manifold around  $\tilde{P}$  (Fig. B.4). The spatial resolution of the manifold is preserved by means of a refinement procedure that enables the introduction of new field lines where they are needed (Fig. B.5), avoiding the introduction of new orbits very close to  $\tilde{P}$  and preventing the clustering of points in other regions of the manifold. This method uses the points describing the manifold segment in the previous

iteration to calculate new initial conditions at the places where the distance between consecutive points becomes larger than some critical distance  $d_c$  [Ciro et al. (2016a)]. This critical distance was estimated by requiring that the lobes were well resolved. For this, we estimated the characteristic lobe size and required it to be one order of magnitude larger than  $d_c$ .

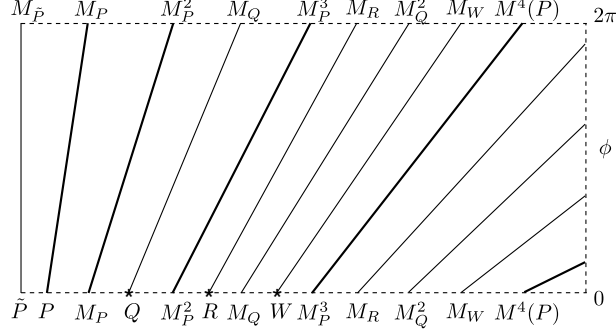


Figure B.5: Representation of the optimization process. Each line represents a field line on the invariant manifold. At the top and bottom we have the intersections with the Poincaré plane  $\phi = 0$ , where  $M_P^N = M^N(P)$ . After the first cycle, the distance between  $M_P$  and  $M_P^2$  was larger than the critical distance  $d_c$ , then a new orbit is created at  $Q$ . The refinement continues, by measuring the distance between  $M_P^2$  and  $M_Q$  that is also larger than  $d_c$ , originating  $R$  and so on. The starting points of the new orbits are calculated in the cutting plane using Lagrange polynomials passing through the neighboring points.

The new points are calculated with Lagrange polynomials at the cutting surfaces to insert the required new orbits smoothly within the sequence of existing ones. The MAGMAN routine is similar to the MAFOT about the propagation of local segments Wingen et al. (2009b), but differs in the dynamic refinement of the segment. MAGMAN also allows us to continue the manifold along material objects, like the divertor tiles and the vacuum chamber, without extra calculations or resolution losses, also, it returns an organized sequence of points that can be connected with segments to represent the manifold.

To illustrate the importance of having an organized and well distributed sequence of points we calculate the invariant manifolds of the EFIT equilibrium reconstruction for the shot #158826, when subjected to an external  $n = 3$  perturbation. For comparison, we represent the manifolds by mapping a set of 7500 random initial conditions close to the UPO for 9 toroidal cycles. In Fig. B.6 we compare the resulting scatter plots from the random sampling with those from MAGMAN, which in addition are organized and can be joined smoothly.

The comparison is performed so that the number of points representing the manifold in the random and adaptive calculations is the same. For the presented results, the MAGMAN calculation requires only 10% of the mappings required by the random sampling method and involves only 5% of its integration steps and computation time, this happens

because the lobes of the manifold develop in regions where the adaptive step integrator performs larger steps. If the comparison is performed so that we obtain the same quality representation with both methods the number of random initial conditions must be tripled, and the number of required mappings for the random method will be 30 times the required by MAGMAN. Consequently, the computation time would be about 60 times the required by MAGMAN for a plot with the same quality.

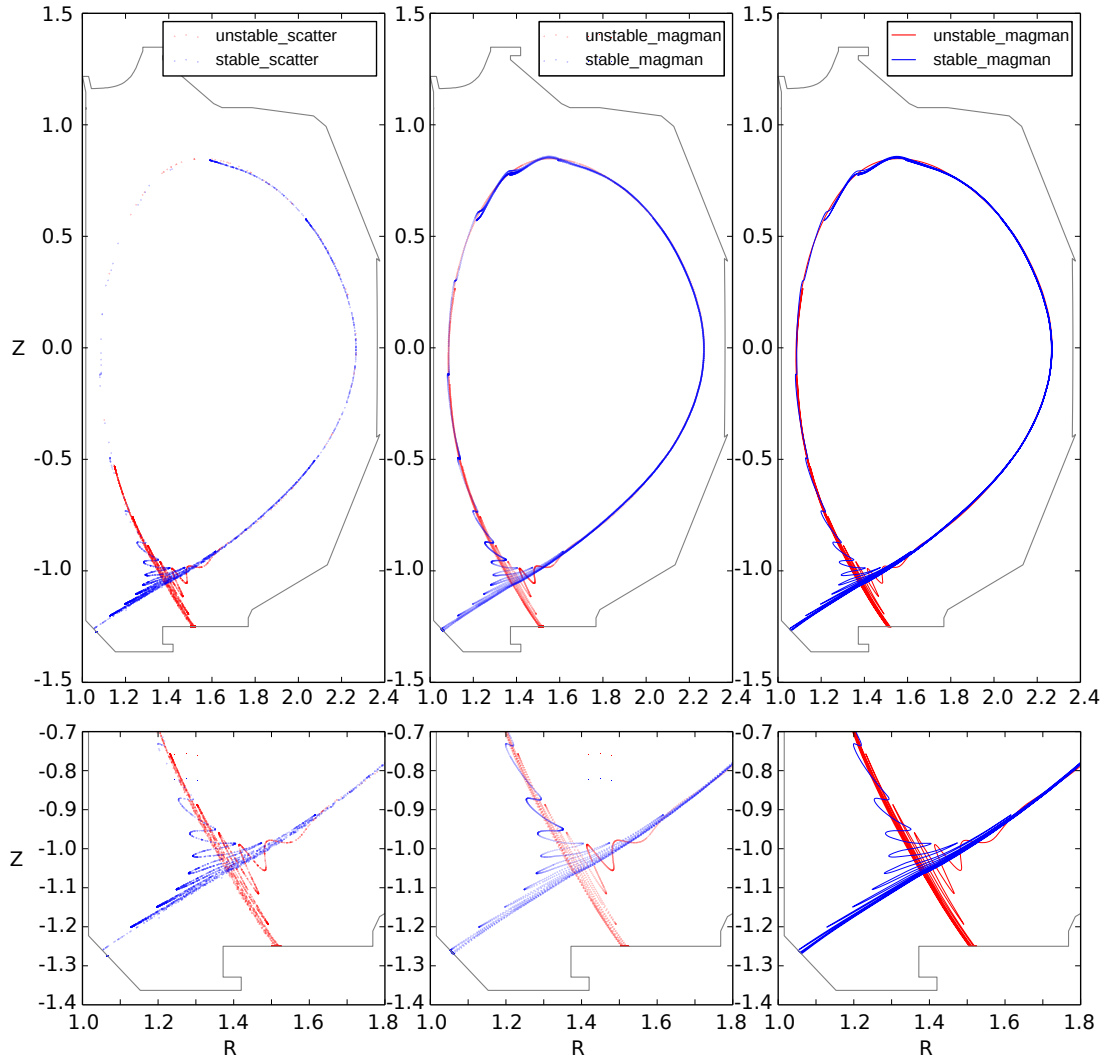


Figure B.6: The left column shows the scatter-plot of a set of 7500 random initial conditions close to the UPO mapped for 9 toroidal cycles. The center column shows the scatter plot of the MAGMAN adaptive calculation, with the same number of points. Clearly, the MAGMAN points are better distributed along the manifold and reach farther regions. The third column shows the smooth line traced along the organized MAGMAN points. As the random sampling does not provide organized points, they can not be joined smoothly to represent the manifold.



# References

- Abdullaev, S. (2014). *Magnetic Stochasticity in Magnetically Confined Fusion Plasmas*. Springer.
- Alfven, H. (1942). Existence of electromagnetic-hydrodynamic waves. *Nature*, 150:405.
- Arfken, G. B., Weber, H. J., and Harris, F. E. (2013). *Mathematical Methods for Physicists 7th. Ed.* Elsevier.
- Arnold, V. I. (1973). *Mathematical Methods of Classical Mechanics*, volume 60 of *Graduate Texts in Mathematics*. Springer - Verlag.
- Balescu, R., Vlad, M., and Spineanu, F. (1998). A Hamiltonian twist map for magnetic field lines in a toroidal geometry. *Phys. Rev. E*, 58:951.
- Bateman, G. (1987). MHD Instabilities. page 220.
- Berrino, J., Lazzaro, E., Cirant, S., D'Antona, G., Gandini, F., Minardi, E., and Granucci, G. (2005). Electron cyclotron emission temperature fluctuations associated with magnetic islands and real-time identification and control system. *Nucl. Fusion*, 45(11):1350.
- Biskamp, D. (1993). *Nonlinear Magnetohydrodynamics*. Cambridge Univ. Press.
- Biskamp, D. (1994). Magnetic reconnection. *Phys. Rep.*, 237:197.
- Bittencourt, J. A. (2004). *Fundamentals of Plasma Physics 3rd Ed.* Springer.
- Bornatici, M., R, C., and O. de Barbieri, F. E. (1983). Electron cyclotron emission and absorption in fusion plasmas. *Nucl. Fusion*, 23:1153.
- Broyden, C. G. (1965). A class of methods for solving nonlinear simultaneous equations. *Math. Comp.*, 19:577.
- Butcher, J. (2008). *Numerical Methods for Ordinary Differential Equations 2nd Ed.* John Wiley & Sons.
- Buttery, R. J., Hender, T., Ashall, J., Blow, K. A. G., and Fielding, S. (1996). Effects of resonant magnetic perturbations on divertor target power loads in Compass-D. *Nucl. Fusion*, 36(10):1369.

- Cahyna, P., Nardon, E., and Contributors, J. E. (2011). Model for screening of resonant magnetic perturbations by plasma in a realistic tokamak geometry and its impact on divertor strike points. *J. Nucl. Mat.*, 415:S927.
- Caldas, I. L., Pereira, J. M., Ullmann, K., and Viana, R. L. (1996). Magnetic fields line mappings for a tokamak with ergodic limiters. *Chaos Soliton Fract.*, 7:991.
- Cary, J. R. and Littlejohn, R. G. (1983). Noncanonical Hamiltonian mechanics and its applications to magnetic field line flow. *Ann Phys-New York*, 151:1.
- Cash, J. and Karp, A. (1990). A variable order Runge-Kutta method for initial value problems with rapidly varying right-hand sides. *ACM Trans. Math. Software*, 16:201.
- Chen, F. (1984). *Introduction to Plasma Physics and Controlled Fusion 2nd Ed.* Plenum Press.
- Ciro, D. and Caldas, I. L. (2014). A semi-analytical solver for the Grad-Shafranov equation. *Phys. Plasmas*, 21:112501.
- Ciro, D., Evans, T. E., and Caldas, I. L. (2016a). An efficient method for tracing high-resolution invariant manifolds of three-dimensional flows. *arXiv*, 1610.01091 [physics.plasm-ph].
- Ciro, D., Evans, T. E., and Caldas, I. L. (2016b). Modeling non-stationary, non-axisymmetric heat patterns in DIII-D tokamak. *Nucl. Fusion*, 57(1):016017.
- da Silva, E. C., Caldas, I. L., Viana, R. L., and Sanjuán, M. A. F. (2002). Escape patterns, magnetic footprints, and homoclinic tangles due to ergodic magnetic limiters. *Phys. Plasmas*, 9:4917.
- da Silva, E. C., Roberto, M., Caldas, I. L., and Viana, R. L. (2006). Effects of the resonant modes on the magnetic footprint patterns in a tokamak wall. *Phys. Plasmas*, 15:052511.
- de Vries, P. C., Waidmann, G., Krämer-Flecken, A., Donné, A. J. H., and Schüller, F. C. (1997). Temperature profile perturbations due to magnetic islands in TEXTOR. *Plasma Phys. Contr. F.*, 39:439.
- Dormand, J. and Prince, J. (1980). A family of embedded Runge-Kutta formulae. *J. Comp. Appl. Math.*, 6:19.
- Eich, T., Herrmann, A., Neuhauser, J., Dux, R., Fuchs, J. C., Günter, S., Horton, L. D., Kallenbach, A., Lang, P. T., Maraschek, M., Rohde, V., Schneider, W., and the ASDEX Upgrade Team (2005). Type-I ELM substructure on the divertor target plates in ASDEX Upgrade. *Plasma Phys. Cont. Fusion*, 46:815.
- Eich, T., Herrmann, A., Neuhauser, J., and Team, A. U. (2003). Nonaxisymmetric energy deposition pattern on ASDEX Upgrade divertor target plates during Type-I edge-localized modes. *Phys. Rev. Lett.*, 91:195003.

- Evans, T., Moyer, R., and Monat, P. (2002). Modeling of stochastic magnetic flux loss from the edge of a poloidally diverted tokamak. *Phys. Plasmas*, 9:4957.
- Evans, T. E., Orlov, D. M., Wingen, A., Wu, W., Loarte, A., Casper, T. A., Schmitz, O., Saibene, G., Schaffer, M. J., and Daly, E. (2013). 3D vacuum magnetic field modelling of the ITER ELM control coil during standard operating scenarios. *Nucl. Fusion*, 53:093029.
- Evans, T. E., Roeder, R. K. W., Carter, J. A., Rapoport, B. I., Fenstermacher, M. E., and Lasnier, C. J. (2005). Experimental signatures of homoclinic tangles in poloidally diverted tokamaks. *J. Phys. Conf. Ser.*, 7:174.
- Fehlberg, E. (1969). Low-order classical Runge-Kutta formulas with step size control and their application to some heat transfer problems. *NASA Technical Report*, NASA TR R-315.
- Freidberg, J. (2007). *Plasma Physics and Fusion Energy*.
- Freidberg, J. P. (2004). *Ideal MHD*. Cambridge Univ. Press.
- Goedbloed, J., Keepens, R., and Poedts, S. (2010). *Advanced Magnetohydrodynamics*. Cambridge Univ. Press.
- Goldstein, H., Poole, C., and Safko, J. (2000). *Classical Mechanics 3rd Ed.* Addison Wesley.
- Grad, H. and Rubin, H. (1958). Hydromagnetic equilibria and force-free fields. *Proc. 2nd UN Conf. on the Peaceful Uses of Atomic Energy*, 31:190.
- Guckenheimer, J. and Holmes, P. (1983). *Nonlinear Oscillations, Dynamical Systems and Bifurcations of Vector Fields*. Springer - Verlag.
- Hudson, S. R. and Nakajima, N. (2010). Pressure, chaotic magnetic fields and magnetohydrodynamic equilibria. *Phys. Plasmas*, 17:052511.
- Jackson, J. D. (1999). *Classical Electrodynamics 3rd. Ed.* John Wiley & Sons.
- Jardin, S. (2010). *Computational Methods in Plasma Physics*. Taylor & Francis Inc.
- Kadomtsev, B. B. (1992). *Tokamak Plasma: A Complex Physical System*. IOP Publishing.
- Kirk, A., Harrison, J., Liu, Y., Nardon, E., Chapman, I. T., Denner, P., and the MAST team (2012). Observation of lobes near the X point in resonant magnetic perturbation experiments on MAST. *Phys. Rev. Lett.*, 108:255003.
- Kroetz, T., Roberto, M., Caldas, I., Viana, R., Morrison, P. J., and Abbamonte, P. (2010). Integrable maps with non-trivial topology: application to divertor configurations. *Nucl. Fusion*, 50:034003.
- Kroetz, T., Roberto, M., da Silva, E. C., Caldas, I. L., and Viana, R. L. (2008). Escape patterns of chaotic magnetic field lines in a tokamak with reversed magnetic shear and an ergodic limiter. *Phys. Plasmas*, 13:092310.

- Lao, L., John, H. S., Stambaugh, R., Kellman, A., and Pfeiffer, W. (1985). Reconstruction of current profile parameters and plasma shapes in tokamaks. *Nucl. Fusion*, 25:1611.
- Lichtenberg, A. J. and Leiberman, M. A. (1983). *Regular and Chaotic Dynamics 2nd Ed.* Springer-Verlag.
- Marquardt, D. (1963). An algorithm for least-squares estimation of nonlinear parameters. *SIAM J. Appl. Math.*, 11:431.
- Mazayuki, O. (2012). Lithium as a plasma facing component for magnetic fusion research. *Technical Report 4808, Princeton Plasma Physics Laboratory.*
- McCarthy, P. J. (1999). Analytical solutions to the Grad-Shafranov equation for tokamak equilibrium with dissimilar source functions. *Phys. Plasmas*, 6(9):3554.
- Park, J., Boozer, A. H., Menard, J. E., Garofalo, A. M., Schaffer, M. J., Hawryluk, R. J., Kaye, S. M., Gerhardt, S. P., Sabbagh, S. A., and the NSTX Team (2009). Importance of plasma response to nonaxisymmetric perturbations in tokamaks. *Phys. Plasmas*, 16:056115.
- Qin, H., Liu, W., Li, H., and Squire, J. (2012). Woltjer-Taylor state without Taylor's conjecture: plasma relaxation at all wavelengths. *Phys. Rev. Lett*, 109:235001.
- Rack, M., Sieglin, B., Pearson, J., Eich, T., Liang, Y., Denner, P., Wingen, A., Zeng, L., Balboa, I., Jachmich, S., and Contributors, J.-E. (2014). Modified heat load deposition of the ELM crash due to  $n = 2$  perturbation fields at JET. *Nucl. Fusion*, 54:064012.
- Rice, B. W. (1996). q-Profile measurements with motional stark effect in DIII-D. *General Atomics Technical Report*, GA-A22269.
- Roeder, R. K. W., Rapoport, B. I., and Evans, T. E. (2003). Explicit calculations of homoclinic tangles in tokamaks. *Phys. Plasmas*, 10:3796.
- Schmitz, O., Evans, T., Fenstermacher, M., McLean, A., Boedo, J., Brooks, N., Frerichs, H., Jakubowski, M., Laengner, R., Lasnier, C., Loarte, A., Moyer, R., Orlov, D., Reimerdes, H., Reiter, D., Samm, U., Stoschus, H., Unterberg, E., Watkins, J., and the DIII-D and TEXTOR Teams (2011). The influence of three-dimensional stochastic magnetic boundaries on plasma edge transport and the resulting plasma wall interaction. *J. Nucl. Mater.*, 415:S886.
- Shafranov, V. and Zakharov, L. (1972). Use of the virtual-casing principle in calculating the containing magnetic field in toroidal plasma systems. *Nucl. Fusion*, 12:599.
- Shafranov, V. D. (1966). Plasma equilibrium in a magnetic field. *Rev. Plasma Phys.*, 2:130.
- Smale, S. (1967). Differentiable dynamical systems. *B. A. Math. Soc.*, 73:747.
- Stangeby, P. C. (2000). *The Plasma Boundary of Magnetic Fusion Devices.* IOP Publishing.

- Taylor, J. B. (1986). Relaxation and magnetic reconnection in plasmas. *Rev. Mod. Phys.*, 58:741.
- Teller, E. (1981). *FUSION Vol. 1: Magnetic Confinement, Part A*. Academic Press.
- Volpe, F. A. G., Austin, M. E., Haye, R. J. L., Lohr, J., Prater, R., Strait, E. J., and Welander, A. S. (2009). Advanced techniques for neoclassical tearing mode control in DIII-D. *Phys. Plasmas*, 16:102502.
- Wesson, J. (2004). *Tokamaks 3rd Ed.* Oxford Univ. Press.
- Wingen, A., Evans, T. E., and Spatschek, K. H. (2009a). Footprint structures due to resonant magnetic perturbations in DIII-D. *Phys. Plasmas*, 16:042504.
- Wingen, A., Evans, T. E., and Spatschek, K. H. (2009b). High resolution numerical studies of separatrix splitting due to non-axisymmetric perturbation in DIII-D. *Nucl. Fusion*, 49:055027.
- Wingen, A., Schmitz, O., Evans, T. E., and Spatschek, K. H. (2014). Heat flux modeling using ion drift effects in DIII-D H-mode plasmas with resonant magnetic perturbations. *Phys. Plasmas*, 21:012509.
- Wingen, A., Spatschek, K. H., and Abdullaev, S. (2005). Stochastic transport of magnetic field lines in the symmetric tokamak. *Contrib. Plasma Phys.*, 45:500.
- Zwingmann, W., Bécoulet, M., Moreau, P., and Nardon, E. (2006). Equilibrium analysis of tokamak discharges with toroidal variation. *AIP Conf. Proc.*, 871:430.